공학박사학위논문

Spontaneous Ignition Mechanism of Pressurized Hydrogen due to Burst Conditions and Obstacle Configurations

누출 조건과 장애물의 영향에 대한 고압 수소의 자발 점화 메커니즘

2013년 8월

서울대학교 대학원

협동과정 계산과학전공

김 세 환

Spontaneous Ignition Mechanism of Pressurized Hydrogen due to Burst Conditions and Obstacle Configurations

A dissertation
Submitted in partial fulfillment
Of the requirements for the degree of

Doctor of Philosophy

By

Seihwan Kim

Dissertation Advisor: Prof. In-Seuck Jeung

Interdisciplinary Program in Computational Science and Technology
School of Mechanical and Aerospace Engineering
Seoul National University

August 2013

Spontaneous Ignition Mechanism of Pressurized Hydrogen due to Burst Conditions and Obstacle Configurations

누출 조건과 장애물의 영향에 대한 고압 수소의 자발 점화 메커니즘

지도교수 정 인 석

이 논문을 공학박사 학위논문으로 제출함

2013년 8월

서울대학교 대학원
협동과정 계산과학전공
김 세 환

김세환의 공학박사 학위논문을 인준함

2013년 8월

위 원 장 : _____

부위원장 : _____

위 원 : _____

위 원 : _____

위 원 : _____

Abstract

Spontaneous Ignition Mechanism of Pressurized Hydrogen due to Burst Conditions and Obstacle Configurations

Seihwan Kim
Interdisciplinary Program in Computational Science and Technology
The Graduate School
Seoul National University

Hydrogen gaining more attention as a next generation clean energy carrier. However as its volumetric efficiency is low, in order to be used for this purpose, it needs to be compressed. However, high-pressure hydrogen presents potential hazards because of its strong flammability. According to past research, over 60% of hydrogen related accidents have been reported that the ignition sources have yet to be identified.

In this thesis, both the experimental and numerical studies have been conducted to clarify the mechanism of spontaneous ignition due to a sudden release of high-pressure hydrogen through tubes. Experimental model has been designed to simulate the release of hydrogen through a tube by bursting the diaphragm installed between a reservoir chamber and an extension tube. The numerical simulation integrates rigorously formulated numerical models. Because of the phenomena included such as strong shock, expansion waves, turbulence, chemical reaction, the models should be capable of shock-capturing, contact-resolving, entropy-satisfying, enthalpy-preserving, and conservation-satisfying. Using these approaches, burst pressure range is extended up to 40 MPa which is not tested before. Results from the

experiment of relationship between tube length and burst pressure shows a general tendency that the propensity of spontaneous ignition is proportional to the burst pressure and extension tube length. Study on a flow structure, a flame development and propagation inside the axisymmetric tube, which is impossible to visualize, is performed using computational code. The results show that flat shaped complete flame has been quickly developed in smaller inner diameter tube and the influence of a disturbance due to a diaphragm burst remains longer when the tube inner diameter is large. Another simulation tries to show the effect of a diaphragm shape depending on the burst pressure. The results show that the ignition mechanism is closely connected with flow formation inside the tube, which is strongly affected by the burst conditions. It suggests that the possibility that the ignition occurs can be higher if there are any factors that result in mixing, such as multi-dimensional shock interactions or any disturbances from the shape of the disk. However, this trend is shown when the burst pressure is low, as it can be seen from that the mixing process can differ sensitively with the shape of pressure boundary. On the other hand, if the burst pressure is high, the ignition feature is less sensitive with the shape of pressure boundary. In company with the study on the phenomena inside the tube, the effect of an obstacle near the tube exit is studied using flat plate with varying height and distance. Although the plate could generate stagnation region in front of it, any secondary reaction is not observed. The mixing in the recirculation at the edge of the wall is also not able to make the heated-air and hydrogen react. But the obstacle could decrease the flame stabilizing time. The results emphasize the importance of flame generation inside the tube.

Keywords : high pressure hydrogen, spontaneous ignition, rupture disk, impinging jet, hydrogen safety

Student Number : 2008-30832

Contents

표 목차

그림 목차

Chapter 1
Introduction

1.1 Background

Hydrogen element covers about 75 % of the Earth, and can be widely used, such as in a liquid rocket engines, hypersonic vehicles, mobile vehicles. Especially after the Kyoto Protocol commitment, as green energy is becoming an issue, hydrogen is gaining high attention as the next generation energy source. But in order to be used for this purpose, it needs to be compressed or liquefied due to its low volumetric density. However, high-pressure hydrogen presents potential hazards because of its strong flammability, e.g., the wide range of flammability. Although liquid hydrogen (LH2) has the advantage of extreme cleanliness and the more economic type of storage, however, on the expense of a significant energy consumption of about one third of its heat of combustion. Another drawback is the unavoidable loss by boil off which is typical to maintain the cold temperature in the tank. For this reason, at present, most systems prefer the compressed form over the liquefied form. Many research are focused on pressurized hydrogen, in order to efficiently operate a hydrogen vehicle, hydrogen must be pressurized at least 700 times the atmosphere pressure. However, high pressure hydrogen comes with extreme

danger due to its ignition characteristics.

1.1.1 Characteristics of Hydrogen

PHYSICAL PROPERTIES OF HYDROGEN

Hydrogen can be considered an ideal gas over a wide temperature range and even at high pressures. At standard temperature and pressure conditions, it is a colorless, odorless, tasteless, non-toxic, noncorrosive, non-metallic diatomic gas, which is in principle physiologically not dangerous. One of its most important characteristics is its low density, which makes it necessary for any practical applications to either compress the hydrogen or liquefy it.

Hydrogen gas is highly diffusive and highly buoyant; it rapidly mixes with the ambient air upon release. The diffusion velocity is proportional to the diffusion coefficient and varies with temperature according to T^n with n in the range of 1.72-1.8. Corresponding diffusion rates of hydrogen in air are larger by about a factor of 4 compared to those of air in air. The positive buoyancy of hydrogen is a favorable safety effect in unconfined areas, but it can cause a hazardous situation in partially confined spaces, where the hydrogen can accumulate, e.g., underneath a roof. Both diffusion and buoyancy determine the rate at which the gas mixes with the ambient air. The rapid mixing of hydrogen with the air is a safety concern, since it leads very soon to flammable mixtures, which also will quickly dilute to the non-flammable range. Therefore it is estimated that in a typical unconfined hydrogen explosion, only a fraction of the gas mixture cloud is involved releasing in fact not more than a few percent of the theoretically available energy. For small hydrogen leaks, buoyancy and diffusion effects in air are often overshadowed by the presence of air currents from a slight ambient wind,

very slow vehicle motion or the radiator fan. In general, these currents serve to disperse leaked hydrogen even more quickly with a further reduction of any associated fire hazard.

Because of its small size, its small molecular weight and its low viscosity, hydrogen can cause a problem with respect to the inclination of the gas to leak at a larger molecular flow rate than other gases. Diffusion in small amount is even possible through intact materials which may lead to gas accumulation in confined spaces.

When used as vehicle fuel, the propensity for hydrogen to leak necessitates special care in the design of the fuel system to ensure that any leaks can disperse with minimum obstruction and the use of dedicated leak detection equipment on the vehicle and within the maintenance facility. The boiling point of a fuel is a critical parameter since it defines the temperature to which it must be cooled in order to store and use it as a liquid. Liquid fuels take up less storage space than gaseous fuels, and are generally easier to transport and handle.

Hydrogen gas dissolved in liquids will seepage into adjoining vessel materials. At elevated temperatures and pressures, hydrogen attacks mild steels severely, causing decarburization and embrittlement. This is a serious concern in any situation involving storage or transfer of hydrogen gas under pressure. Hydrogen also exhibits a positive Thompson-Joule effect at temperatures above 193 K, the inversion temperature. It means that the temperature of the hydrogen gas increases upon expansion, which may lead to ignition. For example, the temperature change is six degrees, if a sudden pressure drop from 20 MPa to ambient pressure takes place.

CHEMICAL PROPERTIES OF HYDROGEN

Hydrogen is able to react chemically with most other elements. In connection with oxygen, hydrogen is highly flammable over a wide range of concentrations. When a small amount of activation energy is provided to a mixture of hydrogen and oxygen, the molecules react strongly, releasing a substantial amount of heat, with water as the final product. We experience this reaction as a fire or explosion. The mass-related energy density of hydrogen is very high; 1 kg of hydrogen contains 132.5 MJ, which is approximately 2.5 times more energy than is contained in 1 kg of natural gas. The energy content of hydrogen is given as either lower heating value (LHV) of 242 kJ/mol or as higher heating value (HHV) of 286 kJ/mol. The difference of 15.6%, which is large compared to other gases, is due to the heat liberated upon condensation of the water vapor. A stoichiometric hydrogen-air mixture, i.e., where maximum combustion energy is released, contains 29.5% volume of hydrogen. The combustion product of hydrogen is water vapor. It burns in a non-luminous, almost invisible pale blue, hot flame to water vapor liberating the chemically bound energy as heat. The maximum flame temperature of a burning (premixed stoichiometric) hydrogen-air mixture is 2403K. There is a wide flammability range of hydrogen at room temperature between 4 and 75% volume of concentration in air and up to 95% volume in oxygen.

Flammability

The lower flammability limit (LFL) as the minimum amount of fuel that supports combustion, is usually the more important limit, since it will be reached first in a continuous leakage. The flammability range widens with higher temperatures. Below the LFL, there is not enough fuel present to

support combustion; the fuel/air mixture is too lean. The influence of the temperature is expressed in the modified Burgess-Wheeler equation for the LFL, which is for hydrogen at ambient pressure [1]:

$$c_{LFL} = c_{LFL}(300K) - \frac{3.14}{\Delta H_c}(T - 300) = 4.0 - 0.013(T - 300) \quad (1\text{-}1)$$

where H_c is the net heat of combustion and T given in [K].

The UFL of a gas is the highest gas concentration that will support a self-propagating flame when mixed with air and ignited. Above the UFL, there is not enough oxygen present to support combustion; the fuel/air mixture is too rich. Between the two limits is the flammable range in which the gas and air are in the right proportions to burn when ignited.

The respective equation for the upper flammability limit (UFL) is [2]:

$$c_{UFL} = 74.0 + 0.026(T - 300) \quad (1\text{-}2)$$

valid for the temperature range 150-300 K. Measurements of upward flame propagation at higher temperatures[3] have shown a further increase of the UFL with initial temperature reaching 87.6% at 673 K.

One consequence of the UFL is that stored hydrogen (whether gaseous or liquid) is not flammable while stored due to the absence of oxygen in the cylinders. The fuel only becomes flammable in the peripheral areas of a leak where the fuel mixes with the air in sufficient proportions.

The potential for an explosion of a flammable hydrogen-air mixture is very high. The auto-ignition temperature, which is the minimum temperature of a hot surface that can ignite a flammable mixture, is for hydrogen in the

range of 800-1000 K depending on the experimental conditions. It is relatively high, but can be lowered by catalytic surfaces. Hydrogen gas does not have a flash point as it is already a gas at ambient conditions. It means that cryogenic hydrogen will flash at all temperatures above its boiling point of 20 K.

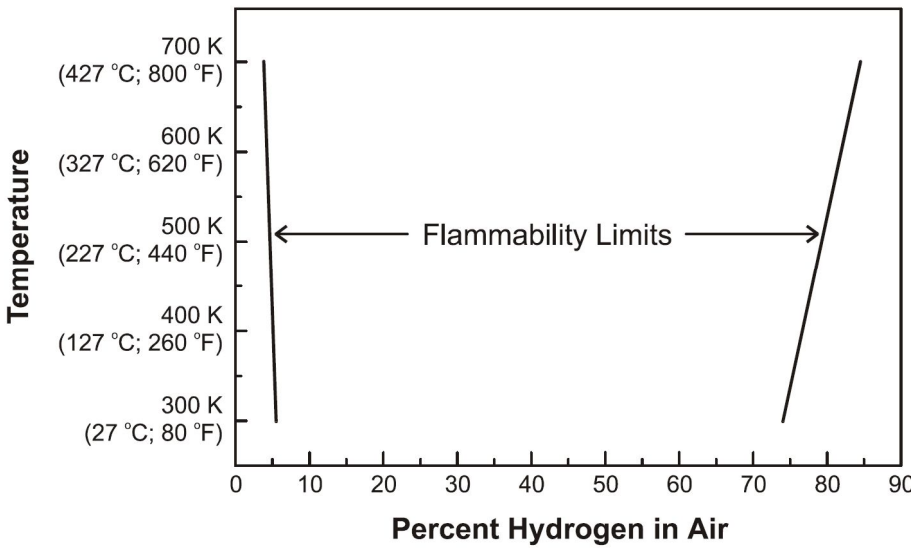

Figure 1-1 Variation of Hydrogen Flammability Limits with Temperature

Ignition Energy

Ignition energy is the amount of external energy that must be applied in order to ignite a combustible fuel mixture. Energy from an external source must be higher than the auto-ignition temperature and be of sufficient duration to heat the fuel vapor to its ignition temperature. Common ignition sources are flames and sparks. Although hydrogen has a higher auto-ignition temperature than methane, propane or gasoline, its ignition energy at 0.02mJ is about an order of magnitude lower and is therefore more easily ignitable. Even an invisible spark or static electricity discharge from a human body (in dry conditions) may have enough energy to cause ignition. The minimum ignition

energy is further decreasing with increasing temperature, pressure, or oxygen contents.

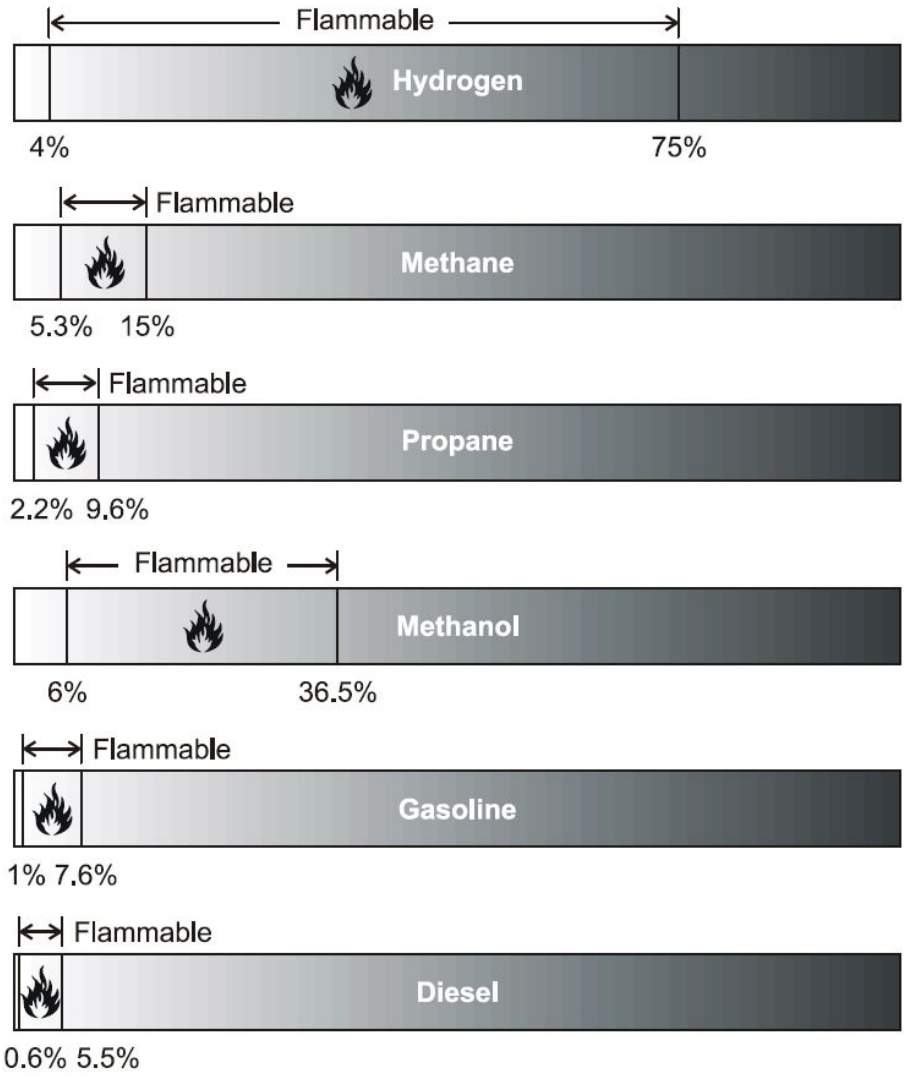

Figure 1-2 Flammability Ranges of Comparative Fuels at Atmospheric Temperature

1.1.2 Accident caused by hydrogen

As seen, hydrogen has high chance to ignite spontaneously. In order to investigate fire hazards due to flammable substances and its ignition sources, Asbury [4] analyzed data from the Major Hazard Incident Database Service [5], open to the public. About 4300 accidents were studied and classified by England, the United States, and other countries, and the result indicates that the source of ignition is often not found. The search revealed 81 incidents involving releases of hydrogen. Of those, a delay between release and ignition was reported for only four releases. It has to be assumed that the others ignited immediately. In 11 cases, the source of ignition was identified, but in the remainder, 86.3% of incidents, the source was not identified. This contrasts with the non-hydrogen releases, where 1.5% did not ignite, and only 65.5% of ignition sources were not identified. This does suggest that there is a difference in propensity for ignition between hydrogen and non-hydrogen gases when released. The summary of sources identified and their frequency is given in Table 1 below. It is worthy of note that since this is a major hazard incident database, releases of hydrogen which simply dispersed and did not involve fire, explosion, or other major hazard are not recorded, so the non-ignition being reported as zero is not necessarily an indication that all hydrogen releases ignited.

Table 1-1 Frequency of occurrence of ignition sources

Ignition soruce	Hydrogen incidents		Non-hydrogen incidents	
	Frequency	%	Frequency	%
Arson	0		37	2.6
Collision	2	2.5	121	8.4
Flame	3	3.7	113	7.9
Hot surface	2	2.5	56	3.9
Electric	2	2.5	114	7.9
Friction spark	2	2.5	33	2.3
Non identified	70	86.3	942	65.5
Non-ignition	0	0	21	1.5
Total	81	100.0	1437	100.0

Identification of ignition source

Astbury [6] investigated the accidents in which the ignition source were not clearly defined, and analyzed the expected ignition mechanisms.

a. Spontaneous ignition at burst pressure of 2.1 MPa in 1922

As numerous events of spontaneous ignitions occurred as 2.1 MPa hydrogen are released to the atmosphere, Nusselt [7] carried out experiments in order to investigate the cause of the ignition. He first investigated the effects due to nozzle shape and material, however, ignition due to sudden release of hydrogen did not occur. He then came upon a hypothesis that the ignition could have happened due to rust existing within the cylinder. In order to prove his hypothesis, he carried out an experiment in which he fed various

particles, but only iron oxide and manganese dioxide resulted hydrogen self-ignition. In order to further investigate on the catalytic effect of the rust, he added hydrogen-air premixed gas into a sealed container with iron oxide. Although many try has been made, those catalytic reactions did not result in an explosion.

Additionally, he carried out an experiment in which hydrogen was released through a long pipe, connected to the end of the tunnel, and found that ignition occurred only when the end was covered with an iron cap. The mechanism was not understood, so further trials were conducted. The test conducted in the dark showed that when the hydrogen leaked out of a flange—the corona discharge was visible, which increased when the pipe was tapped to stir up dust. Further work showed that when sharpened copper wires were used to promote corona discharges, ignition occurred when the point was bent away from the gas direction, whereas no ignition occurred when the wire was pointing in the direction of flow. Consequently, it is apparent that a corona discharge was likely to have been the source of ignition in this case.

b. Explosion near the isolation valve in 1926 and 1930

Following two hydrogen related explosion accidents in 1926 and 1930, Fenning and Cotton [8] carried out experiments in order to reveal the cause of the accidents. As the cause of the ignition in both cases was obscure, experimental work was conducted to try to establish the mechanism. It was noticed that there was many evidence of fine dust, presumably metal oxide, being present in the pipework during the examination after the explosion. This led them to surmise that the explosion had been initiated by an electrostatic discharge, presumed to have been generated by the fine dust being blown

along the pipe by the high velocity hydrogen. However, despite many attempts, no ignition was achieved in their experiments.

c. Ignition result from leaking hydrogen near a flange

Bond [9] reports two hydrogen ignition cases. In the first incident, hydrogen at a pressure of 11.1MPa was leaking from a gasket between two flanges. At the beginning there was no ignition, however when the plumber used a hammer on the repair tool to fasten the bolt, it ignited. It is not apparent whether the ignition source was an impact spark from a hammer wrench being used to tighten the bolts on the joint, or attributed to the mechanism of diffusion ignition. The second incident refers to a cylinder of hydrogen being connected to a piece of laboratory apparatus. The laboratory technician cracked the valve open to clear any dirt out of the connection, and when he did so, the escaping gas ignited immediately. Bond attributes this ignition to the phenomenon of diffusion ignition.

d. Ignition during the ball valve closing

Reider et al. [10] investigated another accident which occurred when the deliberate release of a large quantity of hydrogen to determine the sound pressure levels. The hydrogen was released from storage at an initial pressure of 23.6MPa, for a period of 10 s. After 10 s, the 150mm diameter valve was being closed, and 3 s after starting to close the valve, ignition occurred.

Prior to the experimental discharge, three potential ignition mechanisms were examined which were electrification of the gas, electrification of particles in the gas, and metal particles abrading a metal bar welded across the mouth of the nozzle. Of these, the first was discounted as pure gases are

known to have negligible electrostatic charging. The second was considered, but as the system had been thoroughly cleaned out and blown down prior to the test, it was considered that there would not be any particles present. However, the velocity of the gas being discharged, at 1216 m/s, was far higher during the run than had been used before, so this potential mechanism could not be discounted. The third mechanism was considered as a possibility as the discharge velocity was high—possibly dislodging particles and impacting them on the bar. This too could not be discounted. After the ignition, it was found that the bar had been torn loose at one end, and this may have presented a possible ignition source which had not been foreseen.

1.1.3 Proposed Mechanisms

a. Reverse Joule–Thomson effect

When a compressed gas is vented to atmosphere through a nozzle, the gas expands. If it is below the Joule–Thomson inversion temperature, then the gas cools on expansion. The inversion temperature for air is about 325 °C, so air at ambient temperature and above atmospheric pressure will cool on expansion.

Hydrogen on the other hand has a Joule–Thomson inversion temperature of about 193K (−80 °C) [11], so compressed hydrogen at ambient temperature will heat up on expansion to atmospheric pressure. Data from a Mollier diagram [12] can determine the rise, which for initial conditions of 50MPa and 9 °C will give a rise in temperature of between 9 K and 18 K.

This is hardly conducive to auto-ignition since the auto-ignition temperature of hydrogen is 585 °C [11]. At higher pressures and temperatures, the Mollier diagram shows that isenthalpic lines become very non-linear, so

the temperature rise on expansion is likely to be much larger. However, data for the Joule–Thomson coefficient for hydrogen at pressures up to 250MPa and 150 °C are given by Michels et al. [13] and show that at 100MPa and temperatures up to 150°C, the Joule–Thomson coefficient does not exceed 0.53K MPa, so ignition by this mechanism is unlikely at the pressures in most of the incidents quoted above.

However, the data for the Joule–Thomson coefficient quoted by Michels et al. are calculated partly from experimental data, partly from others' work, and partly by extrapolation and calculation from other measured parameters. This assumes that the Joule–Thomson coefficient is constant over the whole pressure and temperature range, which it is not. Thus where extrapolation is used, it is possible that the values may be erroneous, particularly at the boundaries of the available data, since the quoted coefficients cannot be constant at both isothermal and isenthalpic conditions. Although on its own it would appear that the Joule–Thomson expansion would not raise the temperature of any hydrogen to its normal auto-ignition temperature, it should be kept in mind that it will raise the temperature of the gas above ambient. This alone is unlikely to cause ignition, but in combination with other effects may be sufficient to initiate spontaneous ignition. This is discussed later.

b. Electrostatic ignition

A stoichiometric mixture of hydrogen with air has very low minimum ignition energy of 0.017 mJ [14]. This makes it far more sensitive to ignition than most other gaseous or vaporized flammable materials, and therefore the potential for electrostatic ignition is much greater. There are three main types of electrostatic discharge to consider; spark discharges, brush discharges, and

corona discharges.

- Spark discharges from isolated conductors

These are characterized by a single plasma channel between the high potential conductor and an earthed conductor. The discharge is completed in a very short time, and almost all the charge is transferred in a single spark. Calculations in the paper show that even when quenching effects are taken into account, energy of 0.164 mJ at 2 kV is more than sufficient to ignite the stoichiometric hydrogen-air mixture. Consequently, whilst electrostatic charging of people refueling vehicles with petrol rarely gives rise to ignitions, it is significant that the voltage required for hydrogen to be ignited is below 2 kV. This voltage can be generated easily, without their being aware of it, on people standing on an insulating surface so there is a potential for personnel to ignite hydrogen leaks very easily, without any apparent ignition source being present.

- Brush discharges

These are typified by a discharge between a charged insulator and a conducting earthed point. They are characterized by many separate plasma channels, combining at the conductor, and are typical of those from insulating plastics. Work by Gibson and Harper [15] introduced the term of incendivity or equivalent energy which is where the brush discharge has the ability to ignite an atmosphere, with the same minimum ignition energy as a spark which will just ignite the flammable atmosphere. Typical equivalent energies were found to be about 4 mJ for brush discharges from flat polyethylene sheets. However, Ackroyd and Newton [16] found that certain more modern plastics, and thin plastic coatings on earthed metal, had higher equivalent energies.

- Corona discharges

These are silent, usually continuous discharges which are characterized by a current but no plasma channel. A corona discharge is able to ignite a hydrogen-air mixture without there being a discrete spark or single discharge event. This is a known potential ignition source, particularly from atmospheric electrical activity. Where a potential exists some distance from an earthed surface, an electric field will be present. This field will be linear between a pair of parallel plates. However, if a small point is placed on one of the plates, it will modify the field, and concentrate the lines towards the point. If the local concentrated field strength exceeds the breakdown strength of the air, then a current will pass in the form of a corona. Where vents discharge hydrogen to atmosphere, it has been known for the gas at the vents to ignite for no apparent reason. Studies undertaken many years ago on hydrogen vents [17-19] showed that ignition was rare during fine weather, but was more frequent during thunderstorms, sleet, falling snow, and on cold frosty nights.

c. Diffusion ignition

The phenomenon of diffusion ignition has been postulated by Wolanski and Wójcicki [20], who demonstrated that ignition occurred when high pressure hydrogen was admitted to a shock tube filled with air or oxygen. They found that ignition could be achieved even if the temperature was below the auto-ignition temperature of the hydrogen. They calculated that ammonia synthesis gas, composed of a 3:1 mixture of hydrogen and nitrogen would ignite in air if the shock wave exceeded a Mach number of 2.8 at a temperature of 575 K. A shock-wave of this Mach number would be produced by an upstream pressure of 3.9 MN/m^2, which is typical of the pressure and

temperature conditions in an ammonia synthesizer plant. They also calculated that ignition would occur at a lower Mach number of only 1.7, corresponding to an upstream pressure of 1.3 MN/m^2, when the shock wave was reflected by an obstacle. They confirmed their results using a shock tube, which was totally enclosed. Although they confirmed their calculations using the shock tube, there is no experimental work undertaken with releases to an unconfined atmosphere, such as would be the case for a leak from high pressure direct to atmosphere. They also stated that the auto-ignition temperature for ammonia synthesis gas containing 75% volume of hydrogen, with a balance of nitrogen, had an auto-ignition temperature of 685±30 K (412±30 °C). This auto-ignition temperature seems unduly low compared to that reported by other workers, notably the 585 °C by NASA [11] and 560 °C quoted by IEC 60079-20:2000 [21], although the NFPA [22] reports 500 °C. There is no indication whether their auto-ignition temperature was measured at the expected final pressure in the shock tube, or at atmospheric pressure. Although their shock tube experiments produced ignition, their initial temperature was rather high at 575 K (302 °C), requiring an increase of only 110 K to reach their auto-ignition temperature of hydrogen.

d. Sudden adiabatic compression

This occurs when a gas is compressed adiabatically. If a gas obeys the ideal gas laws, then compressing it at constant entropy would increase the pressure due to the compression in accordance with the relationship

$$PV^{\gamma} = k \tag{1-3}$$

Since for a perfect gas the relationship $PV = nRT$ holds, these two equations may be combined to determine the adiabatic temperature rise due to compression as

$$T_2 = T_1 \left(\frac{V_1}{V_2} \right)^{\gamma - 1} \tag{1-4}$$

Since most diatomic gases have a specific heat ratio of about 1.4, an air–hydrogen mixture would have similar properties, and therefore the same magnitude of temperature rise would occur. However, this assumes adiabatic compression, which is unlikely to be realized in practice. In experiments conducted by Pan et al. [23], the actual measured temperature realized by a compression ratio of 28 times was only 149 K. This compares to a theoretical estimate of 453 K for a plug-flow model where no mixing takes place, and 108 K for a fully mixed system. Thus isentropic compression is unlikely to occur in practice. Work by Cain [24], however, indicates that compression ignition of hydrogen–oxygen–helium mixtures occurs at a relatively constant temperature of 1050 K, at pressure rise ratios of 35~70 starting at 300 K at atmospheric pressure. Reverse calculation, using equation (1-3) and (1-4) combined and re-arranged in terms of ratios, indicates that a temperature rise from 300 K to 1050 K would require a pressure rise ratio that is greater than that measured by Cain, suggesting that there is another ignition mechanism present.

e. Hot surface ignition

This is a phenomenon shared by most flammable gas or vapor air mixtures, in that providing the surroundings are at a high enough temperature, the rate of oxidation generates more heat than is being lost to the surroundings, so allowing the oxidation chain-reaction to progress. This is the usual method of determining auto-ignition temperatures. For example, NASA [11] report values for stoichiometric gaseous hydrogen–air mixtures at 101.3 kPa, of between 773 K and 850 K, and at reduced pressures of 20~50 kPa, ignitions have occurred at temperatures as low as 620 K (347 ˚C).

An abstract of work by Neer [25] indicates that ignitions under shock conditions occurred at much lower temperatures than those resulting from classical static conditions and concludes that a more realistic measurement is to use the term ignition speed rather than ignition temperature to take account of this. At temperatures approaching the classical thermal ignition temperature for stationary mixtures, the ignition delay is short, becoming longer as the temperature drops. Neer postulates that the onset of ignition is favored by higher densities in the lower region of the boundary layer, higher wall temperatures, higher flow speeds, and longer test times. He also suggests that charged particles which are generated by the high speed flow over the walls are responsible for the ignitions. However, work by Bulewicz et al. [26] showed that the position and mode of heating a hot plate had an effect. He used a slow-heating method where free-convection was important, and a time delay between exposure and ignition was apparent, depending on the rate of temperature rise. The orientation of the heating surface also affected the delay, with a longer delay with the heated surface pointing down than when the heated surface was pointing up. During the delay period, H and OH radicals

slowly increased in concentration, until the concentration reached a certain level, at which point ignition was observed with a violent increase in the temperature. This correlated well with their theory. They also looked at heating the plate impulsively using a capacitor bank to discharge through the plate, heating it resistively. The ignition temperatures were higher when heated impulsively than when heated by a slow temperature rise, with ignition temperatures of typically 1600~2500 K.

1.2 Goal

This research investigates the spontaneous ignition phenomena of the hydrogen as high pressure hydrogen is suddenly released through a pipe as the diaphragm bursts. The topic is divided into three subtopics:

Firstly in order to investigate the ignition mechanism for the various burst conditions, the flow characteristic near the diaphragm and the flow within the axisymmetric tube, where experimental visualization is limited, were numerically analyzed and the results are compared with actual experimental data.

Secondly, limits of hydrogen self-ignitions investigated by varying the diaphragm burst conditions. Self-ignition possibilities, flame propagation characteristics are analyzed and compared with existing experimental results. Especially, according to previous experiments, flow characteristics of the released hydrogen drafty changes depending on the tube structure, and thus the effect of the tube structure is investigated.

Lastly, considering daily use of pressurized hydrogen, experimental study of the effect of an obstacle near a fuel tank or pipelines on the self-ignition and flame propagation is carried out and the results are compared with numerical analysis.

1.3 Outline

This thesis contains 6 chapters, the context of each chapter are as follows:

Chapter 2 reviews the literatures that related to the spontaneous ignition caused by the sudden leakage of high pressurized hydrogen. The researches tried to examine the self-ignition using high pressure chamber and extension tubes, to find the limiting condition of spontaneous ignition. Also numerical simulation has been conducted to analyze the ignition process and flow development inside the tube.

In chapter 3, the test equipment, test models, properties of the pressure transducer and the photodiode are introduced. Also the visualization technique, shadowgraph, is presented. The schematics of the test facility and test procedure are addressed in the end of the chapter.

Chapter 4 deals with the numerical approaches, such as governing equation, solution procedure, external library CANTERA which solves the chemical reactions, latest hydrogen reaction model, boundary condition, and computational domain.

In chapter 5, the results of the studies to find the mechanism of high pressurized hydrogen are discussed. By changing the length of extension tube

and the burst pressure, relation between those and possibility of spontaneous ignition has been studied. The effect of a shape of pressure boundary at high and low burst pressure was also analyzed assuming four different pressure boundary condition. In addition, preparing the common usage of hydrogen, the effect of the dimension of tubes and an environment, such as safety wall, on the spontaneous ignition are studied. Simulation was conducted to find the effect of a dimension to the flow development and flame propagation inside the tube. And model wall is installed near the exit and the data is obtained for various height and distance.

In chapter 6, as a conclusion, the results from various conditions are summarized. In addition, some research objectives that can be started from this research are suggested.

Chapter 2
Literature Reviews

As listed in the previous chapters, various hypothesis on self-ignition mechanisms of hydrogen have been proposed, and many researchers have carried out experimental and numerical research in order to find out the actual reason. This chapter reviews the findings of the characteristics of the preceding researches.

2.1 Experimental Studies

2.1.1 First experiment on spontaneous ignition with various geometries

Motivated by the research of Chaineaux et al. [27], which studies flammable cloud formation by pressurized releases of hydrogen jets into air in 1990, the first experimental work on spontaneous ignition of pressurized flammable gas release into an unconfined atmosphere was carried out. In the research, Dryer analyzed the effect of hydrogen pressure, temperature and the tube structure at the rear end. The study demonstrates the spontaneous ignition from sudden compressed hydrogen releases that is not well documented before his work, for which little fundamental explanation, discussion or research foundation exists. In fact, no experimental work exists on

spontaneous ignition of pressurized flammable gas releases of varying geometries into an unconfined atmosphere, which would be representative of incidents reported in industry. And this phenomenon is apparently not encompassed in recent formulations of safety codes and standards for piping, storage, and use of high pressure compressed gas systems handling hydrogen. Accidental or intended, rapid failure of a pressure boundary separating sufficiently compressed hydrogen from air can result in multi-dimensional transient flows involving shock formation, reflection, and interactions such that reactant mixtures are rapidly formed and achieve chemical ignition, inflammation, and transition to turbulent jet diffusive combustion, fed by the continuing discharge of hydrogen.

A variety of experiments were conducted to investigate the dependence of observations on the failure pressure and internal flow geometry downstream of the disk. Experiments were performed using different open-ended flow geometries downstream of a standard commercial, screw union type, straight-through burst disk holder with 1/2" NPT female connections (18.3 mm ID). Ambient air temperatures for the experiments ranged between 280 K and 305 K, with relative humidity levels between 60% and 90%.

Moreover, simple transient shock theory along with chemical kinetic ignition calculations is used to support interpretation of observations and qualitatively identify controlling gas properties and geometrical parameters. According to the results, subsequent reflection of the resulting transient shock from surrounding surfaces through mixing layers of hydrogen and air may have the potential for producing ignition and continuing combustion. Similar considerations for compressed methane, for mixtures of light hydrocarbons and methane, and for larger carbon number hydrocarbons show similar auto-

ignition phenomena may occur with highly compressed methane or natural gas, but are unlikely with higher carbon number cases, unless either the compressed source or surrounding air is sufficiently pre-heated above ambient temperature. Spontaneous ignition of compressed hydrocarbon gases is also generally less likely, given the much lower turbulent blow-off velocity of hydrocarbons in comparison to that for hydrogen.

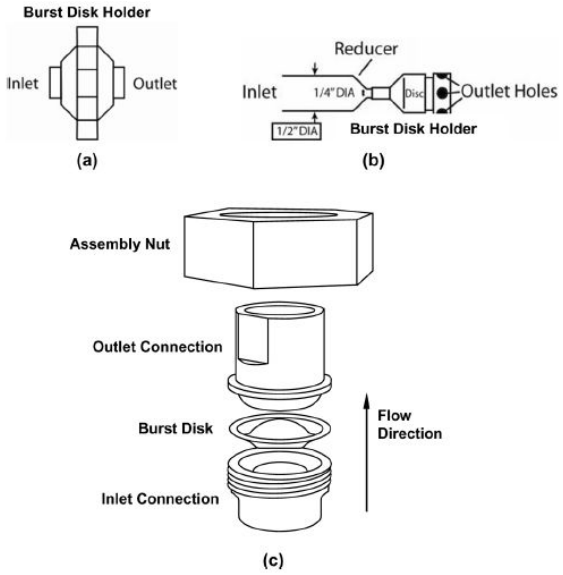

Figure 2-1 Burst disk holder structure [28]

2.1.2 Study on determination of the governing physical phenomena

Golub et al.[29] investigate hydrogen self-ignition occurring as a result of the formation of a shock wave. The aim of the study is the numerical and experimental determination of governing physical phenomena affecting the hydrogen self-ignition at the discharge into the tube filled with air.

An experimental investigation of hydrogen self-ignition in air was carried out in tubes of cylindrical and rectangular cross sections of lengths

65~185 mm and cross-sectional areas of 20 mm^2.

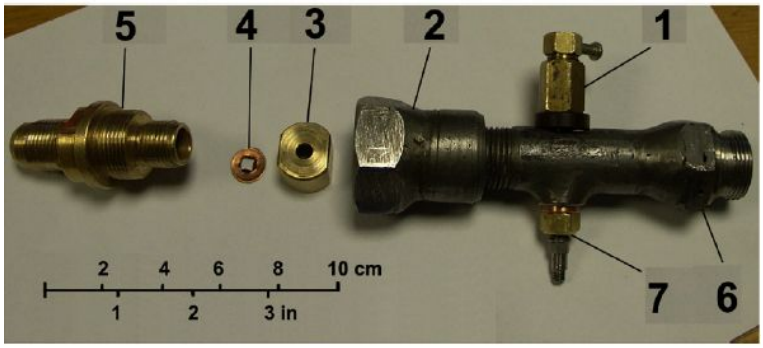

Figure 2-2 Test tube with cylindrical cross section [29]

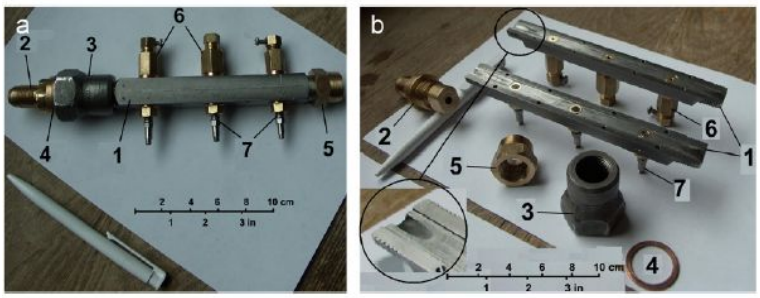

Figure 2-3 Test tube with rectangular cross section [29]

The shock wave is formed in front of high-pressure hydrogen gas propagating in a tube. The ignition of the hydrogen–air mixture occurs at the contact surface of the hydrogen and oxidant mixture and is due to the temperature increase produced as a result of the shock wave. The required condition for self-ignition is to maintain the high temperature in the mixture for a time long enough for inflammation to take place. The results showed that the self-ignition in the tube of 20 mm^2 in cross-sectional area, which has round and rectangular shapes, is possible following failure of the bursting disc of the hydrogen high-pressure chamber at an initial pressure of 40 atm and higher. Self-ignition of hydrogen burst from the orifice of 5 mm in diameter

into the semi-confined space is possible at initial pressure in the high pressure chamber of 123 atm and higher.

A physicochemical model involving gas-dynamic transport of a viscous gas, detailed kinetics of hydrogen oxidation and heat exchange in the laminar approach was used for calculations of high-pressure hydrogen self-ignition. The reservoir pressure range, when a shock wave is formed in the air that has sufficient intensity to produce self-ignition of the hydrogen–air mixture, is found. An analysis of governing physical phenomena based on the experimental and numerical results of the initial conditions, i.e., the hydrogen pressure inside the vessel, and the shape of the tube in which the hydrogen was discharged, and physical mechanisms that lead to combustion is studied.

The results have shown that increases in the initial pressure in the high-pressure chamber decrease the distance from the burst location to the hydrogen ignition on the contact surface. And governing mechanisms of hydrogen self-ignition in tubes are established to be diffusion ignition on the contact surface assisted by the boundary layer influence.

2.1.3 Study on effect of the burst pressure and flame initiation outside tube

Mogi et al.[30] experimentally investigate the phenomenon of self-ignition and explosion during discharge of high-pressure hydrogen. Before their work, a few investigations have been conducted into the effect of burst pressure or the size and shape of a discharge aperture and piping on the possibility of self-ignition. And it is not mentioned whether the self-ignition in a tube propagates outside of the tube to initiate a hydrogen-jet flame.

For this reason, they try to clarify the ignition conditions of high-pressure hydrogen according to the storage pressure, the size of the discharge aperture,

nozzle length and others. A diaphragm was used to allow rapid discharge of the high-pressure hydrogen. The burst pressure was varied from 4 to 30 MPa. The downstream geometry of the diaphragm was a flange and extension pipes, with the pipe length varying from 3 to 300 mm. And two different diameters, 5mm and 10 mm, of the nozzle were used.

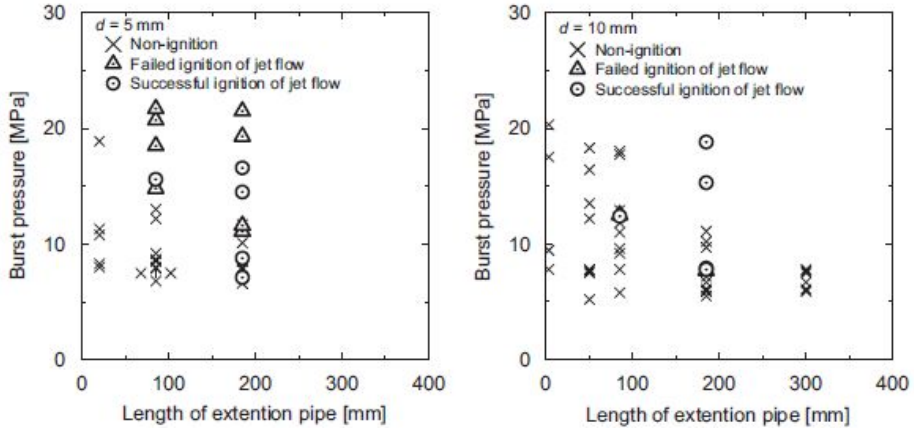

Figure 2-4 Relationship between burst pressure and length of extension pipe

It was confirmed that self-ignition did occur when a nozzle was fitted to the discharge orifice. The results demonstrated the possibility of self-ignition at high pressure even with a short nozzle. It was observed that the frequency of self-ignition of jet-flows increased with increasing length of the discharge tube. Furthermore, the pressure at which these ignitions occurred appears to be decreasing with increasing length. In addition, it was confirmed that the blast from the fireball formed on self-ignition of the hydrogen jet caused an extremely rapid pressure rise.

2.2 Numerical Studies

2.2.1 Investigation of flame development inside and outside tube

Wen et al.[31] reported numerical investigation of hydrogen self-ignition phenomenon through releases via a length of tube. They try to mimic a potential accidental scenario involving release through instrument line.

The implicit large eddy simulation (ILES) approach was used with the 5th-order weighted essentially non-oscillatory (WENO) scheme. A mixture-averaged multi-component approach was used for accurate calculation of molecular transport. The thin flame was resolved with fine grid resolution, 15 ~ 30 μm and the auto-ignition and combustion chemistry were accounted for using a Saxena and Williams' 21-step kinetic scheme.

The results showed that the finite rupture process of the initial pressure boundary plays an important role in the spontaneous ignition. The rupture process induces significant turbulent mixing at the contact region via shock reflections and interactions. The predicted leading shock velocity inside the tube increases during the early stages of the release and then stabilizes at a nearly constant value which is higher than that predicted by one-dimensional analysis. The air behind the leading shock is shock heated and mixes with the released hydrogen in the contact region. Ignition is firstly initiated inside the tube and then a partially premixed flame is developed. Significant amount of shock-heated air and well developed partially premixed flames are two major factors providing potential energy to overcome the strong under-expansion and flow divergence following spouting from the tube.

Parametric studies were also conducted to investigate the effect of

rupture time, release pressure, tube length and diameter on the propensity of spontaneous ignition. It was found that a slower rupture time and a lower release pressure will lead to increases in ignition delay time and hence reduces the chance of spontaneous ignition. If the tube length is smaller than a certain value, even though ignition could take place inside the tube, the flame is unlikely to be sufficiently strong to overcome under-expansion and flow divergence after spouting from the tube and hence is likely to be quenched.

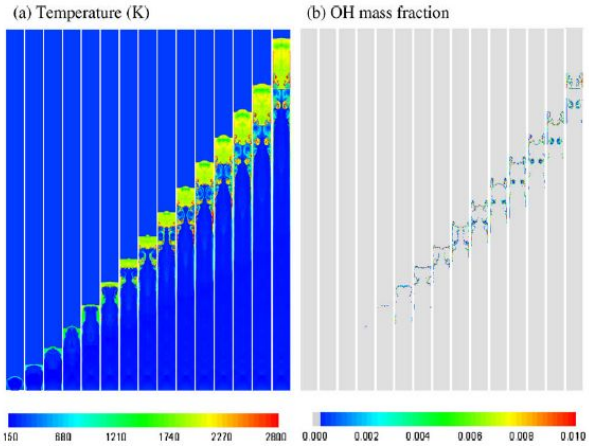

Figure 2-5 Temperature and OH mass fraction inside the extension tube

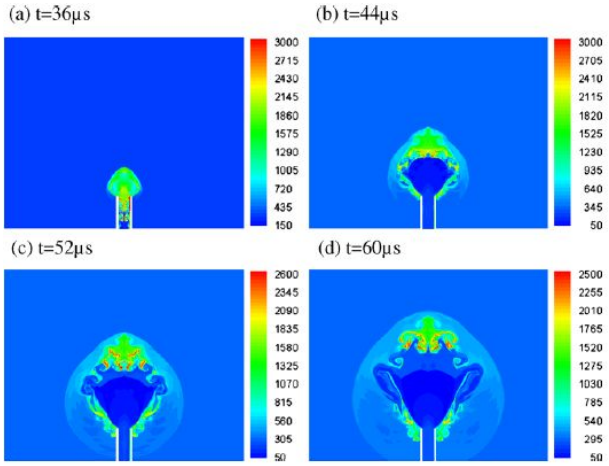

Figure 2-6 Temperature distribution outside the extension tube

2.2.2 Investigation of the flow development and spontaneous ignition inside tube

Lee et al.[32] numerically investigated detailed flow development and spontaneous ignition. There had been several numerical studies of spontaneous ignition of pressurized hydrogen exiting from tubes into air. However, the development of multi-dimensional transient flows and subsequent mixing process in the downstream tubes, associated with the failure of a rupture disk, has not been investigated in detail in most of these numerical studies. In the study, a direct numerical simulation with detailed reaction kinetics is conducted to investigate the transient flow development and the mechanism of spontaneous ignition when hydrogen is released into the air through a downstream tube by the failure of a rupture disk, with a realistic assumption of its failure geometry and conditions based on one of the experiments of Dryer et al.[28], as an effort to demonstrate their postulation.

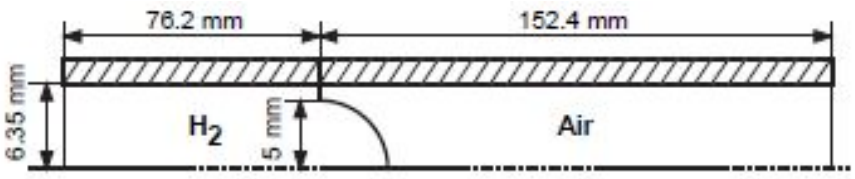

Figure 2-7 Computational domain and pressure boundary shape

By introducing a realistic assumption of the failure geometry of the pressure boundary, the simulation allows for a visualization of the process of flow development and the spontaneous ignition of hydrogen released through a tube.

The multi-dimensional shock reflections and shock-boundary layer interactions with the contact surface are responsible for the early ignition near

the boundary layer. The shock–shock interactions, shock focusing, and the formation of a jet with an accompanying vortex produce a sufficient volume of mixture of the expanding jet and shocked air in the main flow region and cause spontaneous ignition, resulting in a complete flame region across the section of the tube. The findings from the study were in good agreement with the experimental observations and accompanying postulations of Dryer et al.

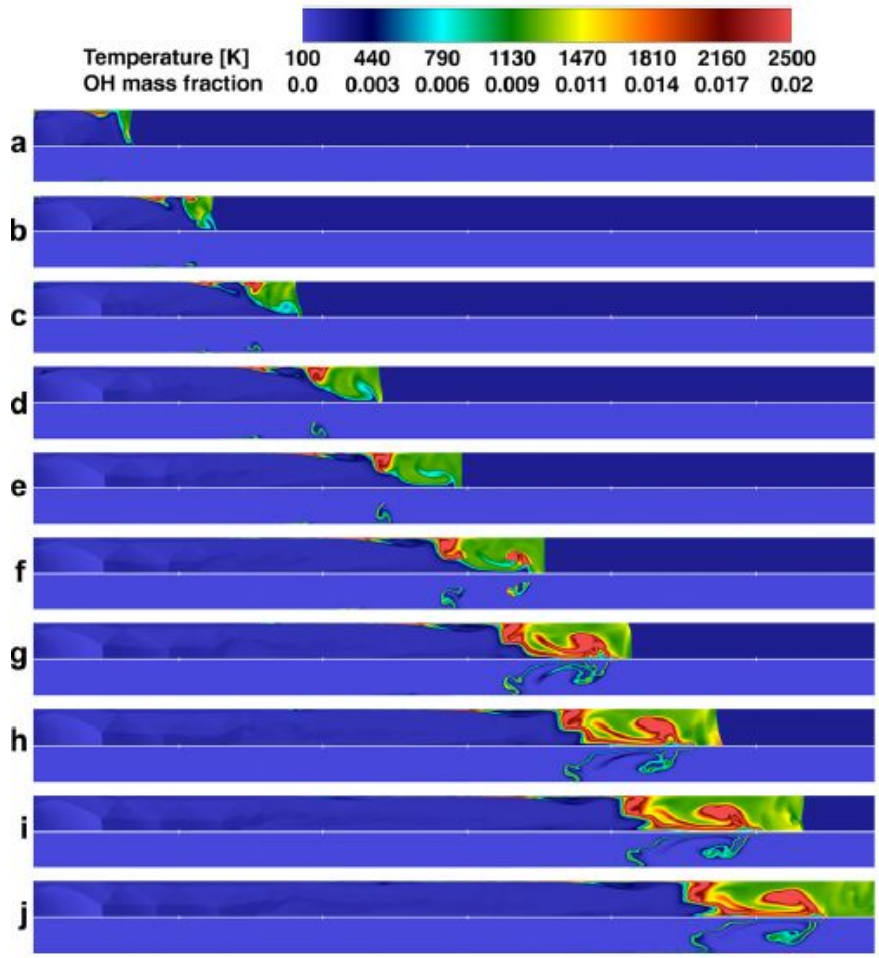

Figure 2-8 Temperature and OH mass fraction inside the extension tube

Chapter 3

Experimental Setup

In this study, both the experimental and numerical methods have been applied to understand the spontaneous ignition phenomena. In the present chapter, test facility configuration, experimental apparatus design, measurement device specifications such as that of pressure transducers or photodiodes, and techniques used to visualize shock wave and flame propagation is introduced. At the end of the chapter, the experiment procedure is explained in detail from the boosting up to the data analysis process.

3.1 Experimental apparatus

The experimental research in this study uses two different experimental systems. The system mainly consists of two parts: the boosting part and the testing part. The boosting part is commonly used for both systems.

3.1.1 Boosting Part

Many of the research directly connected a chamber before the tube to a hydrogen gas cylinder (about 130 atm) for the experiment. These were possible since the pressure of interest was limited to low pressure, and since gas loss due to the experiment was small, repetitive experiment were possible.

However, in order to perform experiments which the diaphragm burst pressure is higher than the gas cylinder pressure, an additional experimental apparatus is required to boost up the pressure.

In this research, the boosting part is designed and manufacturing using air-driven-gas-booster (Haskel, AG-152) in order to boost up a commercial gas cylinder up to 400 atm. The boosting part is also configured with a first storage tank, which can hold up to 2 liter of pressurized hydrogen. The structure of the boosting part is shown in figure 3-1.

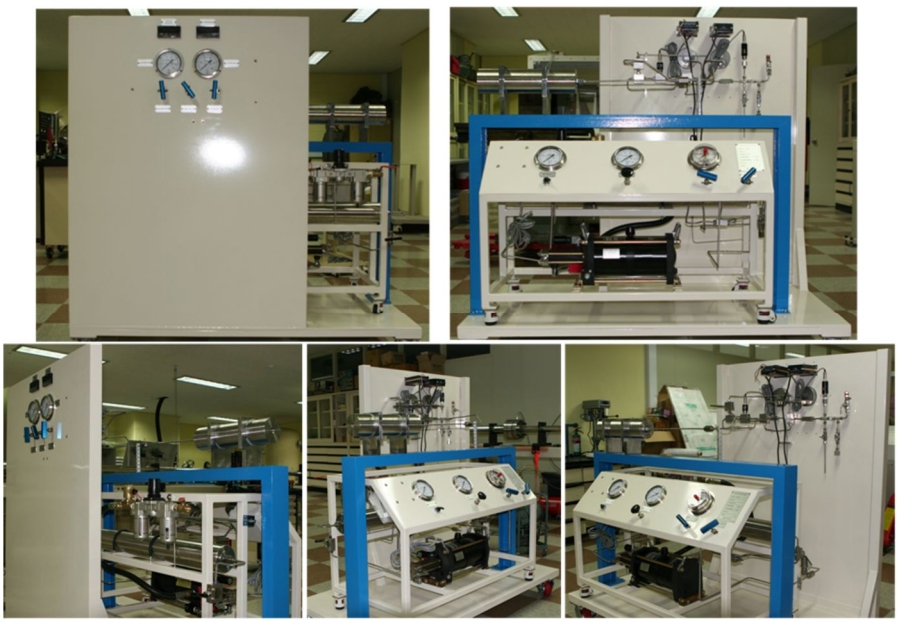

Figure 3-1 Experimental apparatus; boosting part

Three pressure indicators exits in the Gas booster: the first gauge indicates the air source pressure for driving the booster, the second gauge indicates the gas regulator pressure which connects the gas cylinder with the booster input, and the third gauge indicates the storage pressure, which is equipped with an electrical switch that can set two high and low limit of the

storage. The switched attached to the third gauge automatically controls the booster by turning it off when the pressure level is higher than the high limit, and turns it back on when the pressure level is lower than the lower limit. In this way, safety issue is resolved by limiting excessive pressure boosting and at the same time continuous experiment is possible by maintaining certain pressure level

3.1.2 Test part I ; Ignition phenomena with tube length

In order to investigate the effect of the diaphragm burst located between the high pressure hydrogen tank and the extension tube, on the ignition phenomena, a secondary storage tank and variety lengths of extension tubes are used.

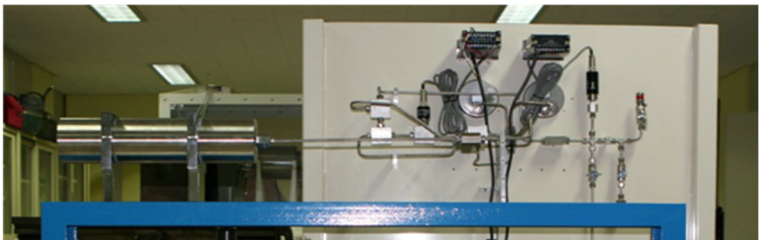

Figure 3-2 Secondary chamber and high pressure piping

Figure 3-3 Front section with control valves

Figure 3-2 shows the 0.5 liter secondary tank chamber and the high pressure piping of the test section. The piping are connected to the chamber with valves, and high pressure hydrogen stored in the tank is fed into the chamber depending on the opened amount of the valves, which are shown in figure 3-3. When the diaphragm bursts, unnecessary hydrogen loss can be prevented by closing the valve.

Figure 3-4 shows the combination of a disk holder, a rupture disk and a downstream tube. The commercial rupture disk for a pipe of 1/2 inch (Fine disk, Korea) which is made of metal (SUS) is inserted inside the disk holder and fixed and sealed by a disk ring which has tapered shape. The commercial diaphragm is made using same material from a lot and the burst pressure is guaranteed from continuous qualification tests. Although the diaphragm can be bought in small quantities, the expenses go up for non-standard bursting pressure diaphragms. Since the disk ring is made of a soft material in order to allow metal sealing, caution is required when assembling to prevent the wrinkling that causes the leakage. Additionally to this, check procedure is required to make sure whether the disk is in the right position and whether the holder, disk, ring and tube are fit to be sealed.

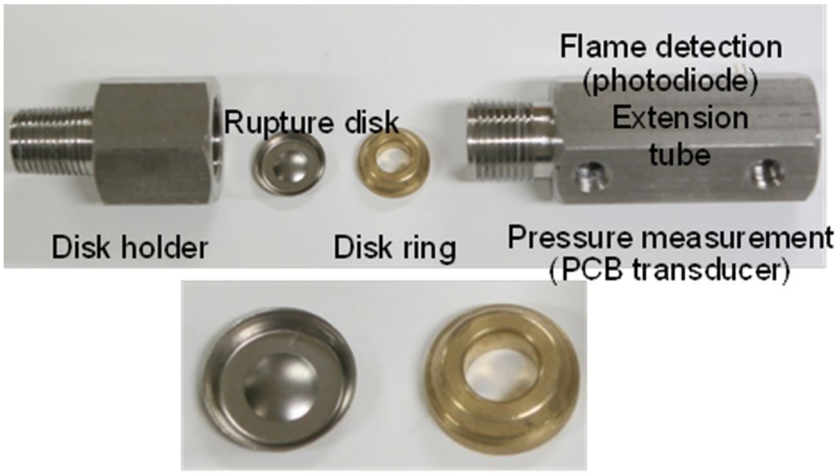

Figure 3-4 Picture of a disk holder, rupture disk, and extension tubes

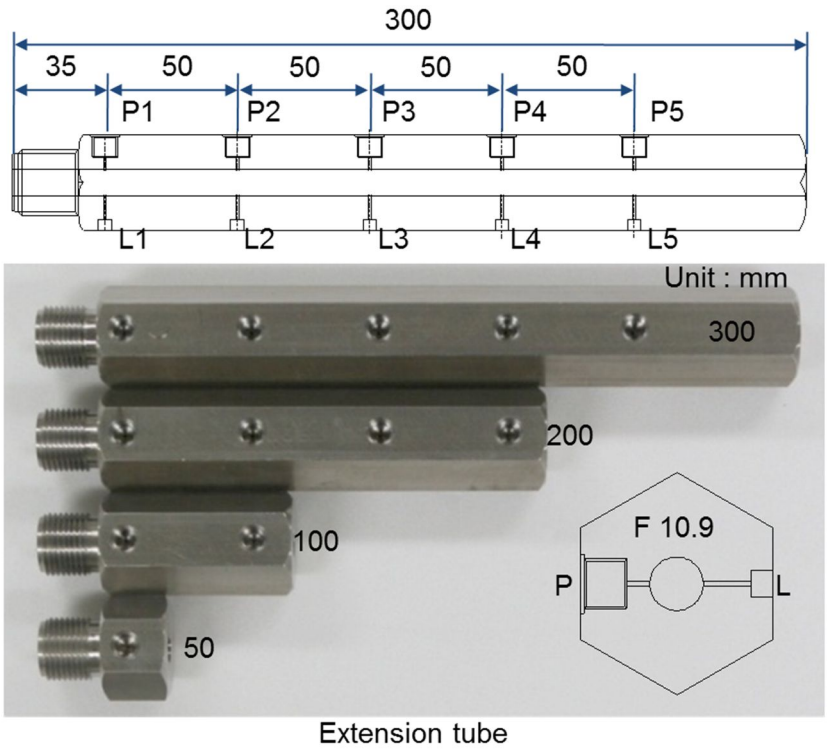

Figure 3-5 Drawing and model of the extension tubes

The disk holder is directly connected to the secondary chamber, and the inner diameter of the holder, the ring, and the tube is equally designed to be 10.9 mm in order to prevent change in shock strength due to non-uniform area. In this experiment, 50, 100, 200, and 300 mm length tubes are used in order to investigate the effect of extension tube length on the ignition phenomena. Each tube is manufactured as a whole in order to prevent any additional disturbances due to manufacturing process such as notches and etc. Figure 3-5 shows a drawing and an actual extension tube used in the experiment

3.1.2 Test part II ; Effect of the obstacle on the ignition phenomena

For the experiment investigating the effect of an obstacle on the ignition phenomena, the test apparatus consists of a test part of 3 mm inner diameter extension tube and a mechanism simulating an outer obstacle. Figure 3-6~3-8 shows the tubes and secondary chambers for different length constraints. Two different kinds of tubes are used in the experiment. When the tube is shorter than 5*D* (*D* is the diameter of the tube), the flange type tube is adopted, as shown in Figure 3-5; otherwise, the screw type tubes are adopted. The cylinders, a secondary chamber, of both types are designed to have the same volume.

In the study, due to inner diameter reduction to 3 mm, commercial rupture disk could not be used, so Mylar (Toray Advanced Materials Korea Inc.) is used as a diaphragm. Mylar is a poly ethylene plastic film, widely used as product wrappers. Mylar is manufactured by either extension or compression, and the Mylar used in the experiment is manufactured by extension, which is more ductile and thus it endures to higher pressure levels. However, since the burst pressure of the Mylar differs according to the gas

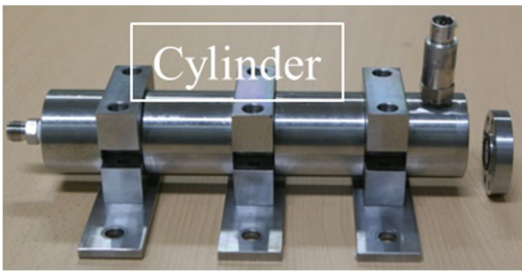

Figure 3-6 10mm test tube and secondary chamber

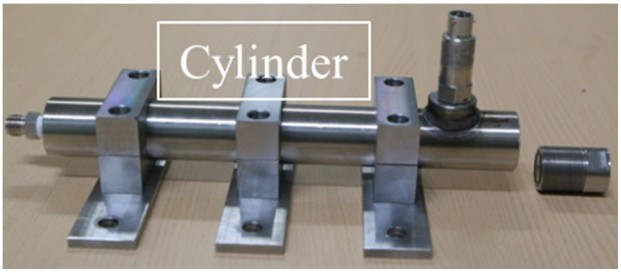

Figure 3-7 34mm test tube and secondary chamber

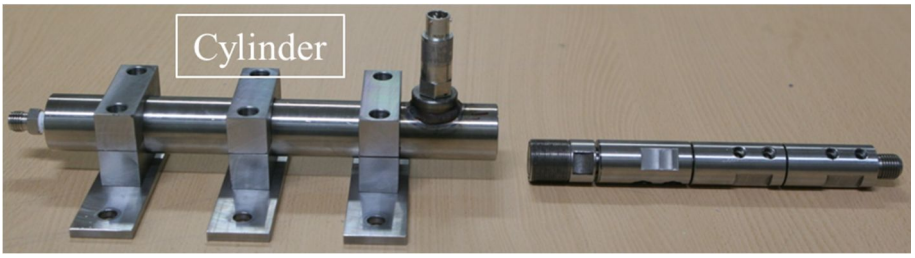

Figure 3-8 200mm test tube and secondary chamber

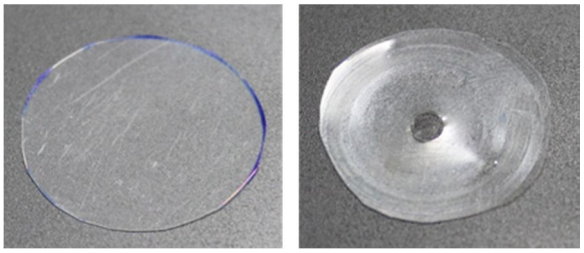

Figure 3-9 Mylar diaphragm before and after rupture

feeding speed, and considering the fact that the Mylar bursts after it expands to a certain point, it is hard to reproduce the same experimental condition.

The diameter of the extension tube is fixed to 3 mm and the length of the tube is varied from 10 to 200 mm.

3.2 Data Acquisition System

In order to analyze the self-ignition phenomena as high pressure hydrogen is released, pressure and illumination measurement within the tube and both direct and shadow graph image is visualized using a high speed camera. This section further focuses on each of the data acquisition techniques.

3.2.1 Pressure Measurement

Measurement location

In order to accurately measure the propagation speed of the shockwave due to the diaphragm burst as high pressure hydrogen is released, and in order to receive a trigger signal for the data acquisition system, several pressure transducers are mounted in the tube.

Considering safety issues related to high pressure usage and mounting of pressure transducers, the thickness of the tube has been designed to be thick enough, and the number of the sensors has been selected so that no interference occurs between the sensors (minimum 2 ~ maximum 5).

As the result of the design, in the case of the 10.9 mm inner diameter tube, the distance between the sensors are 50 mm and the first sensor upstream is located 35 mm from the diaphragm due to the screw mechanism

for fixing the diaphragm. On the other hand, in case of the 3 mm inner diameter tube, it is configured so that the 50 mm tubes are connected to each other in order to allow length variation, and the distance between the sensors is 16 mm, and the sensors between the connecting edges is 34 mm due to its connecting mechanism. Especially in the case of the 10 mm and 34 mm length tubes, there were not enough space to mount the sensors, and thus pressure data were no acquired for tube lengths shorter than 50 mm. In case of the tubes longer than 50mm the closest sensor was located 59 mm away from the diaphragm.

Mounting Mechanism

Figure 3-10 shows the sensor mounting method in the present study. The influences of pressure transducer size have been investigated by White [33] and Schewe [34]. According to their results, in order to detect the small scale of turbulent fluctuations, smaller transducers were recommended. In addition, it has been informed that the installation flushness of transducer was very serious factor which influences on the quality of fluctuations surface pressure data by Hanly [35]. He evaluated flushness effects on transducer signal amplitude, power spectral density, coherence and narrow band convection velocity and showed that a very slight protruding of transducer produced adverse effects on the measurements of desired pressure fluctuation, whereas a light submerged transducer produced only small effect. Therefore, instead of being slightly deteriorated its frequency response characteristics, in order to raise spatial resolution effects, dummy drilled holes with 0.5~1 mm diameter are applied in present experiments as shown is Figure 3-10.

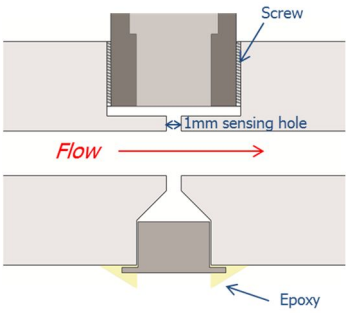

Figure 3-10 Mounting mechanism for pressure transducer and photo diodes

Characteristics of used pressure transducer

Three types of pressure transducers are used in the experiment. In order to accurately measure the formation and propagation of shockwaves within the tube, dynamic pressure transducers (Piezoelectric type) are used. As a piezoelectric type sensor, dynamic sensors (113A series & 111A series) by manufactured PCB (USA) are used. The dynamic pressure sampled over 400 kHz using data-acquisition system. The DAQ board used in this study is PCI-6133, which is made by National Instrument (NI) and can sample eight channels / card at the same time. The picture and detailed specifications of the pressure transducers are listed in Figure 3-11 and Table 3-1.

Figure 3-11 PCB Pressure Transducer (111A & 113A Series)

Table 3-1 Specification of the pressure transducers

	111A26	113B22
Measurement Range	3448 kPa	34474 kPa
Sensitivity (±10%)	1.45 mV/kPa	0.145 mV/kPa
Resolution	0.07 kPa	0.14 kPa
Rise Time	≤1.5 μsec	≤1.0 μsec
Sensing Element	Quartz	Quartz
Sensing Geometry	Compression	Compression

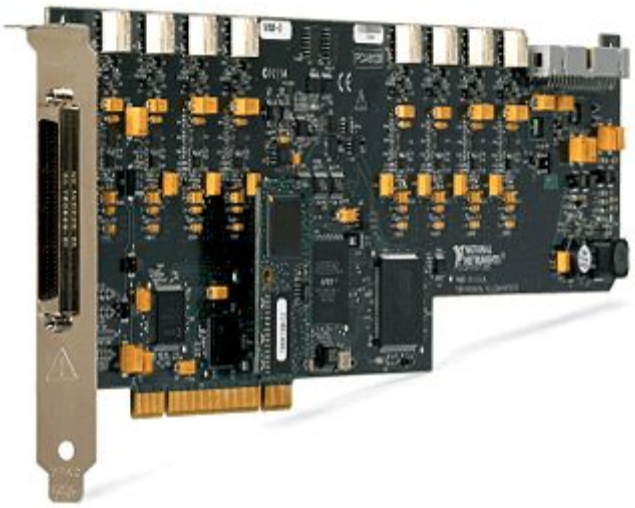

Figure 3-12 National Instruments PCI-6133 DAQ board

Table 3-2 Specifications of PCI-6133 Multifunction DAQ

Analog Input Characteristics	
Number of Channels	8
ADC Resolution	14 bits, 1 in 16,384
Sampling rate	3.0 MS/s per channel
Analog Trigger	
Level	±Full scale
Resolution	8 bits, 1 in 256
Hysteresis	Programmable

3.2.2 Light Signal Measurement

Measurement location

In this experiment, illumination detection was performed in the exactly same location as the pressure measurement. As the structural characteristics of an axisymmetric tube, there is enough space for sensor mounting on each of the symmetric locations. In other words, for the 10.9 mm inner diameter tubes, the sensors were 50 mm apart from each other and in case of 3 mm inner diameter tubes, the sensors were 16 mm / 34 mm / 16 mm / … / 34 mm / 16 mm apart from each other.

Mounting mechanism

Unlike the pressure transducers, the photodiodes do not come with the mount. Therefore in order for the photodiodes to stand the shockwaves, while detecting light signal from the self-ignition, super glue is used to fix the sensor to the tube and epoxy is used to further support its fixture.

Characteristics of used photodiode sensors

In the experiment two different types of photodiodes are used. In order to investigate the phenomena, two types of measurement gauge are installed. The photodiodes (Panasonic, PNZ 300F) as a light detector are installed at the opposite side wall from the PCB sensors. In case of the experiment using the 3 mm inner diameter tube, photodiodes (Hamamatsu, S1336-18BQ) were mounted on the wall to get more accurate measurement for this small inner diameter tube. In figure 3-13 and table 3-3 shows the photodiode and the specification of each photodiode. These two diodes have slightly different structure.

Figure 3-13 Picture of photodiode ; PNZ300(left), S1336(right)

Table 3-3 Specifications of the photodiode

	PNZ300	S1336
Type	Si Pin diode	Si photodiode
Feature	High-speed response Wide directivity	High sensitivity Low dark current
Reverse Voltage(V)	50	5
Peak sensitivity wavelength	800	960
Response time	1 ns	0.1 μs

3.2.3 Measurement of Burst Pressure

The bursting pressure of a rupture disk is measured using a pressure transducer (Sensys, PMHA 1000). However an experiment for the effect of an obstacle, slightly different technique was implemented. When a shorter tube is examined (less than 50 mm), the DAS monitors the real time pressure in the cylinder and triggers the high-speed camera as soon as the pressure decreases after the diaphragm bursts. An accurate burst pressure can be measured from the peak value recorded by the transducer (Kulite, ETM-HT-375-5000G) installed at the end of the cylinder.

3.2.4 Schlieren or Shadow Flow Visualization

Light Propagation through Inhomogeneous Media

Light propagates uniformly through homogeneous media. But the media is not uniform; it is full of disturbances and inhomogeneity due to turbulence, thermal convection, weather phenomena, and whatnot. These disturbances change the local density on a relatively-small scale and with it the refractive index. Since the wave front of light is always perpendicular to its rays, it starts bent.

Light slows upon interacting with matter. The refractive index $n=c_0/c$ of a transparent medium indicates this change, where c is the light speed in the medium and c_0 is the celebrated universal speed limit, $3x10^8$ m/s, of light in a vacuum.

For air and other gases there is a simple linear relationship between the refractive index and the gas density rho;

$$n-1=k\rho \tag{3-1}$$

The Gladstone-Dale coefficient, k, is about 0.23 cm^3/g for air at standard conditions, given visible illumination. For other gases it may vary roughly from 0.1 to 1.5. In substance, however, the refractive index of common gases varies only in the third or fourth decimal place. Also from equation (3-1), n is weakly dependent upon rho. A change in air density of two orders of magnitude causes only a 3% change of n.

The refractivity (n-1) of a gas, depends upon gas composition, temperature and density, and the wavelength of illumination. In many cases the temperature, density, and pressure of gases not far from atmospheric conditions are further related by the simple perfect-gas state equation,

$$p = \rho RT \tag{3-2}$$

where R is the specific gas constant. Flowing gases with variable density are called compressible flows; they can arise due to temperature differences or high gas speeds. All these possibilities lead to gas disturbances that refract light, and that may be visualized by virtue of this refraction.

Schlieren / Shadow graph visualization

Schlieren or shadow graph flow-visualization is a well-estabilshed technique that is used to capture the density change due to a shock and/or expansion waves.

To understand the basics of schlieren imaging, it helps to begins as simply as possible with two lenses, geometric optics and a point light source.

As shown in figure 3-14, the light from a point source is collimated by a lens. And a second lens refocuses the beam to an image of the point source.

From there, the light proceeds to a viewing screen where a real inverted image of the test area is formed. At this point the optical system is merely a projector, imaging opaque objects in the test area as silhouettes on the screen. Transparent schlieren objects are not imaged at all until a knife-edge is added at the focus of the second lens. In practice, this knife-edge is usually just an ordinary razor blade.

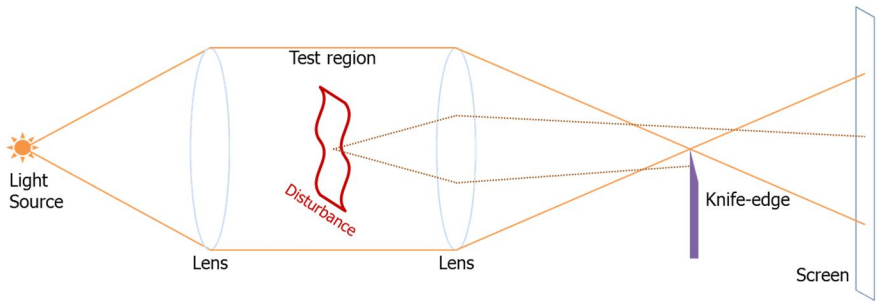

Figure 3-14 Diagram of a simple schlieren system with a point light source

As the knife-edge advances toward the focal point, nothing happens until it rather suddenly blocks the image of the light source, causing the screen to go dark. Thus one has the choice of a bright or a dark screen: bright field or dark field in the language of microscopy. Choosing the former let the knife-edge be positioned just prior to blocking the image of the source point.

If we now add schlieren object S to the test area, it bends light rays away from their original paths. Despite this, however, the second lens focuses the ray from each point in S to a corresponding point in the screen image. Two such rays are shown in figure 3-14 one bent upward, the other downward. Both refracted rays miss the focus of the optical system. The upward-deflected ray brightens a point on the screen, but the downward-deflected ray hits the knife-edge. Its corresponding image point is dark against a bright

background. For this particular point of the schlieren object, the phase difference causing a vertical gradient $\partial n / \partial y$ in the test area is converted to an amplitude difference, and the invisible is made visible.

Generalizing from this example of individual rays, finite schlieren object refracts many such rays in many directions. All downward components of these ray deflections are blocked by the knife-edge, painting at least a partial picture of the schlieren object on the screen in shadows on a bright background. The oversimplified example system of figure 3-14 will shortly be improved, but nevertheless this is the essence of the schlieren effect.

Those who said it were strictly correct, but they exaggerated the difficulty. An Opaque mask with a circular hole can be used in place of the knife-edge to get around this issue if necessary, but that approach has other problems that will become clear later. In practice, a single knife-edge judiciously oriented is often good enough. To illustrate this, three actual schlieren images of the same phenomenon with different cutoffs are shown in figure 3-15 [36].

To conclude, the point-source schlieren system discussed in this section is good for illustration, but not very practical. Its operations are on-or off, with infinitive sensitivity over zero measuring range [33]. In order to take real schlieren pictures like those shows below, an extended light source is generally required.

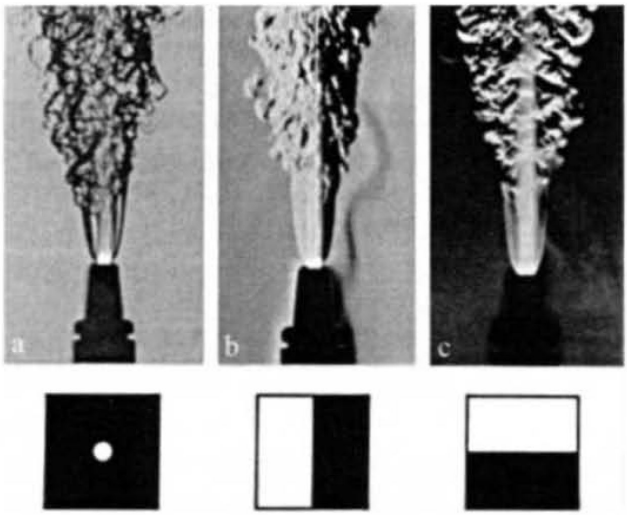

Figure 3-15 Schlieren photographs of the turbulent flame and mixing phenomena: **a** circular cutoff, **b** vertical knife-edge, **c** horizontal knife-edge

The Z-Type Schlieren System

When the size of test section is large, the necessary light beam must have a large diameter, In this case, the use of spherical mirrors is preferable to the one of lenses, which is fairly expensive. Spherical, parabolic, and off-axis concave mirrors are often used in schlieren equipment. But by far the most popular arrangement is the z-type Herschellian system using two oppositely-tilted, on-axis telescopic parabolas, as shown in figure 3-16. The combination of a diverging illuminator beam, an opposite converging analyzer beam, and a parallel beam between the two mirrors suggests the letter z, whence the name.

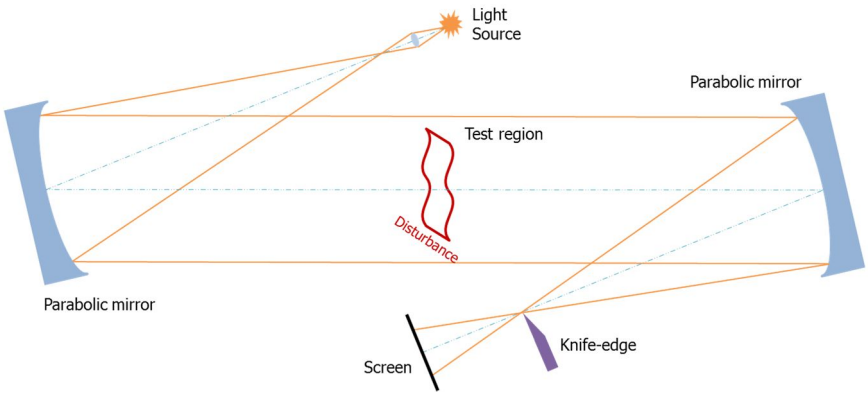

Figure 3-16 Z-type Schlieren arrangement

Though titled, the mirrors are usually symmetrical, on-axis parabolas. Specially-figured off-axis parabolas are quite expensive, and are unnecessary if large-f/number on-axis mirrors are chosen and are carefully aligned [37]. The advantages of parallel light, stated above for lens-type systems, apply equally to the z-type mirror schlieren system. The advantage of mirrors in place of lenses is primarily found in a larger field-of-view for a given cost.

A minimum distance between the field mirrors of about 2f, where f is the mirror focal length, is required to provide space for the test area. Longer distances between mirrors do not matter in principle. To shorten the overall length, plane first surface folding mirrors can be used in the illuminator and analyzer beams. These make the system somewhat more difficult to align and more prone to vibration sensitivity. They also exacerbate optical aberrations by increasing the off-axis angles [38]. Nevertheless they can be essential in cramped quarters.

A Z-type four-mirrored system, in which two planar mirrors are added to the conventional Z-type two-mirrored system described in Ref. [39], are used to obtain the focal distance from the continuous light source to the concave

mirror.

Distinction between Schlieren and Shadowgraph Methods

Schlieren and shadowgraph methods are closely related, but there are several distinctions [40, 41]. First, the shadowgraph is not a focused optical image; it is a mere shadow. The schlieren image, however, is what it purports to be: an optical image formed by a lens, and thus bearing a conjugate optical relationship to the schlieren object. Second, schlieren methods require a knife-edge or some other cutoff of the refracted light, where no such cutoff is needed or allowed in shadowgraph. Finally, the luminance level in a schlieren image responds to the first spatial derivative of the refractive index in the schliere, e.g. $\partial n / \partial x$. The shadowgraph, however, responds to the second spatial derivative or Laplacian, e.g. $\partial^2 n / \partial x^2$. Equivalently, the schlieren image displays the deflection angle ε while shadowgraph displays the ray displacement resulting from the deflection.

Despite these distinctions, both schlieren and shadowgraph are integrating optical systems that project line-of-sight information onto a viewing screen or camera focal plane. As such, they are most appropriate for 2D phenomena but still qualitatively useful for any phenomenon. Even when the object under study is non-planar, we nonetheless assume an equivalent object plane in which the ray deflections appear to lie [42].

Another distinction between schlieren and shadowgraph techniques lies in the apparatus and the effort required. The great advantage of shadowgraph is its extreme ease. So little is needed that natural shadowgraph appear all around us without the use of any high technology. Schlieren effects also appear naturally in more limited circumstances, but they stand out best in the

laboratory using lamps, mirrors, and lenses.

In favor of shadowgraph, note that it readily allows large-scale visualizations and it shows the salient features of a subject without gross changes in illumination. Though it is less sensitive than schlieren in general, particular circumstances can make it more sensitive. For example, $\partial^2 n / \partial x^2$ can be much larger than $\partial n / \partial x$ in gas flows involving shock waves or turbulence, both of which occur around supersonic projectiles [43], for example. Shadowgraph renders, by way of its double differentiation, fine-scale images of turbulent flow [44, 45]. Shock waves, being natural step-function, produce strong higher derivatives of refractive index that cause them to stand out as stark lines in a shadowgraph.

For weaker disturbances overall, however, schlieren holds the advantage of much higher sensitivity. Its unambiguous 1:1 image correspondence with the object of study is often a decisive benefit. It emphasizes, even exaggerates detail in the schlieren object [46] where shadowgraph usually downplays it. Thus many fields of application are open to the superior sensitivity and adaptability of the schlieren method that are closed to the simpler shadowgraph technique.

3.2.5 Obtains High Speed Image

Very fast image capturing is required in order to capture the self-ignition phenomena of high pressure hydrogen release due to diaphragm burst, since the phenomena occurs within a few ms. In order to obtain these images, Phantom, v710 high speed camera is used, which is capable of capturing 1.4 million frames image per second. The resolution depends on the number of images taken, and in this experiment, 37,000 to 200,000 images per second

are captured. And parts of the total recorded frames were used for pre-triggering which captured images before the camera was triggered.

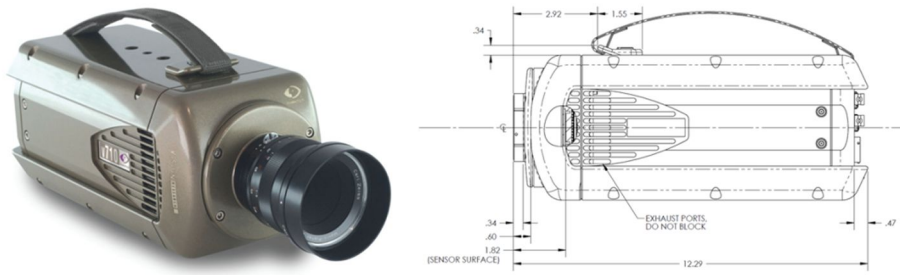

Figure 3-17 Picture and drawing of v710 high-speed camera

Table 3-4 Specifications of Phantom v710

Maximum capacity	1,400,000 pictures-per-second
Resolution	128x8(min) to 1280x800(max)
Imaging sensor	CMOS sensor 1280 x 800 pixels
Pixel size	20 μm
Triggering	Programmable trigger location

3.3 Test Procedure

Although two different tests have been performed, the test procedure is quite similar to each other. The test procedures of the experiment are as follows:

For the experiment setup procedure, an extension tube is selected, depending on the length and inner diameter. Then, pressure transducers and photo diodes are mounted onto the extension tube, which are connected to the DAQ system via BNC cables. The first pressure transducer signal triggers both the DAQ system and the high-speed cameras. Then, the rupture disk is selected, which depends on the test pressure and the test type. The rupture disk is inserted between the storage tank and the extension tube, as the extension tube is mounted onto the end of the second storage tank, as shown in figure 3-18. Final assembly test procedure is carried out in order to ensure the rupture disk is inserted properly and to check whether there are any leakage spots.

After the experiment setup procedure is finished, the boosting procedure is carried out. A vacuum pump is used to pump out any air within the first storage tank, which has a volume of 2 liter, tank in order to prevent the hydrogen from premixing with air before the burst. Then, in to supply the burst pressure for the experiment, hydrogen is boosted up to 40 MPa into the first storage tank, using the air-driven-gas booster. This relatively large tank is employed to avoid a sudden pressure jump in the test cylinder, which can lead to sudden release at an unexpected pressure. When the pressure of the first tank is increased to a sufficient value, the boosting procedure terminates.

As the boosting procedure terminates, the feeding procedure is carried out by feeding hydrogen to the second storage tank, which the volume is 0.5 liter, by opening the needle valve shown in figure 3-18. The feeding continues until the rupture disk bursts, thereby resulting in the sudden release of hydrogen into the atmosphere through downstream of the extension tube. At the moment the rupture disk bursts, the feeding procedure terminates as the needle valve is closed to cut excessive hydrogen flowing into the extension tube. Then, the DAQ system and high-speed cameras are examined to check whether the triggering occurred properly, and whether the acquired data is valid. A portion of the data, which contains just before and throughout the burst process, is selected since most of the other data is insignificant. Lastly, disassemble procedure is carried out by unplugging the cables, unmounting the tube, and checking the shape of the burst-rupture disk. The whole experiment is terminated and is ready to be prepared for the next experiments to follow.

Figure 3-18 Schematics of the test facilit showed schematics of the test facility and wiring.

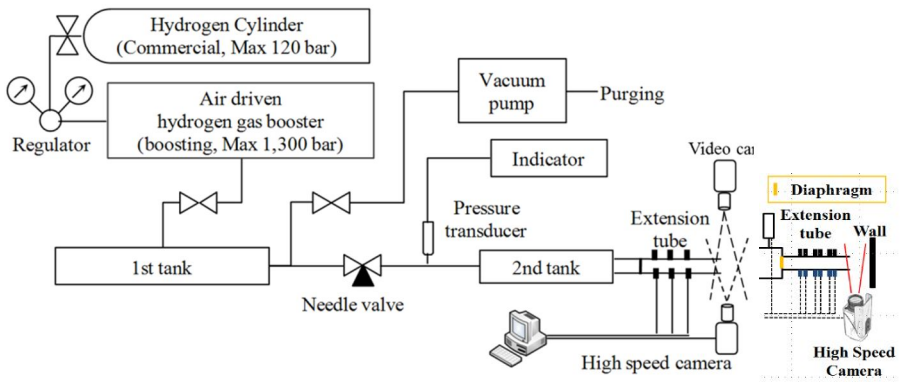

Figure 3-18 Schematics of the test facility

Chapter 4
Numerical Simulation

When highly pressurized hydrogen is released through a tube, shock and expansion wave is generated due to the pressure difference across the diaphragm. If the pressure difference is large enough to heat the air inside the tube over a certain value, reaction between air and hydrogen is triggered. In this chapter, numerical methods, i.e. solution scheme, integrated external libraries, kinetic model, to simulate the spontaneous ignition inside a tube is introduced. Lastly in the chapter, the boundary conditions and computational domains used in the simulation are presented.

4.1 Numerical Method

4.1.1 Governing Equation

The numerical simulation, which tries to observe the spontaneous ignition of the sudden release hydrogen, is required to integrate rigorously formulated numerical models. Because of the phenomena included such as strong shock, expansion waves, turbulence, chemical reaction, the models should be capable of shock-capturing, contact-resolving, entropy-satisfying, enthalpy-preserving, and conservation-satisfying.

The governing equations are the unsteady, compressible, axisymmetric,

multi-species Navier-Stokes equations with chemical reaction source terms, for mixtures of thermally perfect gases,

$$Q_t + F_x + G_y = Fv_x + Gv_y + Sg + Sc \tag{4-1}$$

where each term has 13 components in this study and it can be extracted as follow,

$$Q_t = \frac{\partial}{\partial t}\begin{pmatrix} \rho \\ \rho u \\ \rho v \\ \rho E \\ \rho Y_H \\ \vdots \\ \rho Y_{N_2} \end{pmatrix}, \qquad F_x = \frac{\partial}{\partial x}\begin{pmatrix} \rho u \\ \rho u^2 + p \\ \rho uv \\ \rho uH \\ \rho uY_H \\ \vdots \\ \rho uY_{N_2} \end{pmatrix}, \qquad G_y = \frac{\partial}{\partial y}\begin{pmatrix} \rho v \\ \rho uv \\ \rho v^2 + p \\ \rho vH \\ \rho vY_H \\ \vdots \\ \rho vY_{N_2} \end{pmatrix},$$

$$Fv_x = \frac{\partial}{\partial x}\begin{pmatrix} 0 \\ \tau_{xx} \\ \tau_{xy} \\ \beta_x \\ \rho D^c \dfrac{\partial Y_H}{\partial x} \\ \vdots \\ \rho D^c \dfrac{\partial Y_{N_2}}{\partial x} \end{pmatrix}, \qquad Gv_y = \frac{\partial}{\partial y}\begin{pmatrix} 0 \\ \tau_{xy} \\ \tau_{yy} \\ \beta_y \\ \rho D^c \dfrac{\partial Y_H}{\partial y} \\ \vdots \\ \rho D^c \dfrac{\partial Y_{N_2}}{\partial y} \end{pmatrix}$$

$$S_g = \frac{1}{y}\begin{pmatrix} -\rho v \\ -\rho uv + \tau_{xy} \\ -\rho v^2 + (\tau_{yy} - \tau_{hh}) \\ -\rho vH + \beta_y \\ -\rho vY_H + \rho D^c \dfrac{\partial Y_H}{\partial y} \\ \vdots \\ -\rho vY_H + \rho D^c \dfrac{\partial Y_{N_2}}{\partial y} \end{pmatrix}, \qquad S_c = \begin{pmatrix} 0 \\ 0 \\ 0 \\ 0 \\ \dot{\omega}_H \\ \vdots \\ \dot{\omega}_{N_2} \end{pmatrix}$$

$$\tau_{xx} = \frac{2}{3}\mu\left(2\frac{\partial u}{\partial x} - \frac{\partial v}{\partial y} - \alpha\frac{v}{y}\right), \quad \tau_{yy} = \frac{2}{3}\mu\left(2\frac{\partial v}{\partial y} - \frac{\partial u}{\partial x} - \alpha\frac{v}{y}\right),$$

$$\tau_{xy} = \mu\left(\frac{\partial u}{\partial y} + \frac{\partial v}{\partial x}\right),$$

$$\beta_x = \tau_{xx}u + \tau_{xy}v + \kappa\frac{\partial T}{\partial x} + \dot{Q}_x, \quad \beta_y = \tau_{xy}u + \tau_{yy}v + \kappa\frac{\partial T}{\partial y} + \dot{Q}_y$$

4.1.2 Flux Scheme

For the accurate and robust resolution for shock and moving contact discontinuities, the AUSM-DV scheme with shock-fix and entropy-fix [47] extended to chemically reacting flows is employed. A second order, both in time and in space, finite volume method of Strang type splitting the hyperbolic and source operators is applied. For the hyperbolic part, directional splitting of second order is applied while the MUSCL-Hancock method with slope limited variables is used for each direction.

ASUM-DV scheme

AUSM-DV[47] is a mixture of AUSMD and AUSMV and is proposed to eliminate the overshoots behind the shock. The scheme is seems to solve the problem of overshoots and oscillations near a wall, successfully. However in this method, the advantages of AUSM, i.e. non-existence of carbuncle phenomena and the satisfaction of entropy condition, is not preserved. For this reason, shock-fix and entropy-fix has been applied. In this method, the normal momentum flux has been modified.

$$\left(\rho u^2\right)_{1/2\,AUSMDV} = \frac{1}{2}(1+s)\left(\rho u^2\right)_{AUSMV} + \frac{1}{2}(1-s)\left(\rho u^2\right)_{AUSMD} \quad (4\text{-}2)$$

where s is a switching function of the pressure gradient

$$s = \min\left(1, K\frac{|p_R - p_L|}{\min\left(p_R, p_L\right)}\right), \qquad 0 \le s \le \frac{1}{2} \quad (4\text{-}3)$$

This averaging is biased toward the ASUMV in order to take merit of the shock capturing property.

Shock fix is applied to fix the carbuncle phenomenon. It consists of two steps as follows,

- Find the compressible sonic points across the cell interface. The point exists when

$$\begin{cases} u_L - c_L > 0 & \text{and} \quad u_R - c_R < 0 \\ \text{or} \quad u_L + c_L > 0 & \text{and} \quad u_R + c_R < 0 \end{cases} \quad (4\text{-}4)$$

If a shock sonic point is found between grid point j and j+1 in the ξ-direction, set the flag at j and j+1 to 1, $S_{\xi,j}=1,\ S_{\xi,j+1}=1$. Do same procedure in other directions.

- In calculating a numerical flux in the ξ-direction between j and j+1 grid, *S* except for the ξ-direction are used to sense the shock position, to which some dissipative scheme is applied.

$$\begin{cases}\text{dissipative scheme if} \quad \left(S_{\eta,j}+S_{\eta,j+1}+S_{\varsigma,j}+S_{\varsigma,j+1}\right)\geq 1,\\ \text{nondissipative scheme otherwise}\end{cases}$$

The numerical fluxes in other directions are computed in a similar way.

And another fix, the entropy fix, is applied to fix unrealistic problem near the expansion region. There are two cases where an expansive sonic point is found across the cell interface.

$$\begin{cases}\text{Case A.}\quad u_L-c_L<0 \quad\text{and}\quad u_R-c_R>0,\\ \text{Case B.}\quad u_L+c_L<0 \quad\text{and}\quad u_R+c_R>0,\end{cases}$$

Then a numerical dissipation is only applied when a single expansion wave is found, modifying the flux $F_{1/2}$ to $F_{1/2,E-Fix}$

$$\begin{cases}\text{Case A.}\quad F_{1/2,E-Fix}=F_{1/2}-C\Delta\left(u-c\right)\Delta\left(\rho\Psi\right)\\ \text{Case B.}\quad F_{1/2,E-Fix}=F_{1/2}-C\Delta\left(u+c\right)\Delta\left(\rho\Psi\right),\qquad \Delta(\ )\equiv(\ )_R-(\ )_L\end{cases}$$

MUSCL-Hancock scheme

The MUSCL-Hancock method in two-dimension consist of three steps. The first is to obtain reconstructed data and boundary-extrapolated value. The cell averages $U_{i,j}^{n}$ are reconstructed using slope vectors Δ_i, Δ_j.

$$U_{i,j}^{-x} = U_{i,j}^{n} - \frac{1}{2}\Delta_i, \quad U_{i,j}^{+x} = U_{i,j}^{n} + \frac{1}{2}\Delta_i \tag{4-5}$$

$$U_{i,j}^{-y} = U_{i,j}^{n} - \frac{1}{2}\Delta_j, \quad U_{i,j}^{+y} = U_{i,j}^{n} + \frac{1}{2}\Delta_j \tag{4-6}$$

where $U_{i,j}^{+/-}$ is the boundary-extrapolated value. The next step is to obtain the evolution of boundary-extrapolated values,

$$\hat{U}_{i,j}^{-x} = U_{i,j}^{-x} + \frac{\Delta t}{2\Delta x}\left[F\left(U_{i,j}^{-x}\right) - F\left(U_{i,j}^{+x}\right)\right] - \frac{\Delta t}{2\Delta y}\left[G\left(U_{i,j}^{-y}\right) - G\left(U_{i,j}^{+y}\right)\right] \tag{4-7}$$

$$\hat{U}_{i,j}^{+x} = U_{i,j}^{+x} + \frac{\Delta t}{2\Delta x}\left[F\left(U_{i,j}^{-x}\right) - F\left(U_{i,j}^{+x}\right)\right] - \frac{\Delta t}{2\Delta y}\left[G\left(U_{i,j}^{-y}\right) - G\left(U_{i,j}^{+y}\right)\right] \tag{4-8}$$

$$\hat{U}_{i,j}^{-y} = U_{i,j}^{-y} + \frac{\Delta t}{2\Delta x}\left[F\left(U_{i,j}^{-x}\right) - F\left(U_{i,j}^{+x}\right)\right] - \frac{\Delta t}{2\Delta y}\left[G\left(U_{i,j}^{-y}\right) - G\left(U_{i,j}^{+y}\right)\right] \tag{4-9}$$

$$\hat{U}_{i,j}^{+y} = U_{i,j}^{+y} + \frac{\Delta t}{2\Delta x}\left[F\left(U_{i,j}^{-x}\right) - F\left(U_{i,j}^{+x}\right)\right] - \frac{\Delta t}{2\Delta y}\left[G\left(U_{i,j}^{-y}\right) - G\left(U_{i,j}^{+y}\right)\right] \tag{4-10}$$

The last step is to obtain the solution of the Riemann problem. At intercell position, boundary-extrapolated values are used.

4.1.3 Stiff Solver

For the chemical reaction source term, adaptive, implicit stiff ODE solver of RADAU5[48] is applied, and for the rest of the non-stiff source terms standard RK2 is used.

RADAU5

If the dimension of the differential equation $y' = f(x, y)$ is n, then the s-stage fully implicit Runge-Kutta method involves a *n-s* dimensional nonlinear system for the unknowns $g_1,\ldots,g_s$. The s-stage fully implicit RK method is

$$g_i = y_0 + h\sum_{j=1}^{s} a_{ij} f(x_0 + c_j h, g_j) \qquad i = 1,...,s \qquad (4\text{-}11)$$

$$y_1 = y_0 + h\sum_{j=1}^{s} b_j f(x_0 + c_j h, g_j) \qquad i = 1,...,s \qquad (4\text{-}12)$$

To solve this problem, the processes Radau IIA of Ehle, which are L-stable and of high order, is used with s=3 and p=5. This specific case is called as RADAU5. The method has distinctive advantages. By reformulating the nonlinear system, it could reduce the chance of round-off errors amplification during the iteration. For a general nonlinear differential equation the system has to be solved iteratively. Replacement of all Jacobians in the Newton's methods by an approximation makes only one LU-decomposition be needed which is expensive procedure. However this method basically solves the matrix and needs matrix inversion. Because of this characteristic, RADAU5 could not be used when the number of components involved is large.

4.1.4 Chemistry Solver

As shown in figure 4-1, CANTERA[49] is a set of software tools for problems involving chemical kinetics.

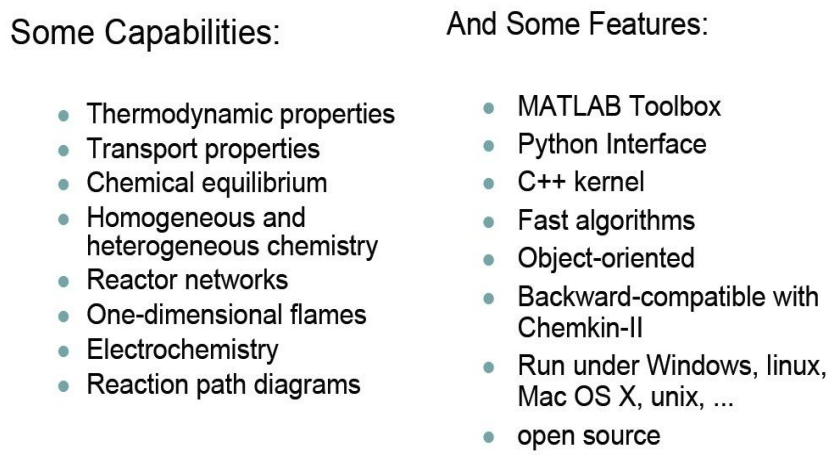

Figure 4-1 Capabilities and features of CANTERA

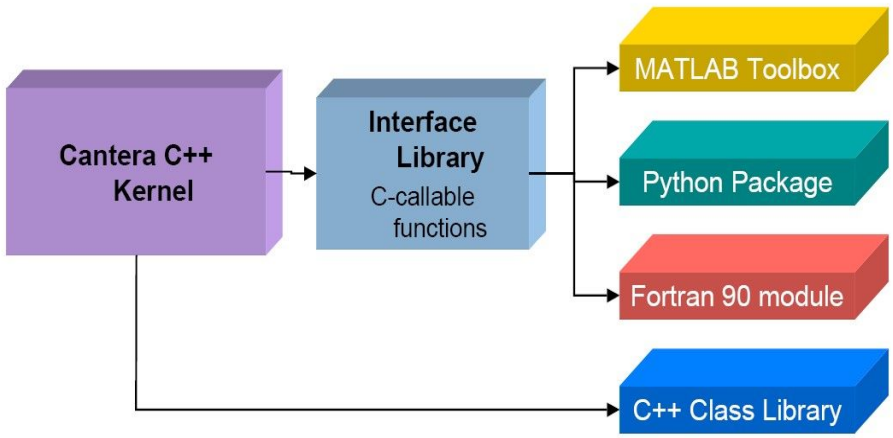

Figure 4-2 Multilinguality of CANTERA

CANTERA can be used from several popular programming, problem-solving environments, interactive or scripting environments like MATLAB and Python for rapid problem solution and software prototyping. And for

large-scale computation, CANTERA can be used from fortran 90 and C++.

The kernel of CANTERA is a C++ class library which is designed for performance. To achieve better performance CANTERA integrates property caching, sparing virtual methods, templates which used to allow inlining at compile time and standard template library container classes. Property caching means expensive reaction rates only recomputed when temperature actually changes. This can help save time in Jacobian evaluation. And by explicitly handling reactions with one, two, or three reactants, it has efficient kinetics performance. Moreover standard open-source numerical libraries like BLAS, LAPACK and CVODE are used.

For chemical equilibrium calculation, CANTERA uses element potential method. The method is one of several equivalent 'non-stoichiometric' algorithms proposed by Smith and Missen. Element potentials are the chemical potentials of the atomic vapor species. With these, all other chemical potentials can be computed from equation of reaction equilibrium for the atomization reactions. And it computes partial and total pressures for selected element potentials.

This adjustment is done until the pressure and the elemental composition have desired values. This procedure requires solving nonlinear system of M, usually less than 5, algebraic equations. Initial estimation is get by solving linear programming problem. If the initial guess is close enough to the solution, variations on Newton's method work well.

To compute reactors, CANTERA integrates primitive conservation equations with no assumption of equation of state or boundary conditions. And same reactor objects may be used to build constant-volume reactors, constant-pressure ones, CSTRs, etc.

$$\frac{dM_k}{dt} = \sum_{inlets} \dot{m}_i Y_{k,i} - Y_k \sum_{outlets} \dot{m}_o + V\hat{m}_k \dot{\omega}_k \tag{4-13}$$

$$\frac{dU}{dt} = \sum_{walls} A_i \dot{q}_i - P\dot{V} + \sum_{inlets} \dot{m}_i h_i - h \sum_{outlets} \dot{m}_o \tag{4-14}$$

$$Y_k = \frac{M_k}{M}, \qquad T = T\left(\frac{U}{M}, Y_1, \ldots, Y_K\right) \tag{4-15}$$

Temperature is determined by Newton iterations.

As seen in figure 4-1, CANTERA has a capability of transport properties calculation. All transport-related tasks are handled by interchangeable transport property managers. Transport models may be swapped dynamically during a simulation. The manager allows adaptive transport property evaluation. In regions of small gradients, CANTERA uses simple and fast models. But in regions of high gradients like boundary layers, flame fronts, it uses accurate models.

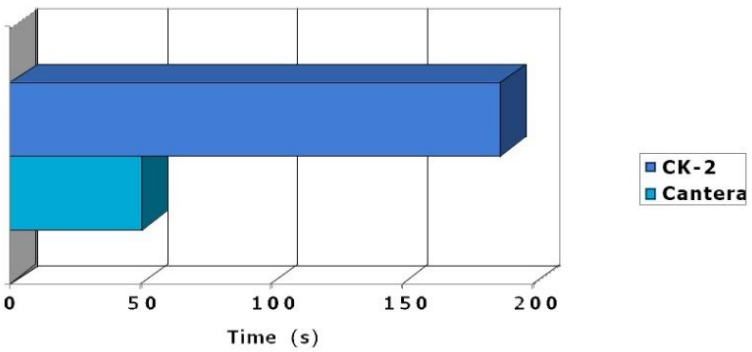

Figure 4-3 Benchmark kinetics performance vs CHEMKIN-II

In case of multi-transport, transport model based on that of Kee, Dixon-Lewis, Warnatz, Coltrin and Miller is implemented. With this model,

CANTERA computes viscosity, binary diffusion coefficients, multicomponent diffusion coefficients, thermal conductivity, and thermal diffusion coefficients. Making some enhancements over Kee et al., it cuts time to solve L-matrix by 50%, uses slightly more accurate and faster collision integral fits, and direct computes fluxes. The result of a performance test of CANTERA vs CHEMKIN-II is shown in figure 4-3.

4.1.5 Chemical Reaction Model

To compute chemical reactive flows, together with three basic equations, rate equation is also needed. The rate law or rate equation for a chemical reaction is an equation which links the reaction rate with concentrations or pressures of reactants and constant parameters (normally rate coefficients and partial reaction orders). To determine the rate equation for a particular system one combines the reaction rate with a mass balance for the system. For a generic reaction, $A + B \rightarrow C$, the simple rate equation (as opposed to the much more common complicated rate equations) is of the form:

$$r = k(T)[A]^m [B]^n \tag{4-16}$$

In this equation, $[X]$ expresses the concentration of a given X, usually in mol/liter. The $k(T)$ is the reaction rate coefficient or rate constant, although it is not really a constant, as it includes everything that affects reaction rate outside concentration such as temperature but also including ionic strength, surface area of the adsorbent or light irradiation. And reaction rate constants usually are highly temperature dependent. A modified three

parameter Arrhenius form,

$$k_{f,i}(T) = AT^{\beta} e^{-E_a/RT} \tag{4-17}$$

is usually flexible enough to describe the temperature dependency of $k_{f,i}$ over a wide range of temperatures. Equation (4-17) differs from the usual Arrhenius expression through the additional T^{β} term.

The exponent n and m are the reaction orders and depend on the reaction mechanism. The stoichiometric coefficients and the reaction orders are very often equal, but only in one step reactions, molecularity (number of molecules or atoms actually colliding), stoichiometry and reaction order must be the same. Complicated rate equations are not of the form above, and they can be a sum of terms like it or have quantities in the denominator.

The rate equation is a differential equation, and it can be integrated in order to obtain an integrated rate equation that links concentrations of reactants or products with time.

For example, consider a system of oxygen in chemical equilibrium at $p = 1$ atm and $T = 3000K$. The oxygen under these conditions should be partially dissociated. Thus, in our system, both O_2 and O will be present in their proper equilibrium amounts. Now, assume that somehow T is instantaneously increased to, say, $4000K$. Equilibrium conditions at this higher temperature demand that the amount of O_2 decrease and the amount of O increase. However this change in composition takes place via molecular collisions, and hence it takes time to adjust to the new equilibrium conditions. During this non-equilibrium adjustment period, chemical reactions

are taking place at a definite net rate.

Continuing with this example of a system of oxygen, the only chemical reaction taking place is

$$O_2 + M \qquad 2O + M \tag{4-18}$$

where M is a collision partner; it a can be either O_2 or O. In terms of notation, a bracket notation, where $[O_2]$, $[N_2]$, etc. denote the concentrations of O_2, N_2, etc. Using the bracket notation for concentration, we denote the number of moles of O_2 and O per unit volume of the mixture by $[O_2]$ and $[O]$, respectively. Empirical results have shown that the time rate of formation of O atoms via equation (4-18) is given by

$$\frac{d[O]}{dt} = 2k[O_2][M] \tag{4-19}$$

where $d[O]/dt$ is the reaction rate, k is the reaction rate constant, and equation (4-19) is called a reaction rate equation. The reaction rate constant k is a function of T only. Equation (4-19) gives the rate at which the reaction given in equation (4-18) goes from left to right; this is called the forward rate, and k is really the forward rate constant k_f:

$$O_2 + M \xrightarrow{k_f} 2O + M \tag{4-20}$$

Hence, equation (4-19) is more precisely written as follows.

Forward rate :

$$\frac{d[O]}{dt} = 2k_f \left[O_2\right]\left[M\right] \tag{4-21}$$

The reaction in equation (4-18) that would proceed from right to left is called the reverse reaction, or backward reaction,

$$O_2 + M \xleftarrow{k_b} 2O + M \tag{4-22}$$

with an associated reverse or backward rate constant k_b, and a reverse or backward rate given by the following.

Reverse rate:

$$\frac{d[O]}{dt} = -2k_b \left[O\right]^2 \left[M\right] \tag{4-23}$$

Note that in both equation (4-21) and (4-23), the right-hand side is the product of the concentrations of those particular colliding molecules that produce the chemical change, raised to the power equal to their stoichiometric mole number in the chemical equation. Equation (4-21) gives the time rate of increase of atoms because of the forward rate, and equation (4-23) gives the time rate of decrease of O atoms because of the reverse rate. However, what we would actually observe in the laboratory is the net time rate of change of O atoms caused by the combined forward and reverse reactions

$$O_2 + M \underset{k_b}{\overset{k_f}{\rightleftarrows}} 2O + M \tag{4-24}$$

and the net reaction rate is given by the following.

Net rate:

$$\frac{d[O]}{dt} = 2k_f [O_2][M] - 2k_b [O]^2 [M] \tag{4-25}$$

Now consider our system to again be in chemical equilibrium; hence, the composition is fixed with time. Then $d[O]/dt = 0$, $[O_2] \equiv [O_2]^*$, and $[O] \equiv [O]^*$ where the asterisk denotes equilibrium conditions. In this case, equation (4-25) becomes

$$0 = 2k_f [O_2]^* [M]^* - 2k_b [O]^{*2} [M]^* \tag{4-26}$$

Or

$$k_f = k_b \frac{[O]^{*2}}{[O_2]^*} \tag{4-27}$$

Examining the chemical equation just given, we can define the ratio $[O]^{*2}/[O_2]^*$ in equation (4-27) as an equilibrium constant based on concentrations K_c. Hence, equation (4-27) can be written as

$$\frac{k_f}{k_b} = K_c \tag{4-28}$$

Equation (4-28), although derived by assuming equilibrium, is simply a relation between the forward and reverse rate constants, and it holds in general for nonequilibrium conditions. Therefore, the net rate, equation (4-25), can be expressed as

$$\frac{d[O]}{dt} = 2k_f [M]\left\{[O_2] - \frac{1}{K_c}[O]^2\right\} \tag{4-29}$$

In practice, values for k_f are found from experiment, and then k_b can be directly obtained from equation (4-28). Keep in mind that k_f, k_b and K_c for a given reaction are all functions of temperature only. Also, k_f in equation (4-29) is generally different depending on whether the collision partner M is chosen to be O_2 or O.

The preceding example has been a special application of the more general case of a reacting mixture of n different species. Consider the general chemical reaction

$$\sum_{i=1}^{nsp} v_i' X_i \underset{k_b}{\overset{k_f}{\rightleftarrows}} \sum_{i=1}^{nsp} v_i'' X_i \tag{4-30}$$

where v_i and v_i represent the stoichiometric mole numbers of the reactants and products, respectively. For the preceding general reaction, equation (4-30), we write the following.

Forward rate:

$$\frac{d[X_i]}{dt} = \left(\nu_i^{"} - \nu_i^{'}\right) k_f \prod_i [X_i]^{\nu_i^{'}} \tag{4-31}$$

Reverse rate:

$$\frac{d[X_i]}{dt} = -\left(\nu_i^{"} - \nu_i^{'}\right) k_b \prod_i [X_i]^{\nu_i^{"}} \tag{4-32}$$

Net rate:

$$\frac{d[X_i]}{dt} = \left(\nu_i^{"} - \nu_i^{'}\right) \left\{ k_f \prod_i [X_i]^{\nu_i^{'}} - k_b \prod_i [X_i]^{\nu_i^{"}} \right\} \tag{4-33}$$

Equation (4-33) is a generalized net rate equation. In addition, the relation between k_f and k_b given by equation (4-28) holds for the general reaction given in equation (4-33)

The total rate of change of the concentration of the ith species caused by all of the chemical reactions is

$$\frac{d[X_i]}{dt} = \sum_{r=1}^{Nre} \frac{d[X_i]_r}{dt} \tag{4-34}$$

The components w_i, the rate of spatial change of the mass fraction of the ith species, in the chemical source term **W** are given by

$$w_i = \frac{d[Y_i]}{dt} = \frac{d[X_i]}{dt} \frac{M_i}{\rho u} \tag{4-35}$$

To use those equations, reaction mechanisms and other parameters should be decided. Because it can be obtained from experiments, there exist in the literature many sets of reactions rate parameters. In the present work, a latest comprehensive hydrogen/air kinetics model for high pressure combustion (Burke 2011) [50] consists of 19 reversible elementary reactions for 9 species, H, H2, O, O2, OH, H2O, HO2, H2O2, and N2, is used.

The model updated from the previous H2/O2 model of the same researcher to incorporate recent improvements in rate constant and transport treatment from fundamental studies as well as to improve agreement with flame speed measurements at high-pressure, dilute flame conditions, and speciation measurements in shock tube. The model is formulated in a manner that balances consistency with data for both elementary reactions and combustion behavior.

Table 4-1 H_2- O_2 Reaction rate coefficients (Burke 2011)

			A	n	E_a
1	$H+O_2=O+OH$		1.04E+14	0.00	1.531E+04
2	$O+H_2=H+OH$	Duplicate	2.82E+12	0.00	7.948E+03
		Duplicate	8.79E+14	0.00	1.917E+04
3	$H_2+OH=H_2O+H$		2.16E+08	1.51	3.430E+03
4	$OH+OH=O+H_2O$		3.34E+04	2.42	-1.930E+03
5	$H_2+M=H+H+M$		4.58E+19	-1.40	1.040E+05
	ε_{H2}=2.5, ε_{H2O}=12.0, ε_{CO}=1.9, ε_{CO2}=3.8, ε_{Ar}=0.00, ε_{He}=0.0				
	$H_2+Ar=H+H+Ar$		5.84E+18	-1.10	1040E+05
	$H_2+He=H+H+He$		5.84E+18	-1.10	1.040E+05
6	$O+O+M=O_2+M$		6.16E+15	-0.50	0.000E+00
	ε_{H2}=2.5, ε_{H2O}=12.0, ε_{CO}=1.9,				

	ε_{CO2}=3.8, ε_{Ar}=0.00, ε_{He}=0.0				
	$O+O+Ar=O_2+Ar$		1.89E+13	0.00	-1.790E+03
	$O+O+He=O_2+He$		1.89E+13	0.00	-1.790E+03
7	$OO+H+M=OH+M$		4.71E+18	-1.00	0.000E+00
	ε_{H2}=2.5, ε_{H2O}=12.0, ε_{CO}=1.9, ε_{CO2}=3.8, ε_{Ar}=0.75, ε_{He}=0.75				
8	$H_2O+M=H+OH+M$		6.06E+27	-3.32	1.208E+05
	ε_{H2}=3.0, ε_{H2O}=0.0, ε_{CO}=1.9, ε_{CO2}=3.8, ε_{O2}=1.5, ε_{N2}=2.0, ε_{He}=1.1				
	$H_2O+H_2O=H+OH+H_2O$		1.01E+26	-2.44	1.202E+05
9	$H+O_2(+M)=HO_2+(+M)$[a]	κ_∞	4.65E+12	0.44	0.000E+00
		κ_0	6.37E+20	-1.72	5.250E+02
	F_c=0.5, T^{***}=1.0E-30, T^*=1.0E+30				
	ε_{H2}=2.0, ε_{H2O}=14.0, ε_{CO}=1.9, ε_{CO2}=3.8, ε_{O2}=0.78, ε_{Ar}=0.67, ε_{He}=0.8				
	$H+O_2(+M)=HO_2(+M)$[b]	κ_∞	4.65E+12	0.44	0.000E+00
		κ_0	9.04E+19	-1.50	4.920E+02
	F_c=0.5, T^{***}=1.0E-30, T^*=1.0E+30				
	ε_{H2}=3.0, ε_{H2O}=21.0, ε_{CO}=2.7, ε_{CO2}=5.4, ε_{O2}=1.1, ε_{He}=1.2, ε_{N2}=1.5				
10	$HO_2+H=H_2+O_2$		2.75E+06	2.09	-1.451E+03
11	$HO_2+H=OH+OH$		7.08E+13	0.00	2.950E+02
12	$HO_2+O=O_2+OH$		2.85E+10	1.00	-7.239E+02
13	$HO_2+OH=H_2O+O_2$		2.89E+13	0.00	-4.970E+02
14	$HO_2+HO_2=H_2O_2+O_2$	Duplicate	4.20E+14	0.00	1.200E+04
	$HO_2+HO_2=H_2O_2+O_2$	Duplicate	1.30E+11	0.00	-1.630E+03
15	$H_2O_2(+M)=OH+OH(+M)$	κ_∞	2.00E+12	0.90	4.875E+04
		κ_0	2.49E+24	-2.30	4875E+04
	F_c=0.42, T^{***}=1.0E-30, T^*=1.0E+30				
	ε_{H2O}=7.5, ε_{H2O2}=7.7, ε_{CO2}=1.6, ε_{O2}=1.2, ε_{N2}=1.5, ε_{He}=0.65, ε_{H2}=3.7, ε_{CO}=2.8				
16	$H_2O_2+H=H_2O+OH$		2.41E+13	0.00	3.970E+03
17	$H_2O_2+H=HO_2+H_2$		4.82E+13	0.00	7950E+03
18	$H_2O_2+O=OH+HO_2$		9.55E+06	2.00	3970E+03
19	$H_2O_2+OH=HO_2+H_2O$	Duplicate	1.74E+12	0.00	3.180E+02
		Duplicate	7.59E+13	0.00	7.270E+03

4.2 Boundary Conditions

In order to numerically simulate the formation of the propagating within the extension tube as the diaphragm burst, the mixing of the hydrogen/air, and the self-ignition phenomena, the numerical method in the previous section has been used. The tube and the high pressure hydrogen chamber was assumed to have the same cross-sectional area and the length of the chamber was selected so it is long enough that the rarefaction wave does not reflect back at the end of the calculation region on the upstream, but shorter than the actual model.

Numerical analysis was performed as axisymmetric condition, since the actual model is also axisymmetric. The wall boundary condition is set to the no-slip condition. Since the flow is supersonic at the end of the tube, the condition is set to extrapolate and since the actual test chamber is long enough, the condition at the upstream end is set to be extrapolation as indicated before.

For the diaphragm separating high pressure hydrogen and the air, various shapes are considered in order to study the effect of a pressure boundary. Those pressure boundaries divided into two categories, spherical and flat, and each has branches depending on the perfectness of diaphragm burst. Detailed features are shown in the figure 4-4, the red line represents the remaining part of the diaphragm after the burst. When partial spherical boundary has been applied, the radius of the hemispherical part of the rupture disk is assumed to be about 4.45 mm. In a real configuration, high pressure hydrogen does not burst with a flat diaphragm shape. However, it does not generate multi-dimensional shock wave interaction; the result could be compared with more realistic cases. Then the effect of multi-dimensional shock on the spontaneous

ignition could be observed easily. When spherical condition is given, as in the study of Lee et al. [32], the radius is set as the radius of the diaphragm measured in the experiment.

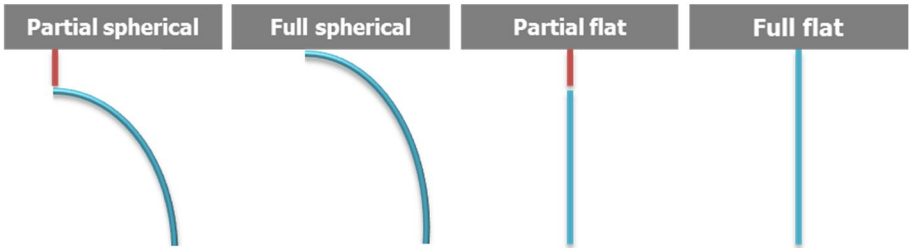

Figure 4-4 Configurations of pressure boundary (red:remaining, blue:burst)

For the case, hydrogen initially distributes spherically, and if the boundary is inside the cell, the area ratio is calculated and from the hydrogen and air ratio, the molarity of the cell is determined. When calculating the area ratio, thickness of the diaphragm is ignored. In other words, if the boundary crossed the cell, the cell is divided into 100X100 infinitesimal regions and the inner and outer corresponding cells are obtained. The area ratio of hydrogen and air is calculated by dividing the infinitesimal grid number by 10,000, and then pressure, density, temperature, concentration of each molecule is calculated. Then a physical quantity such as internal entropy is calculated using CANTERA to make the simulation more realistic. And for the simulating cases with an edge of diaphragm, the edge is assumed as a slip wall, whereas when the edge does not exist, it is assumed to be equal as a wall.

4.3 Computation Domains

In this research two different configurations are studied. When investigating the effect of burst pressure on the self-ignition phenomena, the computation domain has been constructed which is modeling the region near the diaphragm of the experiment to study the effect of burst pressure and tube length on the ignition phenomena. Figure 4-5 shows the computational domain with the location of rupture disk. The geometry of the rupture disk is changed following the type of pressure boundary. The computation domain is consisted of two regions, length of upstream region is 100 mm from the rupture disk, and the inner diameter is 10.9 mm. The downstream part of the tube is also determined as 100 mm, since an expansion wave moves only to the left-hand side, it is considered as a sufficient length. The dash-dot line in Figure 4-5 represents the symmetric line, which is the axis of the tube.

A Cartesian grid system with a uniform size of 10 μm is used downstream of the plane of the rupture disk. The total number of cells is about 8 million.

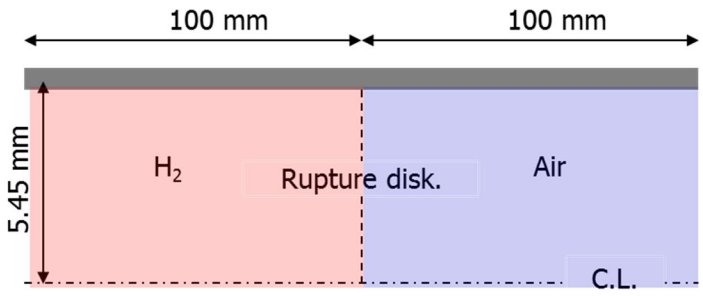

Figure 4-5 Computational domains for study on the ignition mechanism

Secondly, for the computation to investigate the effect of inner diameter of the tube on the self-ignition phenomena, the tube structure was set such that the result can be compared for tube of two different inner diameter with the length of 200 mm, the length of the chamber is 63 mm so that the reflection of expansion wave is eliminated and in order to minimize the number of grids within the given node.

Same size of Cartesian grid, 10 μm, has been used and total number of cells is 3.96 million when the inner diameter is 3 mm and 14.39 million when the inner diameter is 10.9 mm.

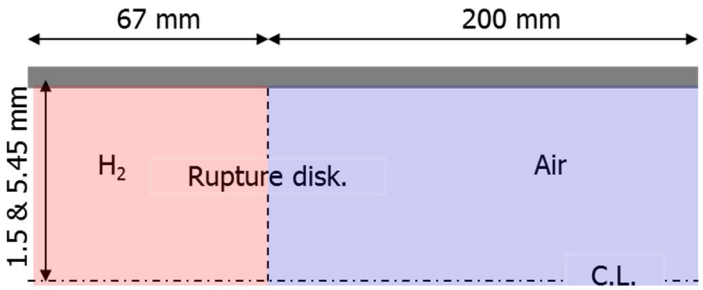

Figure 4-6 Computational domain for study of the tube diameter effect

Chapter 5
Parametric studies on spontaneous ignition mechanism of pressurized hydrogen

Although many experiments and simulations have been conducted in order to reveal the characteristics of high pressure hydrogen spontaneous ignition phenomena, there still are lot of unknowns about the conditions or the mechanisms of the spontaneous ignition. In this chapter, unexplored regions of pressure and tube length are investigated to find the relationship between the two parameters. Using numerical approach, the characteristics of flow development and flame generation inside the tube is found and the results are compared with experimental data. The numerical simulation analysis is also applied to higher pressures, at ranges which are impossible to test due to safety reasons. Moreover, according to the experiment, there are two distinctive shape of the diaphragm after the burst, depending on the material used. The effect of such pressure boundaries is also studied thoroughly. At the last part of the chapter, a research using a flat plate perpendicular to the flow spouting from the tube is introduced. The plate mimics an obstacle near the release point and the effect of this particular hindrance on flame development or ignition characteristics are analyzed using visualized images.

5.1 Effect of Tube Length

5.1.1 Identifying ignition phenomena at various conditions

In the study of Dryer et al.[28] and Mogi et al.[30], three different phenomena has been observed when high pressure hydrogen was released through the tube due to burst of a diaphragm. From the detailed comparison between these phenomena, the ignition pattern is classified as self-ignition, failed-ignition and non-ignition. Self-ignition means the flame formed within the tube and this flame developed to a diffusion flame outside the tube. Failed-ignition indicates the situation that the flame generated inside the tube does not developed to a sustainable flame when it spouts outside the tube. In a fail-ignition, a flame is generated inside the tube during the hydrogen flows downstream. However the flame is extinguished within few moments as it propagates throughout the tube, as the temperature drops due to the expansion. On the other hand, non-ignition indicates a flame is not detected inside or outside the tube and there are no evidence that indicates the reaction between the mixed hydrogen and gas. Non-ignition signifies the circumstance in which ignition or flames are not observed at all.

Dryer et al. had suggested according to experimental results that turbulent mixing is formed near the contact surface due to multi-dimensional shock from the imperfect burst of a diaphragm, and flame is formed in both the boundary layer and the core regions, and the flame is propagated as the two regions merge.

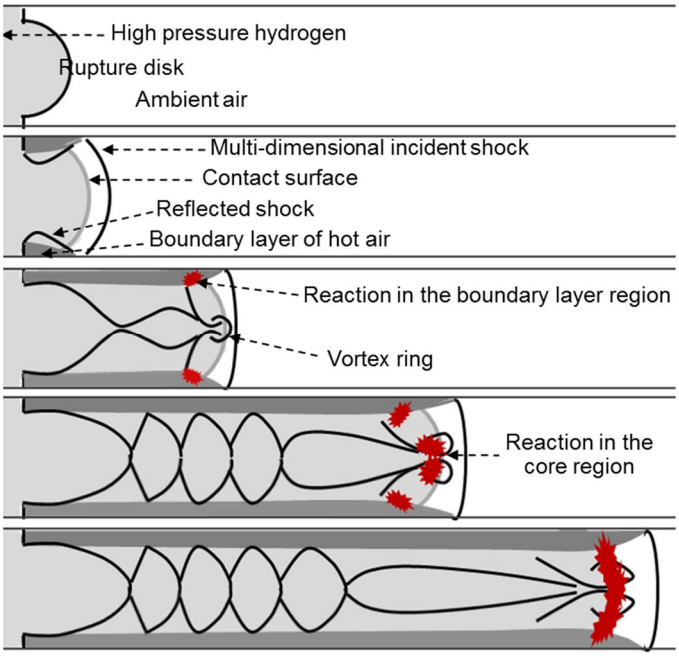

Figure 5-1 Proposed self-ignition mechanism

The model has been numerically verified by Lee et al. From the research, it is turned out that the initial stages of flow developments after the rupture of the pressure boundary have a significant influence on the rest stages. The spherical leading shock wave, which is generated as the pressure boundary ruptures, is reflected at the side wall. The shock reflection and shock-boundary layer interaction with the contact surface causes the early ignition near the boundary layer. After the reflection waves are gathered at the axis of symmetry, which is known as 'shock focusing phenomena', and causes instability resulting in the generation of a strong jet along the axis. A vortex ring, induced from the intrusion of the jet into preceding shock, mixes expending hydrogen and shock heated air which developed into a secondary ignition region. When those two reaction region, boundary layer and core region, merges a complete flame across the cross-section is generated. This

ignition mechanism is illustrated in figure 5-1.

Figure 5-2 shows flame propagation outside the tube with varying tube lengths for a bursting pressure of 10.8 MPa.[57] For a bursting pressure of 10.8 MPa, spontaneous ignition occurs only in the tube 300 mm in length; however, although not shown in the figure, a flame is not observed at all when the tube length is 50 mm. According to the previous results [28, 30, 51], it is considered that the sufficient length of the tube for the mixing of hydrogen and air is necessary so that the spontaneous ignition occurs inside the tube. Furthermore, according to Lee et al. [32], two reaction regions inside the tube may exist to effectively complete a flame region in which self-ignition occurs as the two reaction regions merge. The result obtained by Lee et al. is confirmed by the images in figure 5-2, in which the flame is observed only near the wall. After undergoing expansion, the flame near the wall weakens and is subsequently quenched after exiting the tube. However, as shown in the case of 300 mm, the flame is observed over the entire cross-section of the tube outlet and spontaneous ignition occurs.

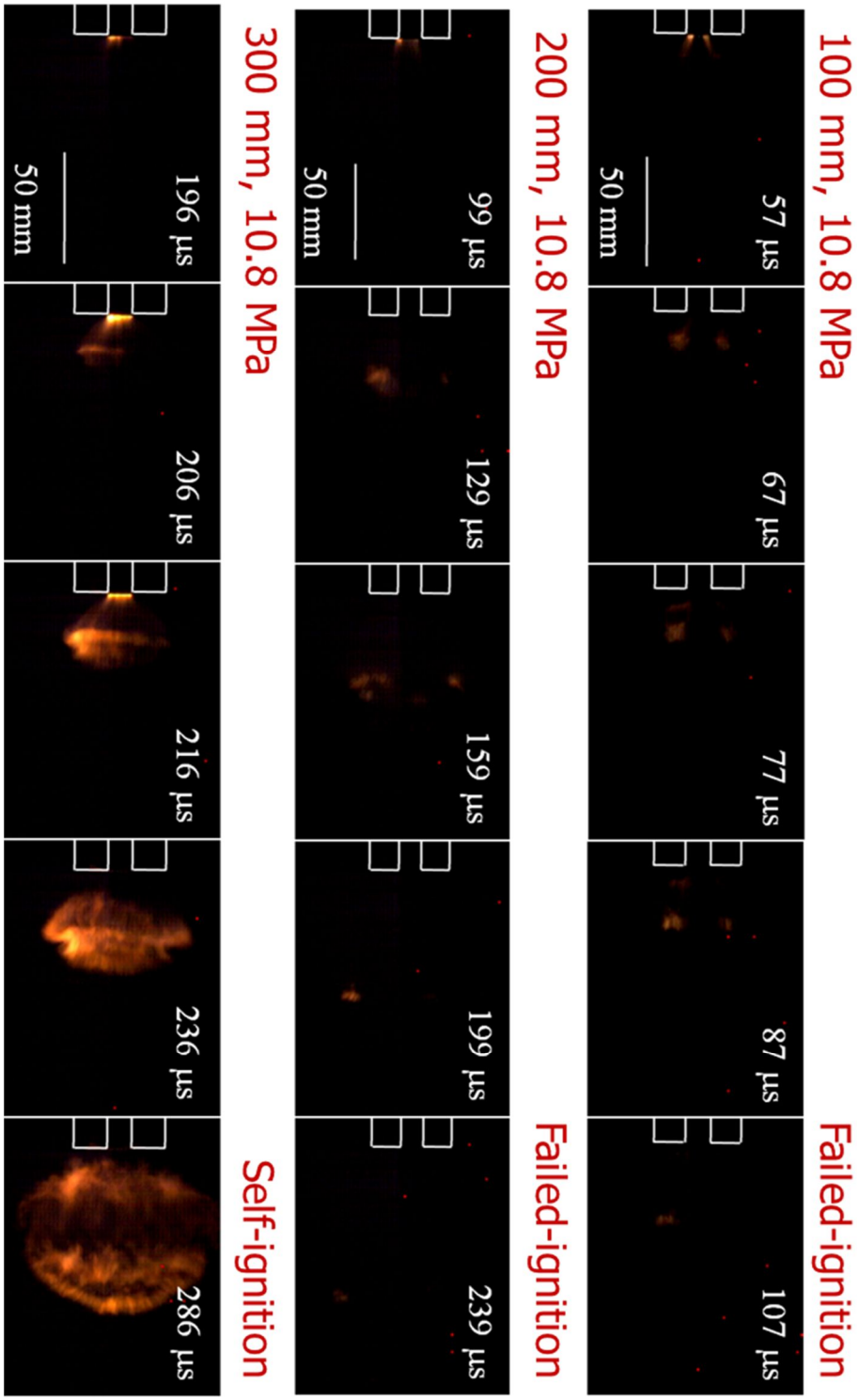

Figure 5-2 Flame propagation outside the tube

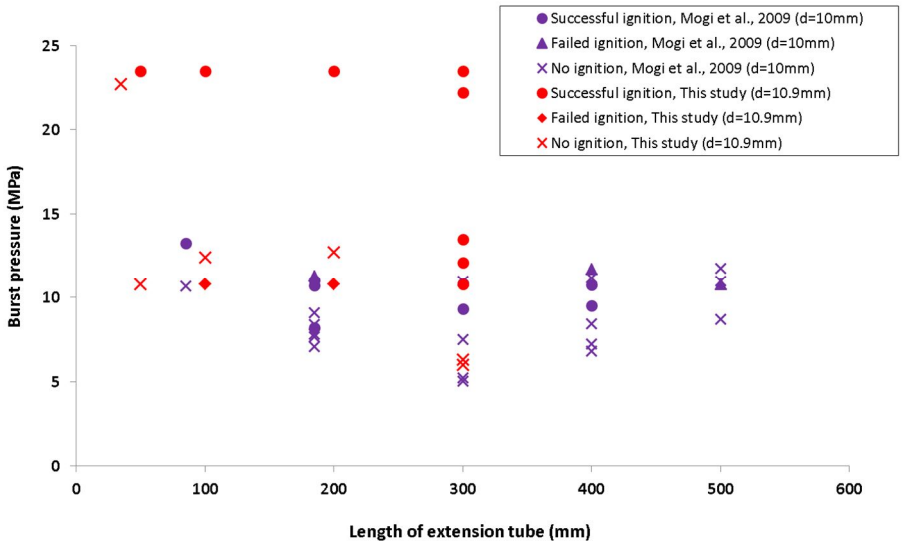

Figure 5-3 Ignition characteristics: Burst pressure vs length of extension tube (tube diameter : ~10 mm)

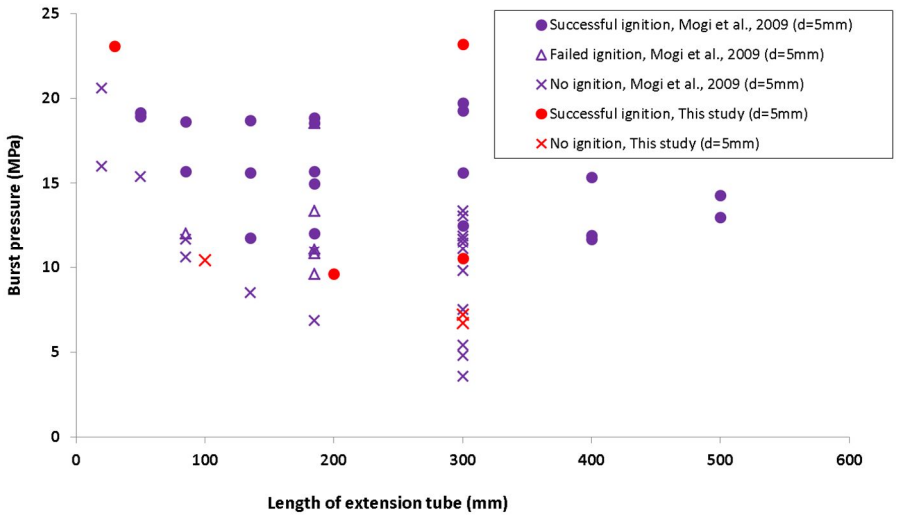

Figure 5-4 Ignition characteristics: Burst pressure vs length of extension tube (tube diameter : 5 mm)

This suggests the significance of the flame across the entire tube because it possesses the potential to sustain a diffusion flame after jetting out of the tube into the open air. Additionally, it is necessary to have sufficient length so that the mixing region is generated by multi-dimensional shock-shock interactions in order to establish a complete flame inside the tube.

Figure 5-3 and 5-4 shows the results from ignition phenomena observed as extension tube lengths are varied for various burst pressures. Additionally, the results obtained by Mogi et al. [30] are included in the figure to compare with the previous results. After self-ignition of high pressure hydrogen had been ever first verified by Wolanski and Wojcicki [20], many studies have been carried out, however verification is hard since the experimental apparatus or conditions are unknown.

However Mogi et al.'s results are comparable to the results of current study because the experimental configurations are very similar. Generally, the results show the tendency that self-ignition can occur at high bursting pressure for shorter extension tubes. However, previous results have not been reported for the cases in which the bursting pressure is higher than 20 MPa.

Mogi et al. basically showed that self-ignition does not take place for bursting pressures less than 20 MPa for the extension tubes with lengths of 20 mm or less when an inner diameter of the tube was 5 mm. Additionally, for the case in which the inner diameter was 10 mm, self-ignition was not observed for a bursting pressure of 18 MPa when the length of tube is 50 mm. In this experiment, self-ignition occurred at a bursting pressure of 23.5 MPa and a tube length of 50 mm. This result suggests that self-ignition can occur when the bursting pressure is sufficiently high, even though the extension tube is extremely short, and furthermore, it is necessary to determine the limitation

of minimum value of the burst pressure for spontaneous ignition with correlating shorter tubes of lengths less than 50 mm.

As a concern to the ignition criterion, in the paper of Mogi et al., the result is not clear comparing to a general trend when the tube length is 185 mm. A successful ignition occurs when the burst pressure is approximately 8 MPa, but failed-ignition or non-ignition is observed at bursting pressure higher than 8 MPa. In the present experiment, the flame quenches, failed-ignition, at a bursting pressure of 10.8 MPa for a tube with a length of 200 mm. The flame is finally quenched due to energy loss from expansion as the flame propagates outside the tube.

When comparing the experimental setups of our current study and Mogi et al., it is found that all the conditions in Mogi et al.'s experiments are very similar to the current study except the disk that was used. The disk used in Mogi et al.'s experiment is made of polyethylene terephthalate (PET) film. This difference means that the bursting shape of a rupture disk may be different. As in the next chapter and in the numerical simulation performed by Lee et al. [32], the shape of the diaphragm burst affects the self-ignition phenomena. Furthermore, it should be noted that flammable particles of PET can be generated when the disk bursts, which assists self-ignition. It is possible that the ambiguity of the Mogi et al.'s results originates from these causes.

5.1.2 Development of the flame inside the tube

Measured signal from the photodiode inside the tube after the successful ignition of the hydrogen jet at a bursting pressure of 23.5 MPa and tube length of 200 mm is shown in figure 5-5. Figure 5-5 also indicates the position of the

pressure jump due to a shock wave in order to compare the time at which light is emitted and the time at which pressure begins to increase. Time zero is set to the time when the first pressure transducer measures an increase of pressure inside the tube. The mean velocity of the pressure wave obtained from pressure propagation is 1945.5 m/s; this agrees with the theoretical value of 1932 m/s. The position at which the emission increases is exactly the same as that of the pressure jump due to the luminance induced by a strong incident shock wave. The fact that the luminance region behind the incident shock exists can be inferred from figure 5-7, which shows the flame propagation near the tube exit.

Therefore, it is very difficult to measure the flame speed from the emission data alone. However, the data clearly indicates that the flame exists inside the tube. The emission from the flame increases as the flame approaches the tube outlet. And it is detected until about 200 μsec after the flame exit the tube outlet at 83 μsec.

Figure 5-6 presents the comparison of emission signals with bursting pressures for a tube 300 mm long. In the Figure 5-6, the bursting pressure is 10.8 MPa and 23 MPa, respectively. Spontaneous ignition occurred for both conditions. The jump of the emission signal was observed at a position near the rupture disk when the burst pressure is higher. This result means that the flame is generated near the rupture disk when bursting pressure increases; this is because the multi-dimensional shock-shock interactions occur faster and the temperature of contact surface behind the incident shock increases more largely when bursting pressure is high. Because these factors make a mixing region faster and an induction time shorter, the reaction occurs faster near the rupture disk.

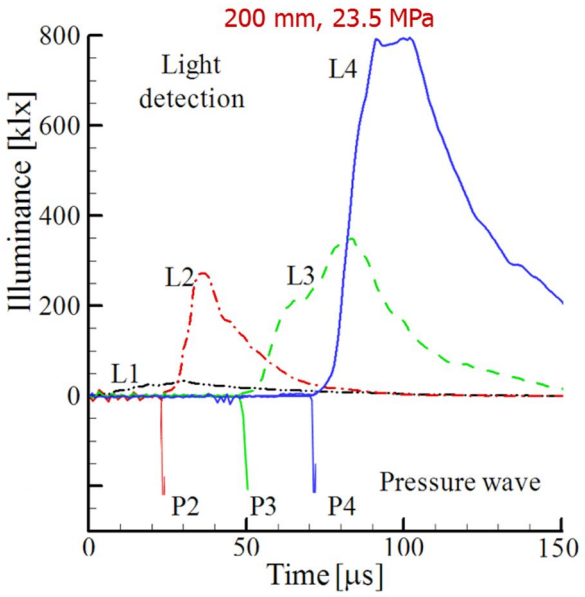

Figure 5-5 Luminance vs time inside the 200 mm extension tube at burst pressure of 23.5 MPa

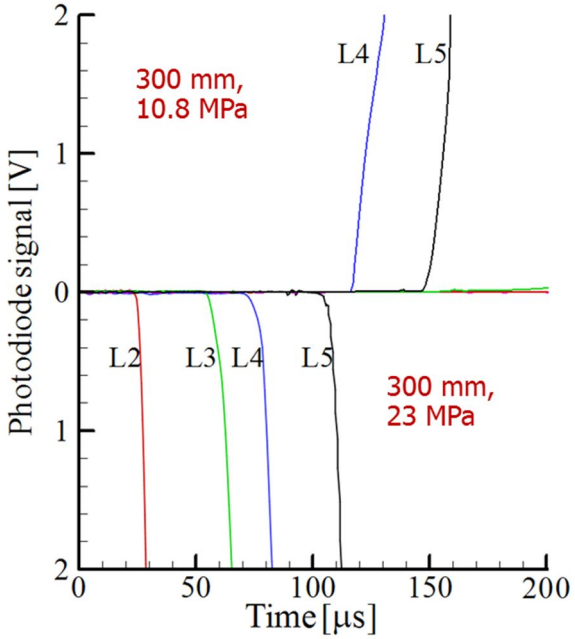

Figure 5-6 Signal from photodiodes inside the 300mm extension tube at burst pressure of 10.8 MPa (upper) and 23 MPa (lower)

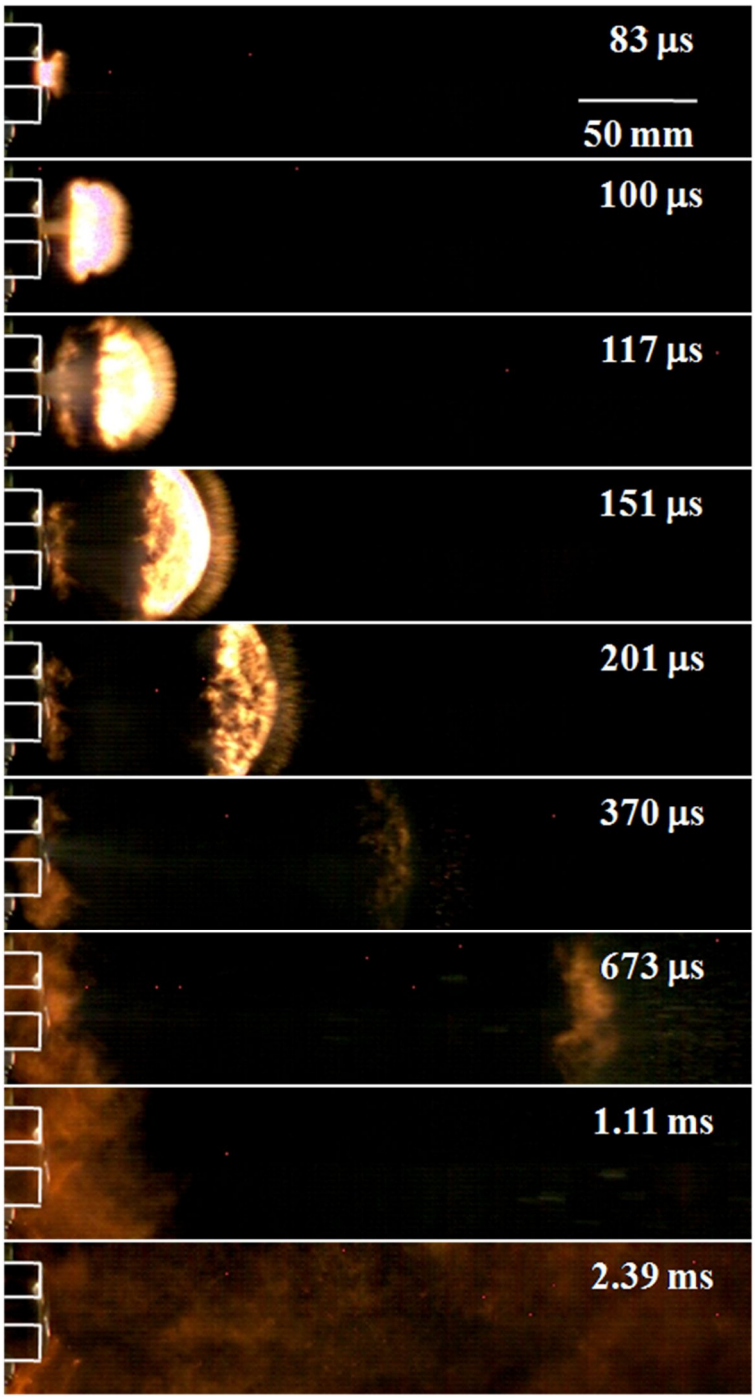

Figure 5-7 Flame propagation outside the 200 mm extension tube at the burst pressure of 23.5 MPa

5.2 Effect of Tube Diameter

5.2.1 Identifying ignition pattern at different tube diameter

According to the experiments, change in ignition patterns have been observed depending on the length of the extension tube for the same burst pressures. This difference is shown in figure 5-8. The results also show that the effect due to the extension tube is more critical than the effect of an obstacle near a tube. Furthermore, it has been observed that non-ignition, failed-ignition and self-ignition phenomena may occur depending on the inner diameter of the tube, even for the same burst pressures. Therefore, in this chapter, in order to investigate the reason of the different ignitions patterns depending on the inner diameter of the tube, numerical analysis results of a 200 mm length, 3 mm and 10.9 mm diameter tube is computed for diaphragm burst pressure ratio of about 110, and is compared to the experimental results.

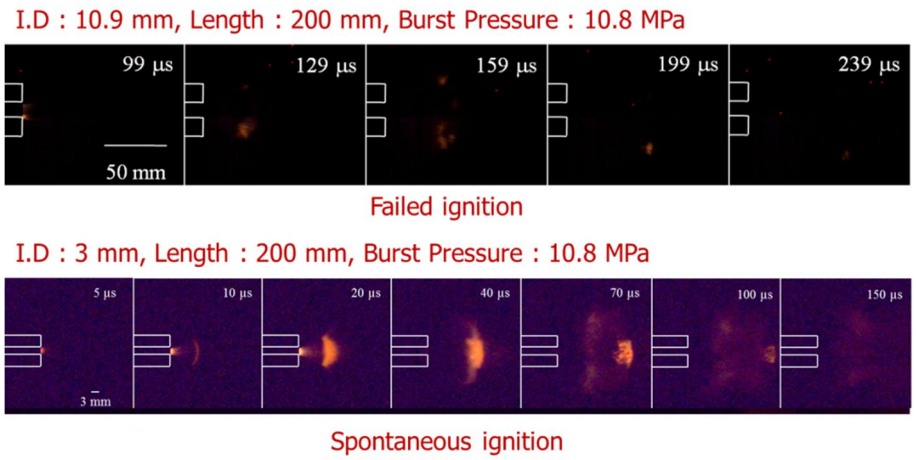

Figure 5-8 Different ignition patterns at the same burst pressure

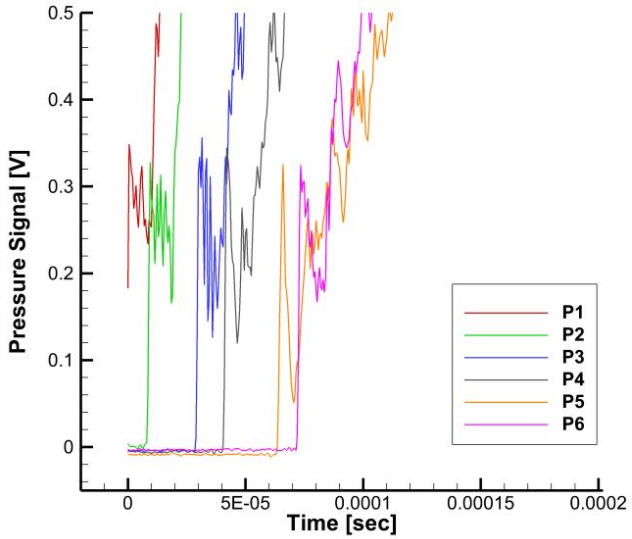

Figure 5-9 Shock wave propagation inside the extension tube

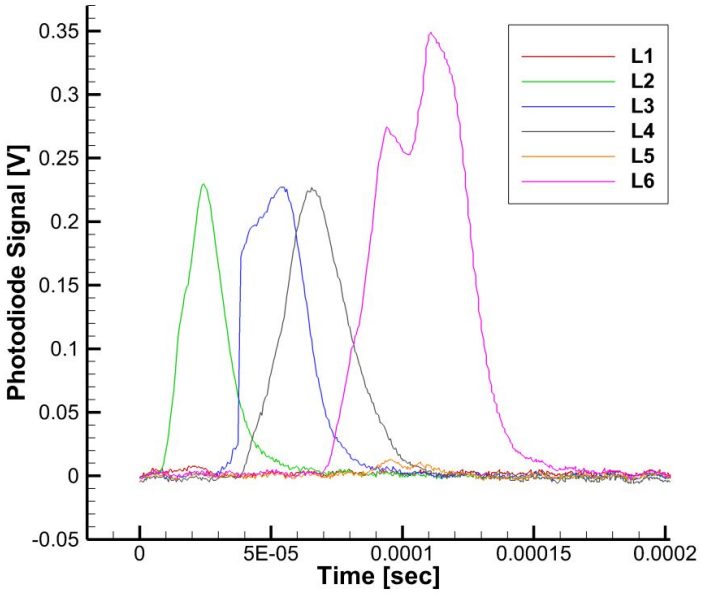

Figure 5-10 Luminance signal from the photodiode through the extension tube

Figure 5-9 and 5-10 shows the acquired signals from an experiment using the 3 mm inner diameter tube. As explained earlier, the first pressure transducer is used as the trigger source. The slight delay of the photodiode signals compared to the pressure rise is due to the flame existing near the contact surface. The acquired shock propagation speed and contact surface propagation speed shows a 3% / 5% difference compared to the theoretical propagation speeds. The theoretical and acquired shock and contact surface propagation speeds are shown in the table below. The reference for the shock wave is the rising signal of the pressure transducer, whereas the reference for the contact surface is the maximum point of each sensor signals.

Table 5-1 Comparison between theoretical and measured speed

	Theoretical Value	**Measured Value**	**Error (%)**
Shock speed (m/s)	1562.3	1610.9	3
Contact speed (m/s)	1237.7	1177.3	5

Referring to figure 5-9, a portion of the signals is lost due to the usage of P1 signal as the trigger source. However, considering the rising time of the sensor and the characteristics of a shock wave, such loss does not affect the results. Regarding the photodiode signals, two interesting point is observed. Firstly, the existence of a flame can be predicted from the L2 signal, however there is almost no signal in L1. Secondly, L5 shows barely any signal, while the signal is amplified for the two L6 signals. This can be simply understood as a result

of a weak flame, however as pointed out earlier, regarding the acquired signals, further possibilities must be considered. There are three possible explanations for such phenomena. Firstly, there is a possibility that shockwaves could have damaged the sensors, regarding the fact that weak signals were detected at the same locations throughout the experiments. Secondly, there could have been flaws in the particular tube sensor ports during the manufacturing process. Lastly, in case of the photodiode, superglue and epoxy are used for fixing the sensor onto the tube. However, there were cases where it was necessary to reattach the sensors onto the tube, as the sensors got loose due to continuous experiments. During such procedures, remains of fragments of the adhesives could have blocked the sensors, weakening the acquired signals. Considering these three issues, although it is impossible to exactly predict the flame strength, confirmation of flame existence at a particular location is possible.

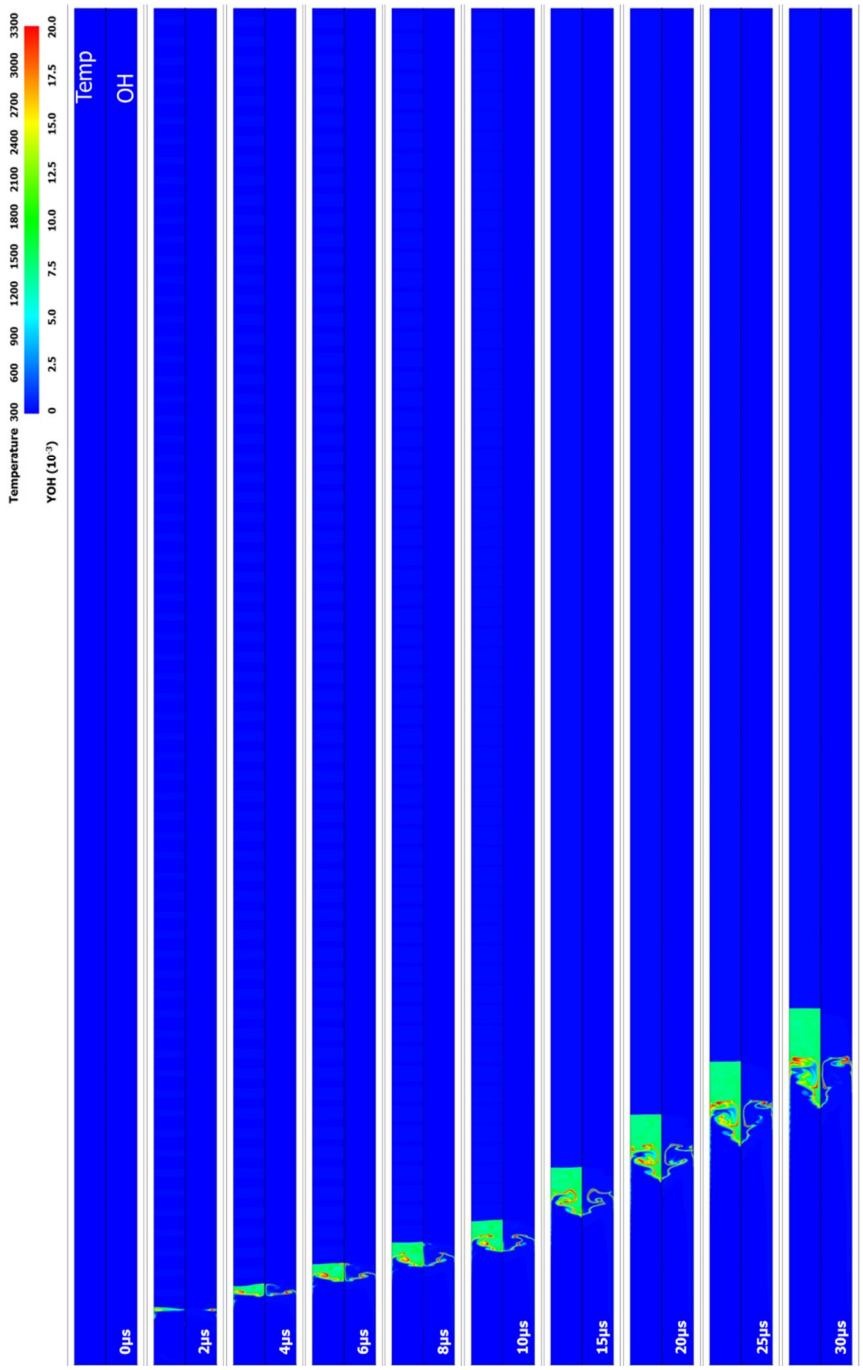

Figure 5-11 Early stage of flame development for a 3 mm diameter tube: Temperature vs OH mass fraction

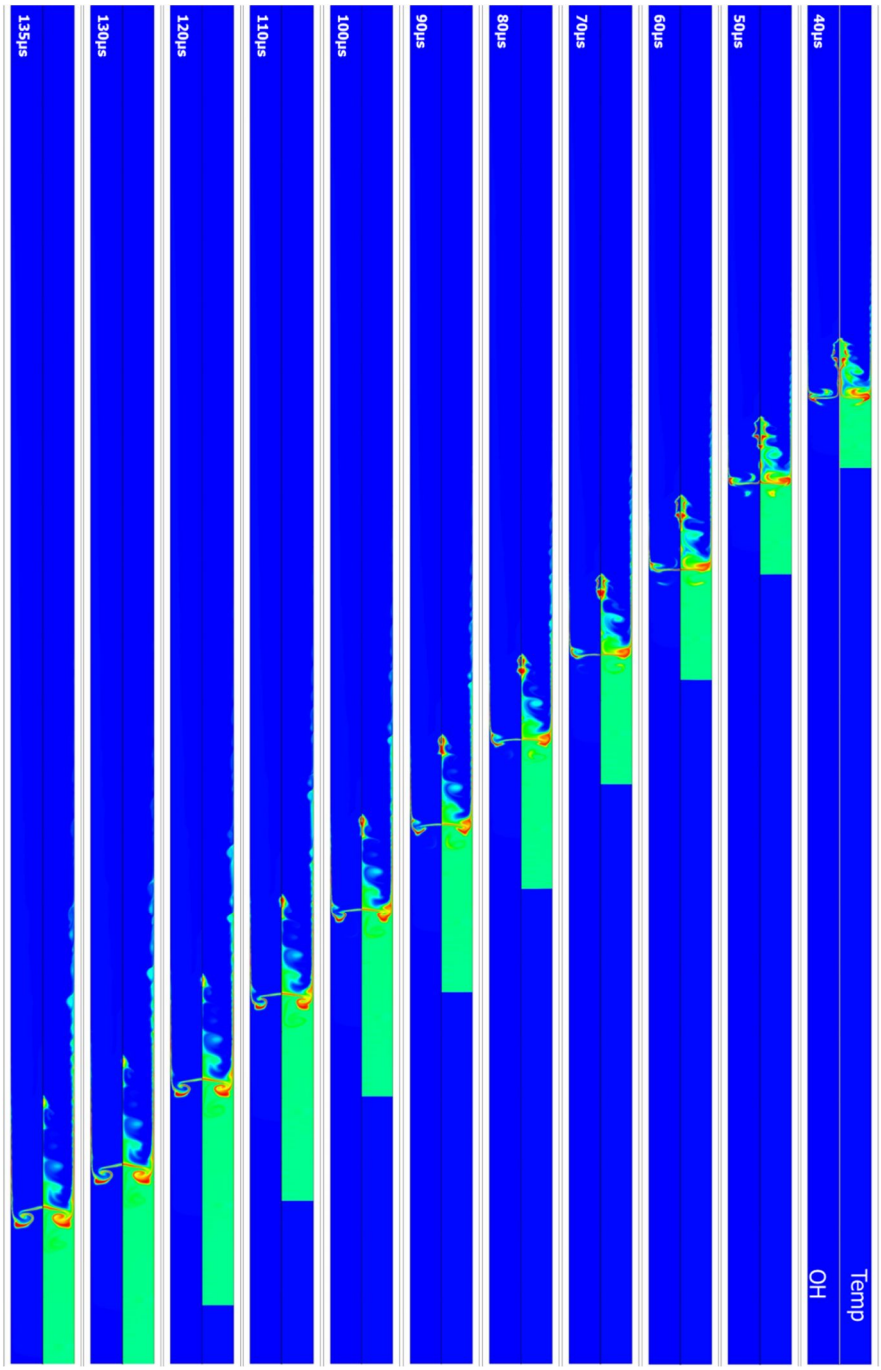

Figure 5-12 Later stage of flame development for a 3 mm diameter tube: Temperature vs OH mass fraction

Temperature and OH mass fraction according to time is shown in figure 5-11 and figure 5-12. Here, the partial spherical pressure boundary assumed with 3 mm inner diameter tube. The upper figure shows the temperature and the lower figure shows the OH mass fraction. According to the 1D analysis for the identical burst condition, auto-ignition due to diffusion and mixing of heated air and hydrogen at the contact surface occurred at about 14 μsec, shown in figure 5-13. But in the simulation with the partial pressure boundary, the reaction is occurred near the boundary layer at about 2 μsec. This can be seen to be due to the multi-dimensional shock interaction, which is resulted from the diaphragm structure as revealed in past studies. However when considering the detailed flow development, although the diaphragm is assumed to be partial spherical shape, for very thin Mylar, as that of the experiment, it is very similar to that of a full spherical boundary condition. Detailed study on the difference between these two configurations is presented in the next chapter. The flame formed at the boundary propagated along the contact surface, and jet due to shock focusing was not observed in this configuration.

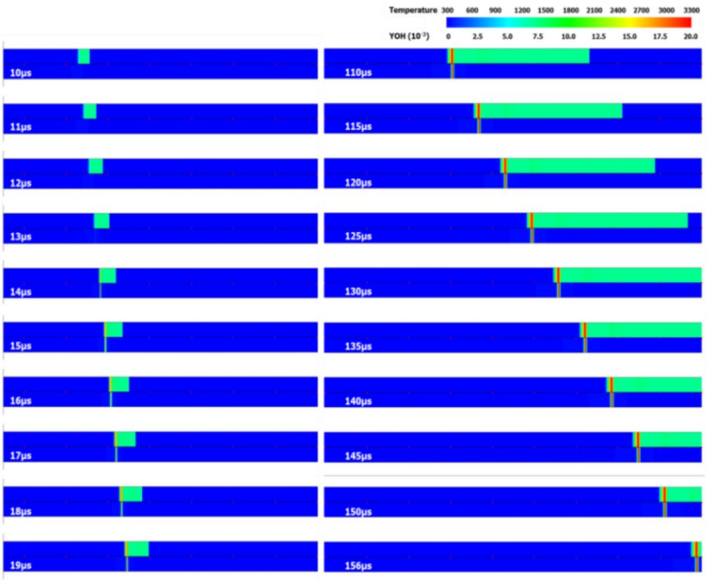

Figure 5-13 1D simulation to determine the ignition delay only by the diffusion between shock heated air and expanding hydrogen

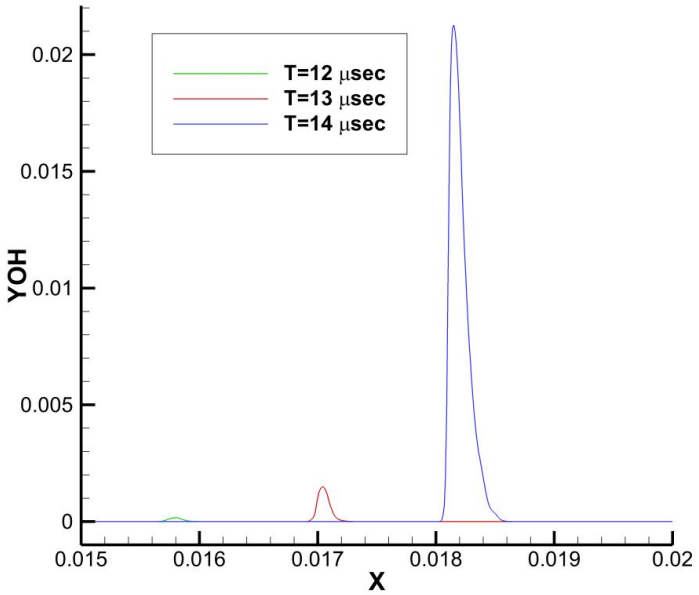

Figure 5-14 OH mass fraction at the beginning of reaction

Comparing the OH radical distribution at the sensor location of the photodiodes, the contact surface passes the L1 point at 40 μsec, where the existence of flame near the wall can be observed. Therefore, although the sensor did not exactly detect the illumination, the results agree with the small amount of signal detected at L1. Between 50 μsec ~ 60 μsec as the contact surface passes the L2 location, flame can be found in the result. And another finding is that the strength and size of the flame remains almost the same during it flows from the location L3 to L4, it agrees with that the signal from L2 to L3 shows same tendency. This may be resulted from the flat shaped flame region observed in the numerical simulation. However after 90 μsec the flame start to be developed from the boundary layer then the larger flame spouted out.

Figure 5-15 and 5-16 shows the numerical analysis result for the 10.9 mm inner diameter tube. The formation of the flame at the boundary layer after the diaphragm bursts, merging with the flame in the core region, and the formation of a complete flame is very similar as the 3 mm inner diameter tube. However, the time for the flame to be formed is relatively longer, and when the flame merges, it can be seen that the flame is stretched as it is divided into several smaller flames. Out of the smaller flames, vortex-like flames died out as the flame propagated along the tube, whereas only long thin flames exited the tube. As a result, unlike the 3 mm inner diameter tube, generation of a flat flame was not observed.

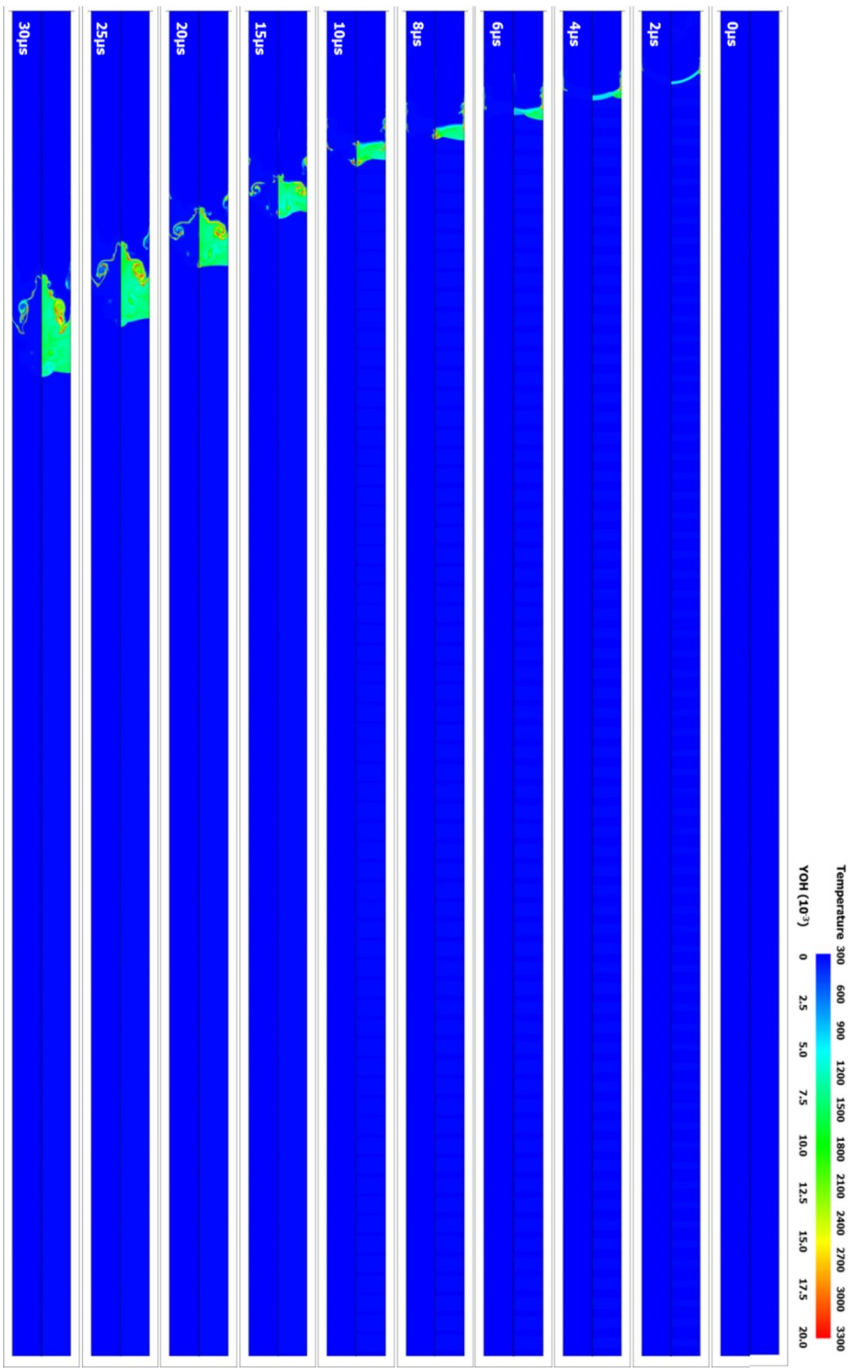

Figure 5-15 Early stage of flame development for a 10.9 mm diameter tube: Temperature vs OH mass fraction

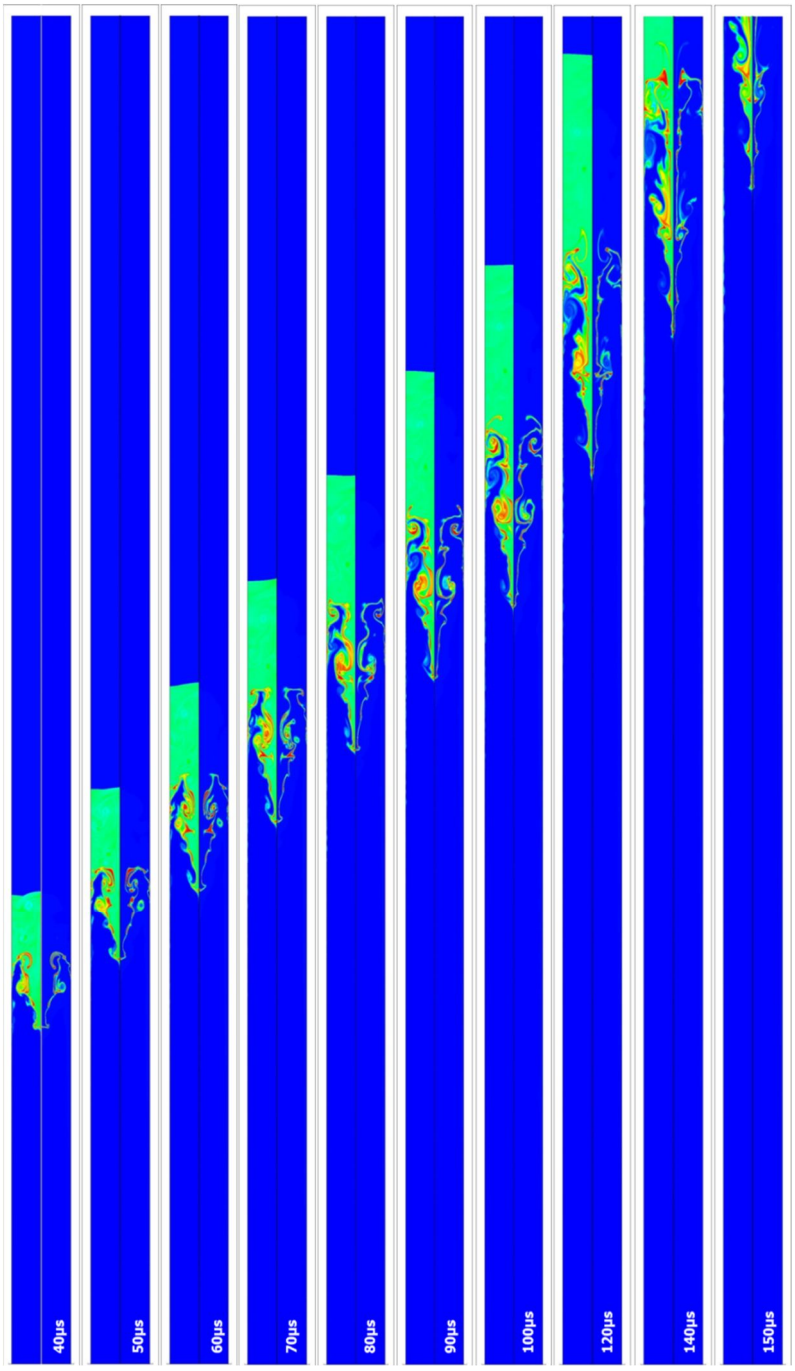

Figure 5-16 Later stage of flame development for a 10.9 mm diameter tube: Temperature vs OH mass fraction

In order to further investigate flame development characteristics, OH mass fraction and flame index is plotted in figure 5-17~5-20. The flame index introduced by Takeno et al.[54] was the method to distinguish the pre-mixed flame and diffusion flame by comparing the distribution of fuel and air. Although there are some modified versions, the original form of equation is used in this study.

$$FlameIndex = G_{FI} = \nabla Y_F \ \nabla Y_O$$
$$\begin{cases} G_{FI} < 0 & \text{Diffusion Flame} \\ G_{FI} > 0 & \text{Premixed Flame} \end{cases} \qquad (5\text{-}1)$$

After the diaphragm burst, several eddy formed from the instable flow and shock waves accelerates the mixing of heated air and hydrogen. As a result, a pre-mixed flame is dominated than a diffusion flame near the contact surface. However, the situation is reversed as the contact moves downstream. The eddy shaped flame is changed into a flat flame and diffusion effect becomes more dominated than before. On the other hand, a pre-mixed flame is also developed in the boundary layer by the continuously supplied heated air and its mixing with hydrogen. These two flame regions finally merge into a strong flame inside the tube. After 50 μsec, the mixing effect due to vortices is diminished and the flame propagates, maintaining its form. After 80 μsec, the flame, starting from the boundary layer, grows to a complete flame and is propagated outside of the tube. It seems that this flat shaped complete flame with a supply of an air through the boundary layer keep the flame sustaining when it leaves the tube.

However when the inner diameter of the tube increases, disturbances, due to the burst of a diaphragm, influence the flow for a longer time. Eddies

from the edge of the diaphragm and the interaction between shock wave and boundary layer make local pre-mixed flame inside the tube. Because this pre-mixed flame accelerates local propagating speed, the flame starts to stretch inside the tube as shown in figure 5-18. Unlike the case of 3 mm tube, the stretched flame is not transformed into a flat shaped flame before it leaves the tube and the thickness of the flame seems thinner both in the boundary layer and the core reaction regions. As the flame does not form a complete flame, it seems that the flame does not have enough energy to overcome rapid expansion when it spouts into the air.[55] Thus, the flame that has exited the tube is exposed to an easy condition to blow off due to sudden expansion, resulting failed-ignition. Therefore, although multi-dimensional shock heats up the air and auto-ignition of the air and hydrogen takes place, it does not always end up as a spontaneous ignition.

Comparing the flame shapes and the flame index, a development of the flame for a 10.9 mm tube at the end of the tube is similar to that for a 3 mm tube at the earlier stage, before the flat flame has been formed. From this observation, findings from the previous research which is a sufficient length of a tube is required to get a self-ignition are not just for a merging of the two flame in the boundary and core regions. It seems that the tube length is also important to have a complete diffusion flame which is formed after the unstable flow from the burst is weakened.

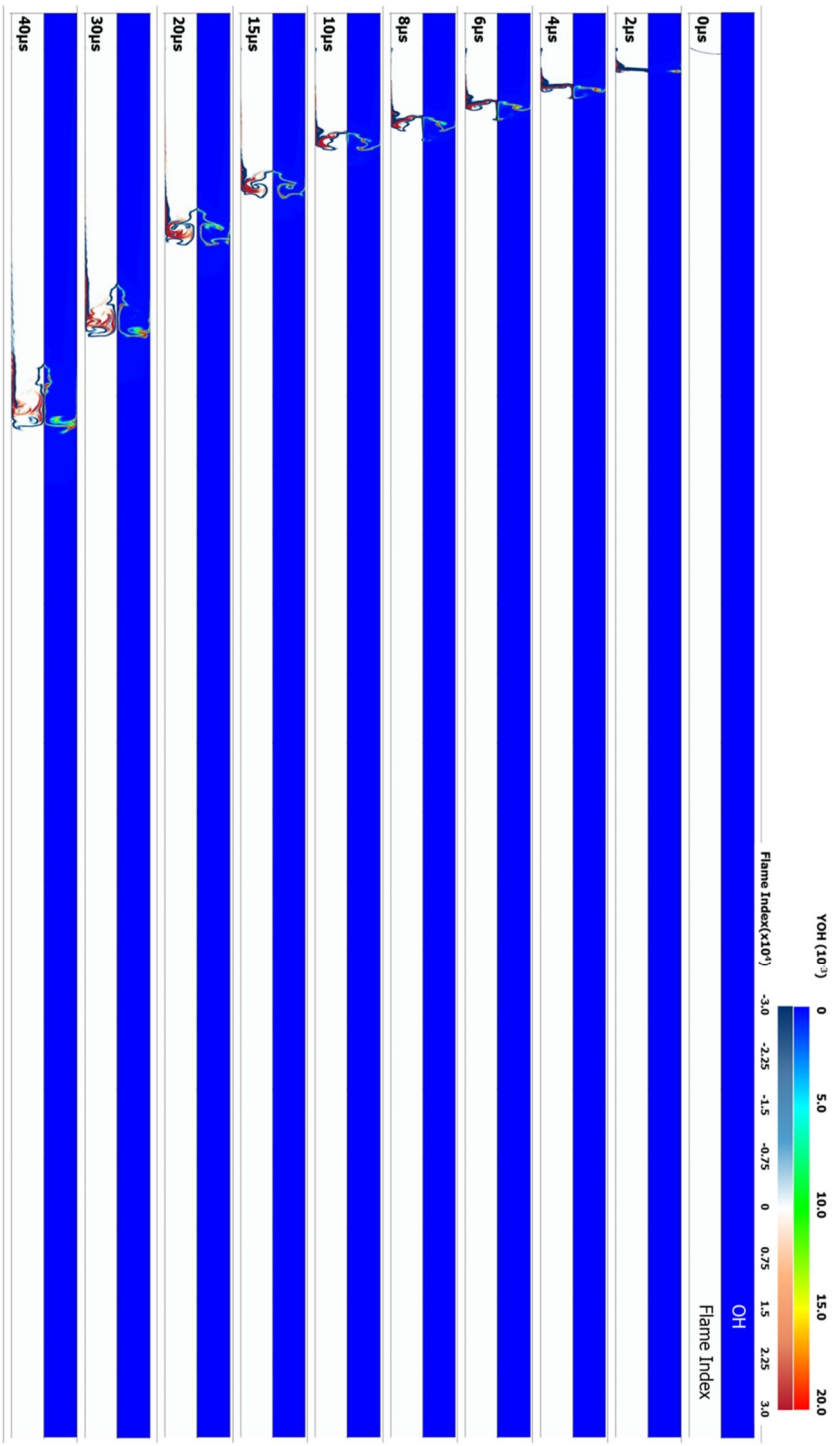

Figure 5-17 Flame index and OH mass fraction in the 3 mm tube ; 0~40 μs

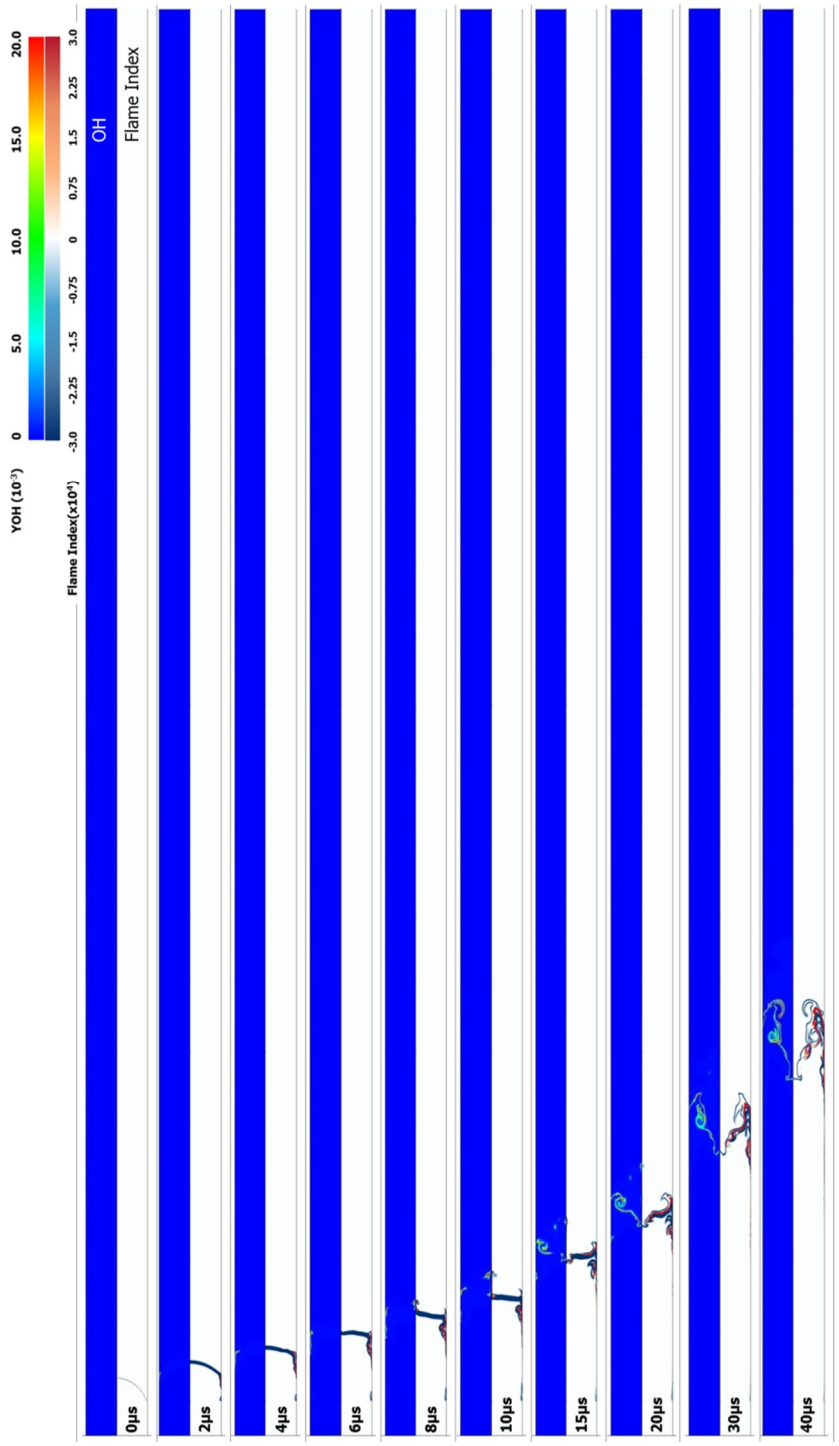

Figure 5-18 Flame index and OH mass fraction in the 10.9 mm tube ; 0~40 μs

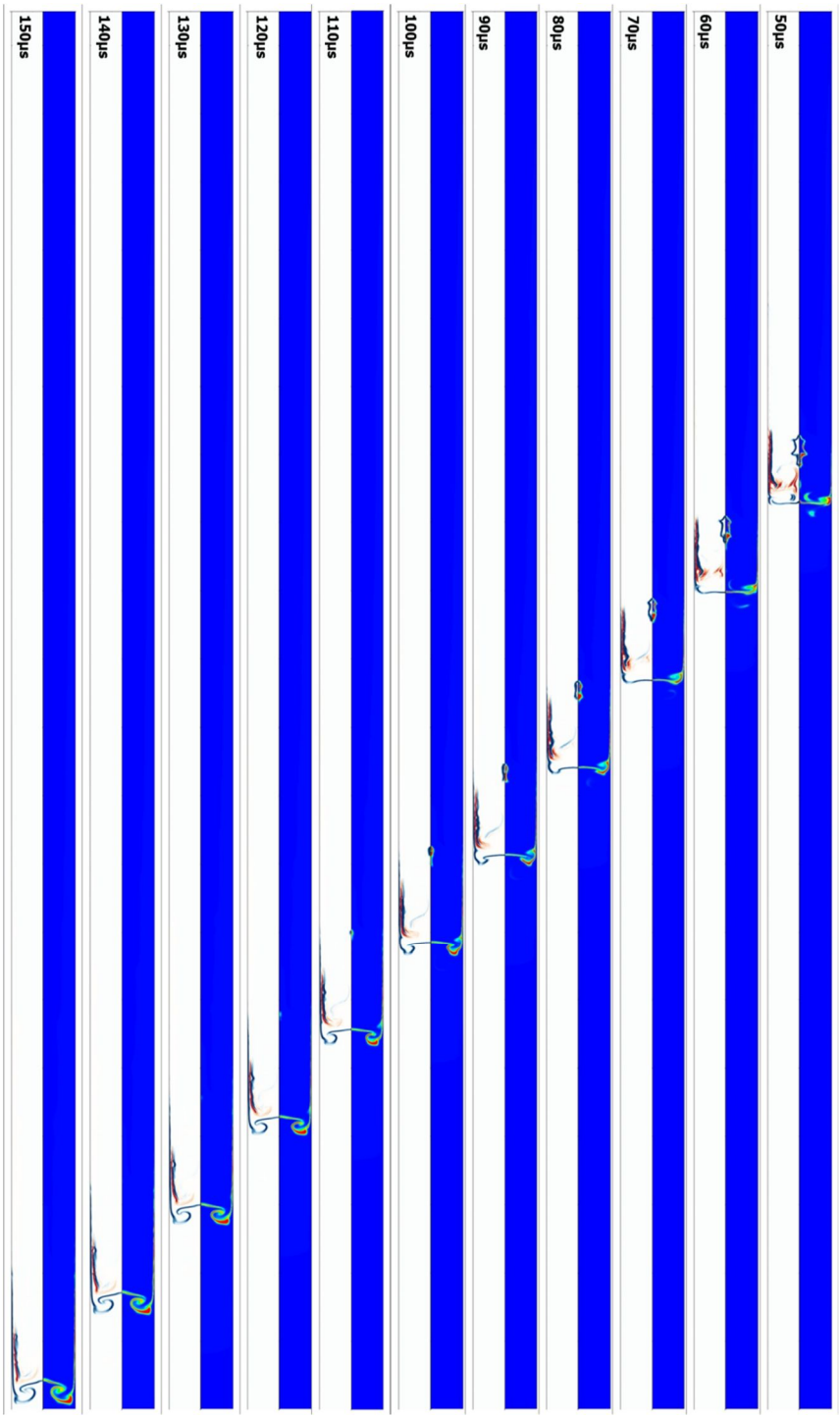

Figure 5-19 Flame index and OH mass fraction in the 3 mm tube ; 50~150 μs

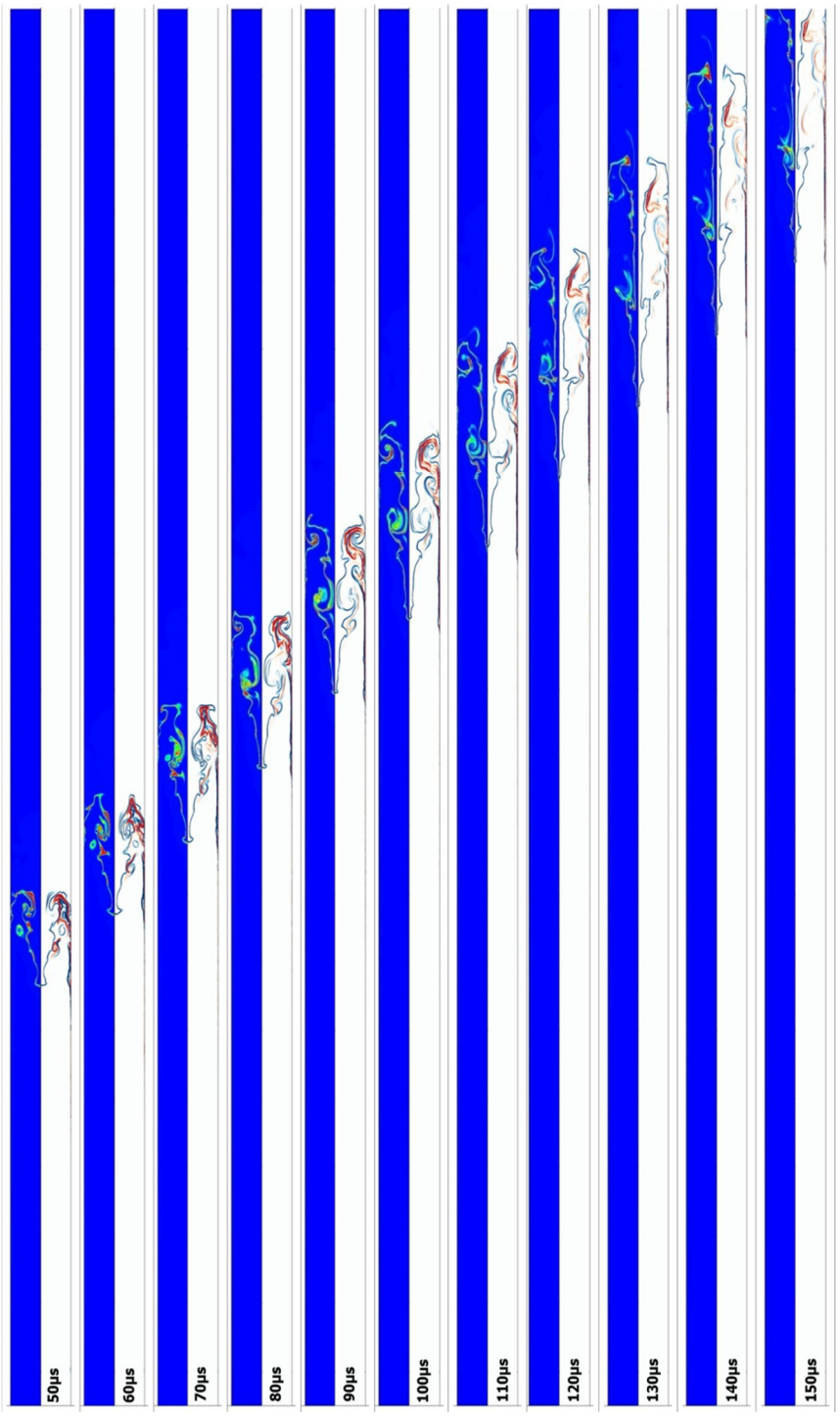

Figure 5-20 Flame index and OH mass fraction in the 10.9 mm tube ; 50~150 μs

5.3 Effect of Rupture Diaphragm Shape

From the previous results, it seems that the ignition mechanism is quite clear, and that three factors are regarded as essential to initiate the ignition inside the tube and to sustain the flame outside the tube; 1) a high burst pressure in which a strong shock can be generated, which leads to sufficient heating of the air; 2) the shape of the rupture disk, which can allow multi-dimensional shock interactions to be induced, leading to the formation of mixing regions; and 3) a sufficient tube length through which the flame can be spread, which can generate sufficient energy. However, this postulation was deduced from results for limited conditions with respect to burst pressure and shape of the rupture disk. Most of these experimental and numerical results were obtained with burst pressure of about 10 MPa and less than 20 MPa. Furthermore, the effect of the shape of the rupture disk on the ignition, which affects the feature of shock interactions, has not been considered in detail. These are factors closely related to the rupture disk, which can affect the ignition mechanism or process. There is a strong possibility that the feature of shock interactions and mixing can be differ significantly, and the mechanism can also differ if the burst pressure is higher than 20 MPa and the shape of the rupture disk is different. In fact, although the experiment has been conducted with rectangular cross-sectional test model, the ignition feature observed in the result of Kim et al. [52] is quite different from the mechanism above. According to the visualization results from them, the two reaction regions did not merge and the reaction region generated from the boundary layer developed gradually.

In this chapter, the effect is analyzed of the rupture disk and higher pressure above 20 MPa on the spontaneous ignition mechanism inside the tube. To do this, numerical simulations have been conducted for various rupture conditions, for which the burst pressure is maximum at 40 MPa.

As pointed out earlier, burst pressure of previous experiments were mostly lower than 20 MPa, and thus in this simulation, pressure lower than 20 MPa is defined to be low burst pressure and pressure higher than 20 MPa is defined to be high burst pressure.

5.3.1 Low burst pressure

Spherical boundary condition

Figure 5-21 and 5-22 shows results of a numerical simulation for the partial spherical boundary at the burst pressure of 10 MPa. The images show the ignition process in detail, and the mechanism is very similar to that in previous results [32]. Generally, it is known that the initial flow induced by multi-dimensional shock interactions after failure of the disk significantly affect the overall flow development and ignition mechanism in the downstream tube. The initial transient flow can be explained from the numerical Schlieren images and pressure contours for every 2 μsec in figure 5-21(a). The moment of the disk failure is set to be 0. The OH radicals in the dashed-rectangular region are inserted together to show the reaction process in figure 5-21(a). The spherical leading shock wave is formed by the spherical shape of the pressure boundary, which impacts the side wall of the downstream tube and is reflected back. Subsequently, the shock focusing is observed at the axis of symmetry, which causes a strong jet and flow instability at 6 μsec after pressure boundary is destroyed. The jet is strong

enough to intrude the preceding shock along the axis of symmetry, and starts to form a vortex ring at the center of the tube, as shown in the images of 10 μsec. The role of this vortex ring is important in mixing between cold hydrogen and heated air, as shown in the equivalence ratio images of 10 μsec in figure 5-21(b).

The contours of the mass fraction of OH radicals, Y_{OH}, and temperature are presented with the contour of Mach number and density for every 10 μsec in figures 5-22, to show the process of the hydrogen reaction due to auto ignition and the flow structures in the downstream tube together. From the results, we can see there are two separate reaction regions, a boundary layer and core region, at the initial stage. The reaction region within the boundary layer is due to the volume of mixture formed within the heated boundary layer as the contact surface of expanding hydrogen and ambient air interacts with the developing boundary layer. The reaction in this region grows into a hot shocked region along the junction of the boundary layer and the contact surface. A reaction in the core region is also observed along the mixing region by a generated vortex ring. A region of reaction by spontaneous ignition of hydrogen is observed as a low-density area, which corresponds to the high-temperature area and the locally distributed area of OH radicals in figures 5-22. These two ignition regions grow and eventually meet each other, forming a complete section of flame at 40 μsec. After that, this complete flame over the cross section is sustained and propagates along the downstream tube.

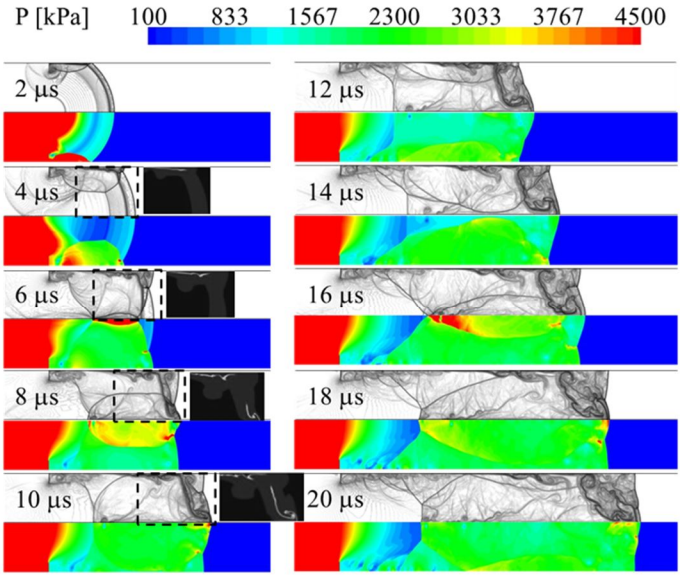

(a) Numerical Schlieren and pressure contour

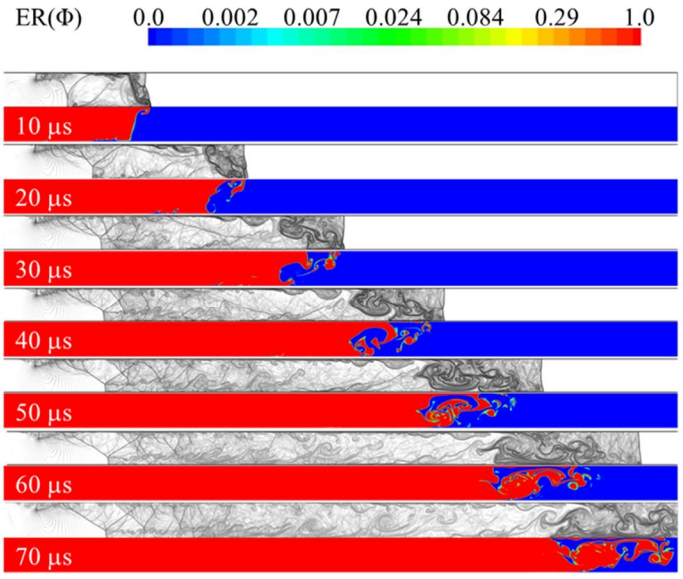

(b) Numerical Schlieren equivalence ratio

Figure 5-21 Result for a partial spherical pressure boundary: burst pressure 10 MPa
(a) Schlieren & Pressure, (b) Schlieren & Equivalence ratio

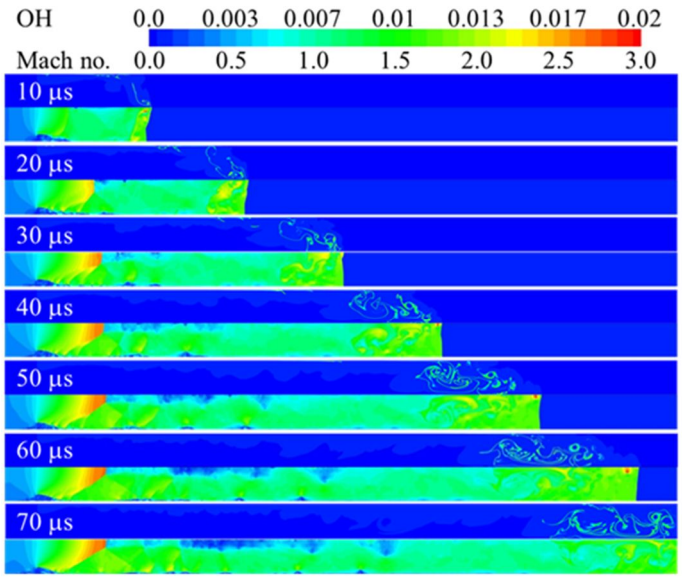

(a) OH mass fraction and Mach number contour

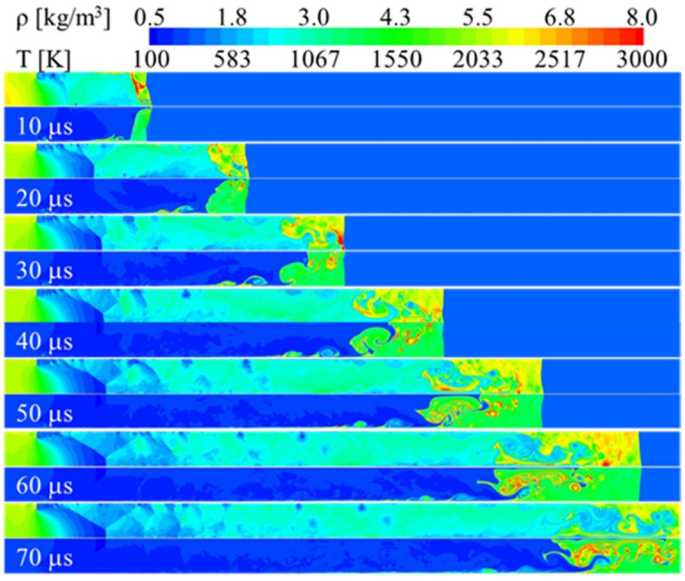

(b) Density and temperature contour

Figure 5-22 Result for a partial spherical pressure boundary: burst pressure 10 MPa
(a) OH mass fraction & Mach number, (b) Density & Temperature

With a very similar method, the numerical results for a full spherical pressure boundary at the same burst pressure are presented in the figure 5-23 and 5-24. For the case that a full spherical pressure boundary is applied, the whole process in which a flow is developed and reaction regions are formed is very similar to that with a partial spherical pressure boundary. However, the flow is developed somewhat differently in the initial stages after the burst of the disk, because the reflective pattern of shock waves inside the tube is different, as there is no disk remains after burst. As shown in figure 5-23(a), the flow formation is similar with the case of partial spherical boundary condition until 8 μsec after burst, but after that, the vortex ring of the core region which does not have enough strength to penetrate a contact surface that is observed from a former condition In the images of 10 μsec in figure 5-23(a), it is shown that the hydrogen does not intrude into the core region of the tube, and the mixing region cannot be strongly formed. For this reason, there is no hydrogen in the contact surface of the core region after 10 μsec, as shown in figure 5-23(b).

Next, a remarkable distinction for the flow formation is shown in the contours of Mach number. As shown in figure 5-24(a), there exist very fast flow regions in the core of the tube compared to figure 5-22(a). Thus, the reaction of the core region moves away from the reaction region of the boundary layer, and two reaction regions are not merged after very weak mixing. Also, a reaction region is formed in the core region due to the small vortex ring as shown in figure 5-23(b). It seems that this fast flow region makes the mixing of hydrogen and air to be difficult much more downstream.

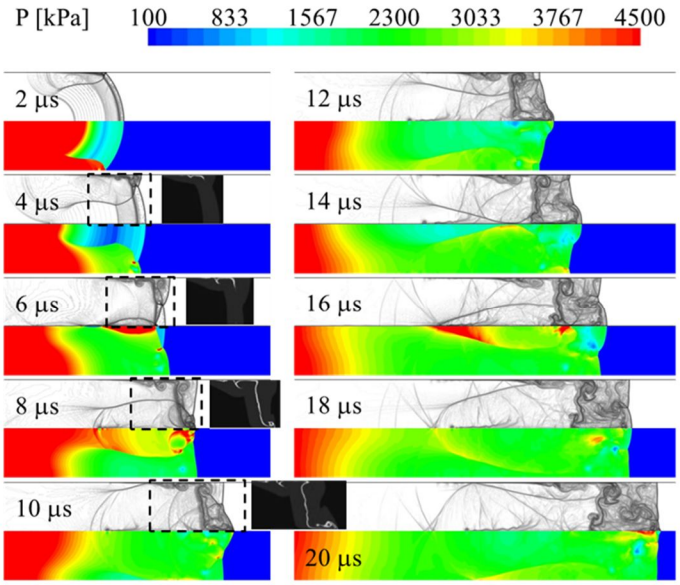

(a) Numerical Schlieren and pressure contour

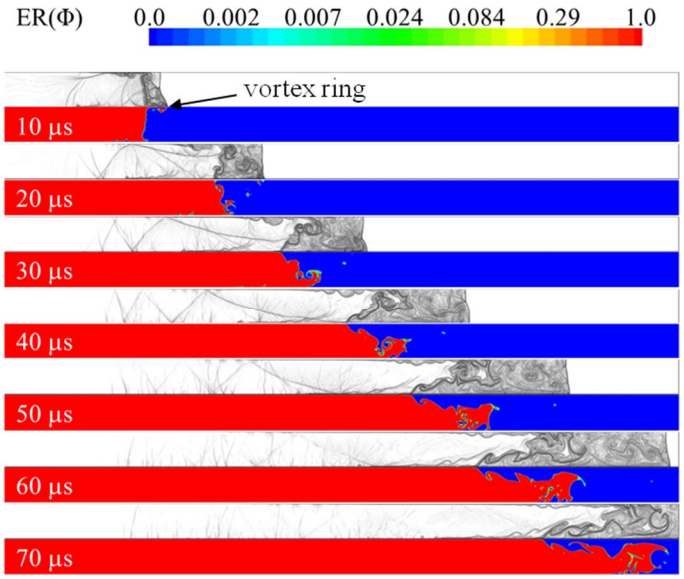

(b) Numerical Schlieren equivalence ratio

Figure 5-23 Result for a full spherical pressure boundary: burst pressure 10 MPa
(a) Schlieren & Pressure, (b) Schlieren & Equivalence ratio

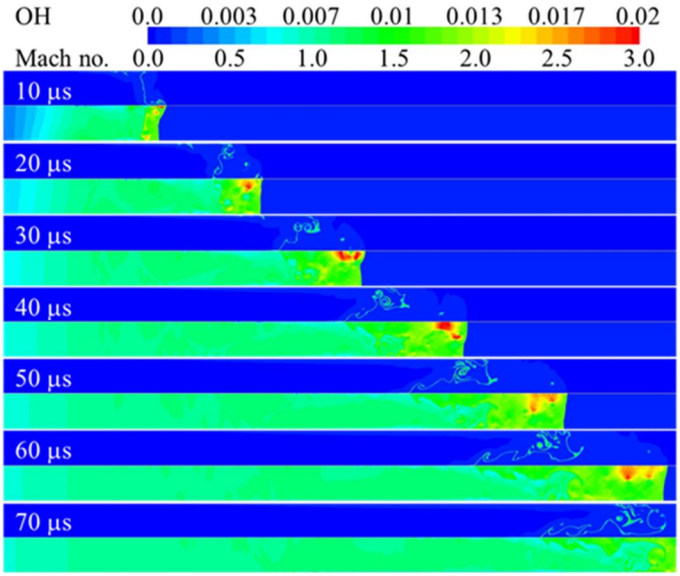

(a) OH mass fraction and Mach number contour

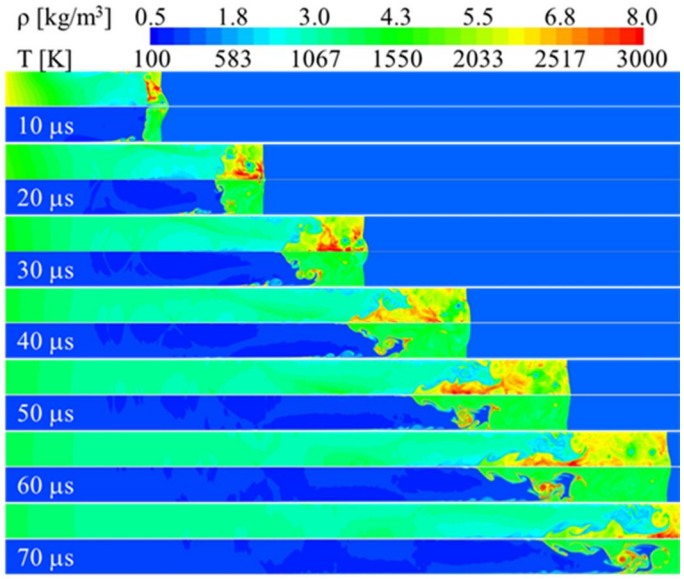

(b) Density and temperature contour

Figure 5-24 Result for a full spherical pressure boundary: burst pressure 10 MPa
(a) OH mass fraction & Mach number, (b) Density & Temperature

The mixing region near the boundary layer spreads gradually to the core region of the tube, and the reaction is also developed along the same region, as shown in figures 5-24. Consequently, when the full spherical boundary is applied, the ignition pattern differs; there is no merging of two reaction regions inside the tube, and the reaction region generated from the boundary layer initiates the self-ignition. Therefore, compared to partial spherical pressure boundary, the distance that the complete flame is formed inside the tube is longer. This ignition feature, in which a complete flame is formed from the reaction region developed from the boundary layer, is very similar with the experimental research from Kim et al. [52], which uses Mylar film as a rupture disk.

Flat boundary condition

Figure 5-25 and 5-26 shows the simulation results for the partial flat pressure boundary at a burst pressure of 10 MPa. The results show that multi-dimensional shock interactions accompanying the reflection of transverse waves do not take place when a flat pressure boundary is applied. Only some disturbance near the thin plate on the tube wall and reflected waves from the region are observed until 10 μsec after the failure of the disk. This reflected wave makes a jet, which is similar to the one induced from shock interactions, in the core region at 12 μsec in figure 5-25(a). However, a mixing region is not formed, as this jet cannot intrude into the contact surface between hydrogen and air. Eventually, no mixing or reaction region is found in the core region. However, a weak mixing region near the boundary layer is continuously developed, because there is a spot at which a kind of instability can be induced, as shown in figure 5-25(b). Therefore, it is very slow, but a

reaction region can be developed gradually along this mixing region, as shown in figures 5-26. Compared to the results of a full spherical pressure boundary, two cases have a similar tendency in that a mixing and reaction region is developed mainly from the boundary layer, but the area in which the reaction can be developed are quite different. More active mixing is formed, and the reaction is developed in a wider region when the full spherical pressure boundary is applied, because the flow formed inside the tube is generally governed by the strong instability induced by multi-dimensional shock interactions.

This tendency is understood more clearly when comparing the results for a full flat pressure boundary, figure 5-27. Only mass fractions of OH radicals and temperature contours are presented, because large variation does not occur inside the tube. Weak OH radicals can be observed in the contact surface as a consequence of molecular diffusion process of hydrogen into the heated air, because the air behind a strong incident shock is already heated enough for hydrogen to react. However, no additional mixing or reaction regions are observed, except near the boundary layer. This is because no hydrodynamic instability can be induced from the flat boundary, and there is no disturbance in the tube.

From the above results, one can observe different ignition patterns for different shapes of the disk failure. This is because the flow formation and mixing phenomenon can vary sensitively with the shape of the pressure boundary, which simulates the rupture disk and ignition pattern, two strongly influential factors. Multi-dimensional shock interactions and the shape of the disk, which can generate disturbances, play an important role in enhancing the mixing and reaction.

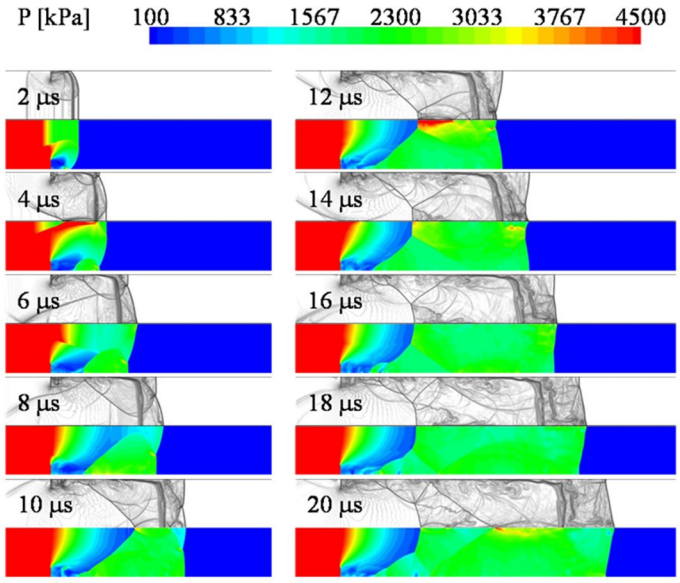

(a) Numerical Schlieren and pressure contour

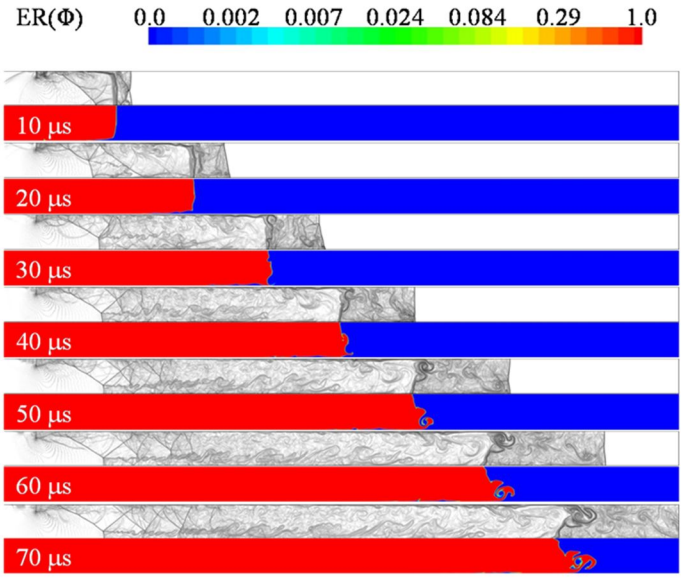

(b) Numerical Schlieren equivalence ratio

Figure 5-25 Result for a partial flat pressure boundary: burst pressure 10 MPa
(a) Schlieren & Pressure, (b) Schlieren & Equivalence ratio

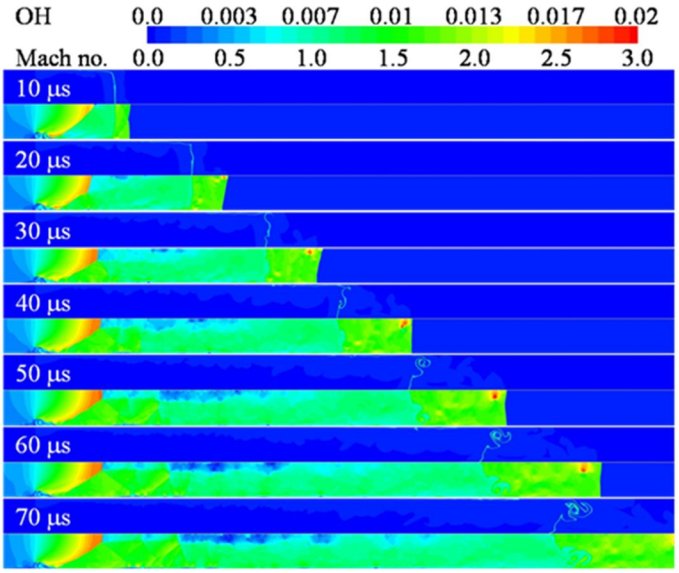

(a) OH mass fraction and Mach number contour

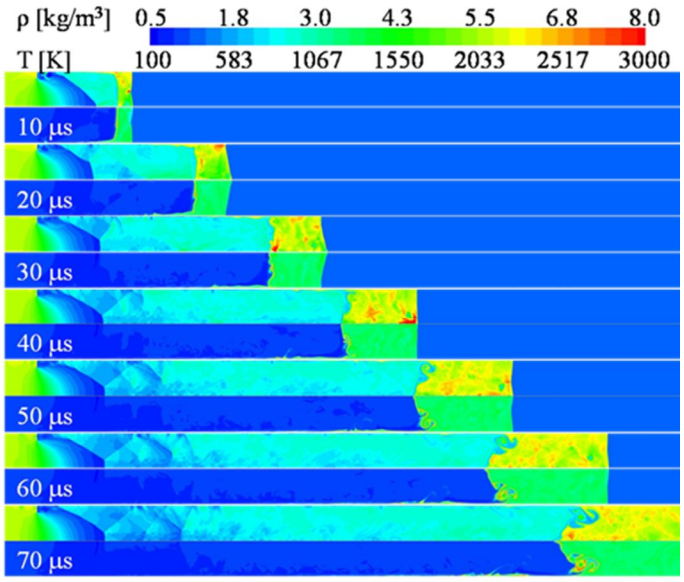

(b) Density and temperature contour

Figure 5-26 Result for a partial flat pressure boundary: burst pressure 10 MPa
(a) OH mass fraction & Mach number, (b) Density & Temperature

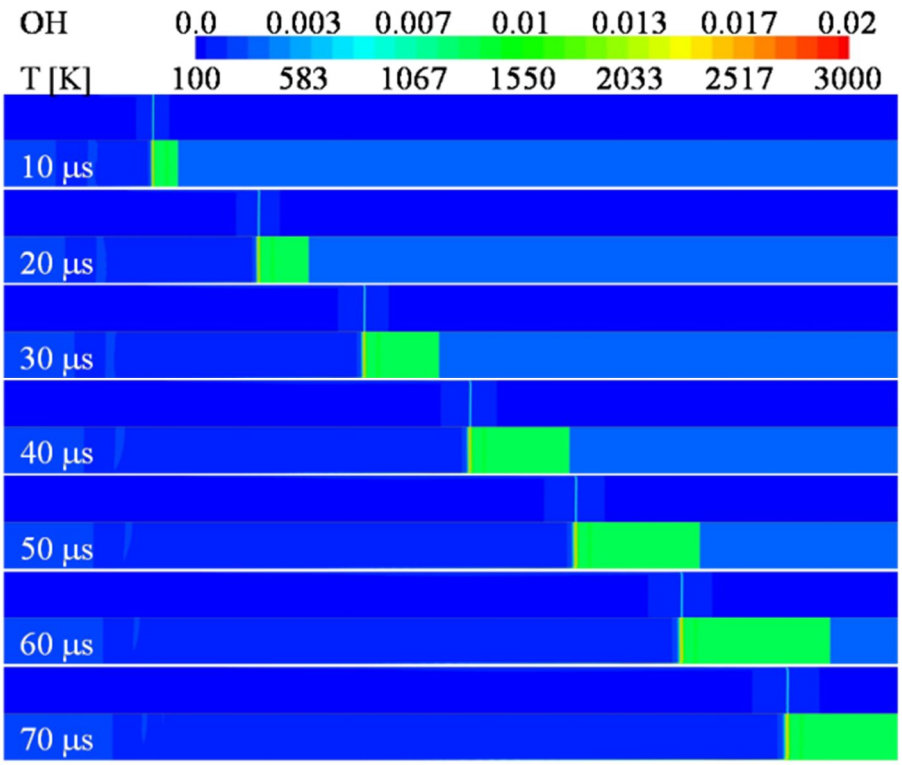

Figure 5-27 Result for a full flat pressure boundary: burst pressure 10 MPa

Multi-dimensional shock interactions can create mixing regions such as a vortex ring in the core region, and also assist in mixing near the boundary layer. It is clear that spontaneous ignition can occur more easily with a spherical pressure boundary, which can be applied in a real system.

However, the existence of the reaction in the core region or its merging with the reaction region near the boundary layer is not essential to initiating spontaneous ignition.

5.3.2 High burst pressure

Spherical pressure boundary

Figure 5-28~5-30 shows the results with the shape of pressure boundaries at the burst pressure of 23.5 MPa. Numerical Schlieren images, the equivalence ratio, the mass fraction of OH radicals, and the Mach number distributions are presented to compare the mixing and ignition phenomenon for all results. For a full spherical and a partial flat pressure boundary, the trend that the mixing and reaction occur is very similar to the former result, although the burst pressure increases. For a full spherical pressure boundary, as shown in figure 5-29, very small mixing and weak reaction occur in the core region, but they disappear rapidly as the flow is propagated downstream. Similar to the results of a full spherical pressure boundary at a 10 MPa burst pressure, two reaction regions fail to merge, and only the reaction region near the boundary layer is developed widely, because the multi-dimensional shock interactions are stronger than with a burst pressure of 10 MPa.

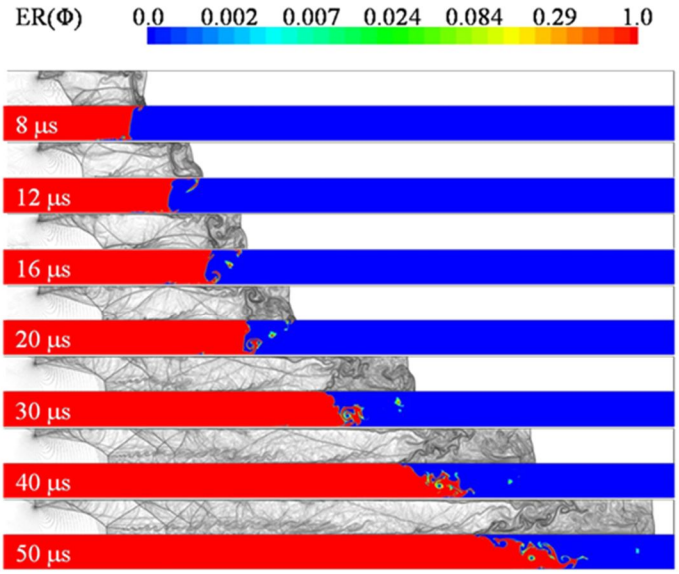

(a) Numerical Schlieren equivalence ratio

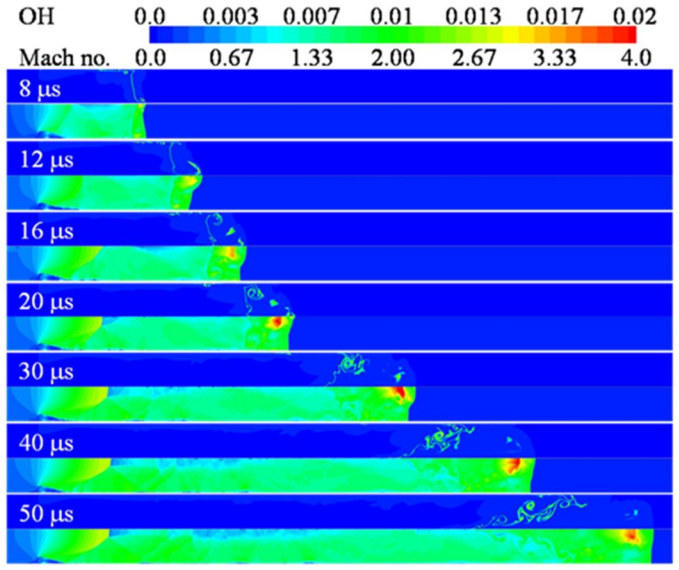

(b) OH mass fraction and Mach number contour

Figure 5-28 Result for a partial spherical pressure boundary: burst pressure 23.5 MPa

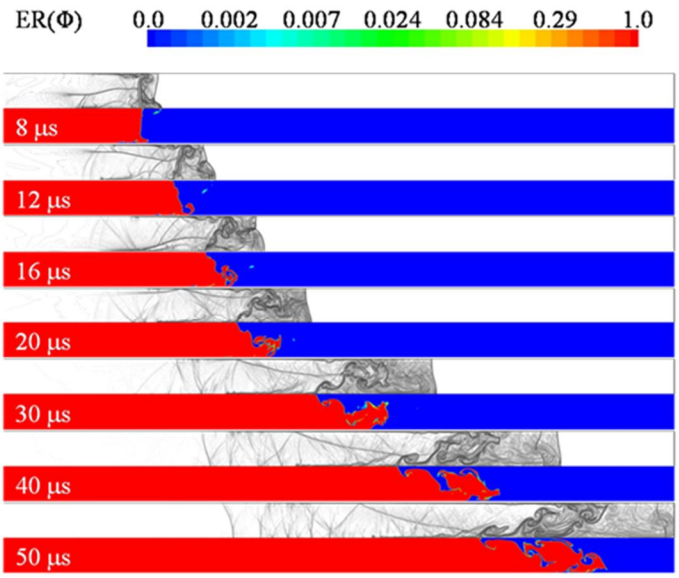

(a) Numerical Schlieren equivalence ratio

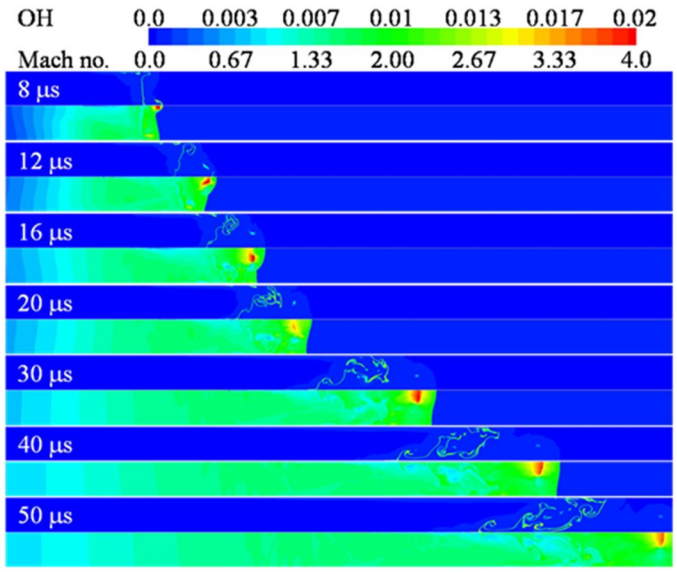

(b) OH mass fraction and Mach number contour

Figure 5-29 Result for a full spherical pressure boundary: burst pressure 23.5 MPa

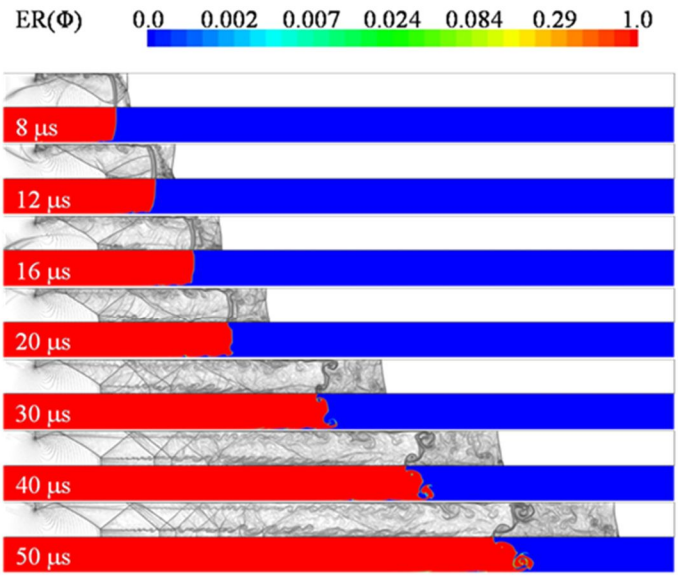

(a) Numerical Schlieren equivalence ratio

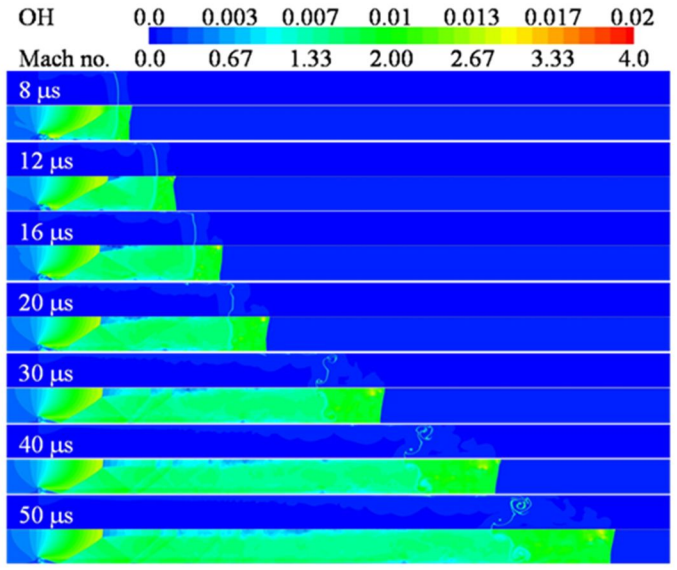

(b) OH mass fraction and Mach number contour

Figure 5-30 Result for a partial flat pressure boundary: burst pressure 23.5 MPa

However, compared to the results for the 10 MPa burst pressure, different ignition features are observed when a partial spherical pressure boundary is applied at the burst pressure of 23.5 MPa. The flow is formed very similarly until 12 μsec after the failure of the disk. A large vortex ring is generated from the multi-dimensional shock interactions, and a strong reaction is also observed in the core region. Simultaneously, the reaction region near the boundary layer is also well developed. But, after that, the two reaction regions are not merged together, and two regions part from each other gradually as the flow near the vortex ring is propagated downstream very quickly, as shown in the Mach number contours of figure 5-28. As the flow is propagated downstream, the reaction in the core region disappears, and only the reaction region generated from the boundary layer is developed widely. Consequently, when the burst pressure increases, the ignition pattern becomes similar for both a partial and a full spherical pressure boundary, as shown in figures 5-28 and 5-29, as the reaction in the core region does not play a key role in initiating spontaneous ignition any more.

Figure 5-31 and 5-32 shows the results with higher burst pressures for the partial spherical pressure boundary. The figure 5-31 is for a burst pressure of 30 MPa, and the figure 5-32 is for a burst pressure of 40 MPa. The general flow and reacting feature is similar with that of a burst pressure of 23.5 MPa. The phenomena such as flow formation occur somewhat more quickly when the burst pressure is higher, but both results are very similar, as shown in figures 5-31 and 5-32. Similarly, the speed that a flame is generated and propagated becomes faster as the burst pressure increases. For both cases, a large vortex ring and a strong reaction are observed in the core region at the initial stages after the burst of the disk, but they disappear soon after. Instead,

the reaction region developed from the boundary layer grows gradually and becomes a complete flame, filling the cross section of the tube. Consequently, the results show that the reaction of the core region is not important for initiating the ignition although it can be generated by the multi-dimensional shock interactions because of the spherical pressure boundary, when the burst pressure is above 20 MPa. Instead, the reaction region developed from the boundary layer plays a main role for spontaneous ignition inside the tube. Therefore, some distance within the tube is necessary to initiate the spontaneous ignition even though the burst pressure is sufficiently high, because the ignition mechanism depends on the reaction region developed from the boundary layer which has a slow propagating speed.

Flat Shape Pressure Boundary

For the partial flat pressure boundary at higher burst pressure, unlike the spherical pressure boundary condition, even when the burst pressure increases, the flow formation is very similar to that with 10 MPa burst pressure. In other words, there is no reaction in the core region, and only the reaction region near the boundary layer is developed gradually as the flow is propagated downstream. Therefore, in order for the hydrogen/air mixture to fully develop into flame, the tube must be long enough, and the flame hazard will decrease compared to spherical pressure boundary condition.

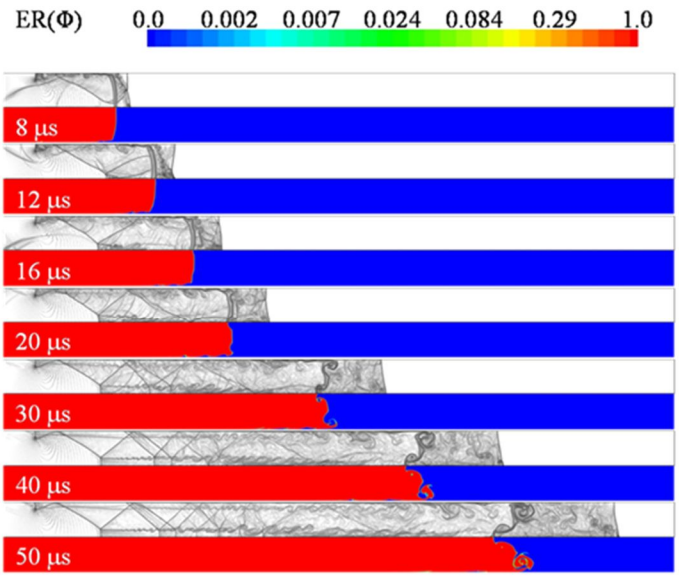

(a) Numerical Schlieren equivalence ratio

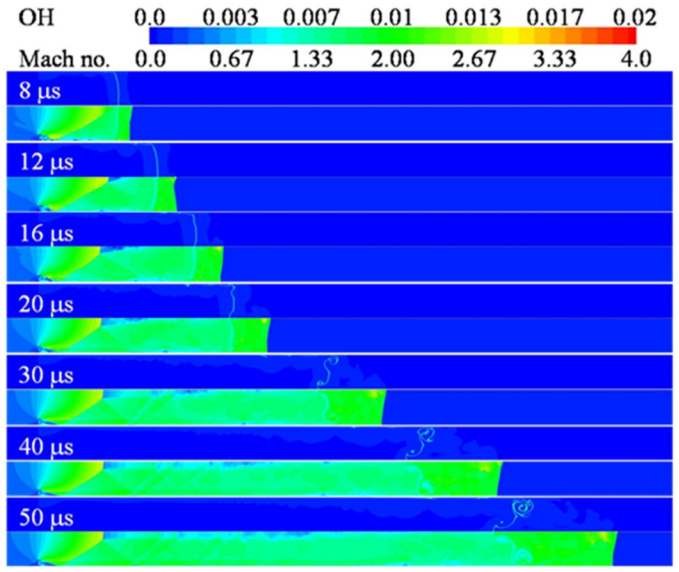

(b) OH mass fraction and Mach number contour

Figure 5-31 Result for a partial spherical pressure boundary: burst pressure 30 MPa

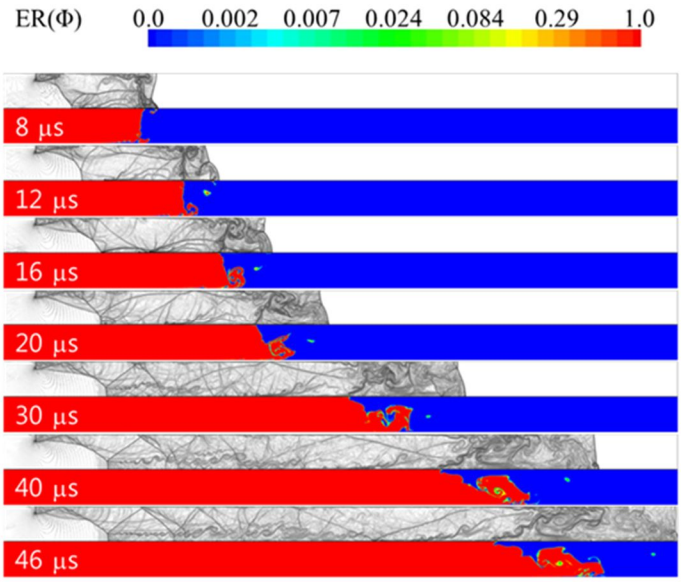

(a) Numerical Schlieren equivalence ratio

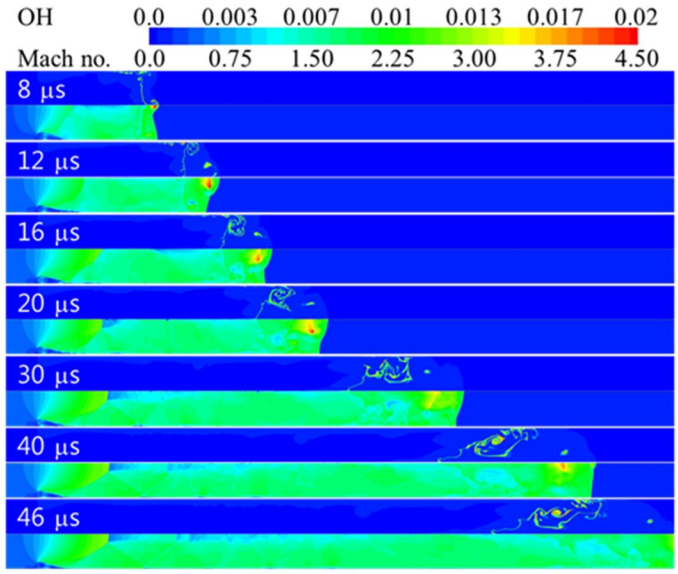

(b) OH mass fraction and Mach number contour

Figure 5-32 Result for a partial spherical pressure boundary: burst pressure 40 MPa

The results above are summarized in Figure 5-33, showing the schematics of ignition feature depending on the shape of pressure boundary and the burst pressure. The solid and dashed-dot lines present the wall and symmetric axis, respectively, and the red colored region presents the reaction regions. It is clear that the multi-dimensional shock interactions can play a critical role in the ignition by creating separated two mixing regions inside the tube, which occurs only when a spherical pressure boundary is applied as shown in figure 5-33(a) and figure 5-33(b). Also, the thin wall that remains after the burst of a disk can be helpful in initiating spontaneous ignition by aiding the reaction near the boundary layer can be developed. This can be proven by the results that no reaction region was generated when a full flat pressure boundary was applied, although the situation is unrealistic. However, as opposed to the previous results, it is observed that the reaction induced by a vortex ring in the core region or the merging of two reaction regions is not essential for spontaneous ignition. The spontaneous ignition can be initiated by only a reaction region developed from the boundary layer when a reaction in the core region disappears or is not generated when applying a full spherical or partial flat pressure boundary. The results showed that the ignition mechanism or ignition features can differ sensitively with the burst shape of the rupture disk, which is simulated by the pressure boundary in this paper when the burst pressure is relatively low as shown in figure 5-33(a). On the other hand, the ignition mechanism tends to be affected less sensitively with the shape of pressure boundary when the burst pressure is high. The ignition patterns are very similar regardless of partial or full spherical pressure boundary for burst pressure of above 20 MPa as shown in figure 5-33(b). In all of these cases, the reaction in the core region cannot play any role in

initiating the spontaneous ignition, as it disappears soon after the burst disk, but a complete flame is formed by a reaction region developed from the boundary layer, and the spontaneous ignition can be initiated.

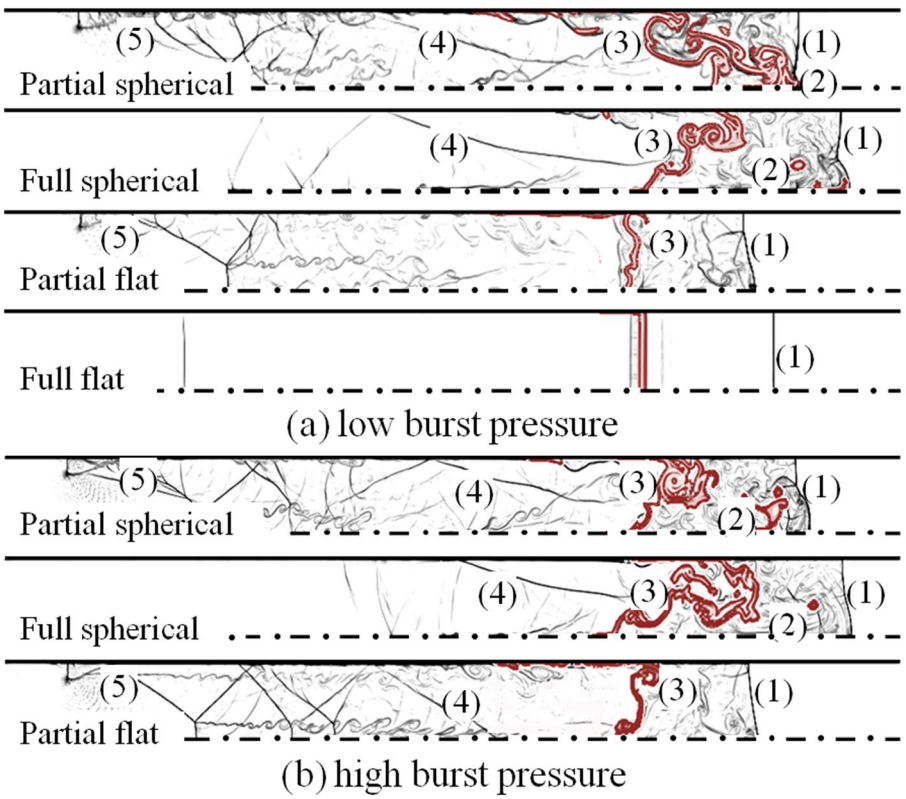

Figure 5-33 Schematic of ignition feature with burst conditions
(1) incident shock, (2) reaction in the core region, (3) reaction near the boundary layer, (4) multi-dimensional shock waves, (5) disturbance from the remaining of diaphragm

5.4 Effect of Obstacle

5.4.1 Effect of a wall on self-ignition patterns

In this chapter, the effect of an obstacle on self-ignition of high pressure hydrogen release due to burst of a diaphragm is investigated.[56] First, the three ignition patterns discussed previously have been reproduced by changing the tube length conditions while keeping the burst pressure constant. Then a series of experiments were conducted to investigate the effects of a wall on these different types of ignition pattern. The wall, which had a height of 1*D*, was located 2*D* from the exit. The results of the experiments were compared to those of a previous numerical study that conducted by Xu et al.[53].

Figure 5-34 shows the typical three different ignition types, non-ignition, failed-ignition and self-ignition at tube lengths of 10, 34, and 200 mm, respectively. The burst pressure of these cases was 14 MPa. In the case of non-ignition, only shadowgraph images are presented instead of direct images.

When the tube length was below 10 mm, no flame was detected inside and outside the tube (non-ignition). As shown in figure 5-34(a), when ignition has not occurred, high-pressure hydrogen leaving the tube shows a typical under-expanded flow pattern. And the shadowgraph does not show any gradient near the tube exit, unlike the shadowgraph of the self-ignition case that shows a gradient near the tube exit, figure 5-34(c). In another case with a 34 mm tube, a weak flame from the tube exit was observed for about 15 μsec but after that, the flame extinguished (failed-ignition), which may have resulted from the fast temperature decrease due to flow expansion.

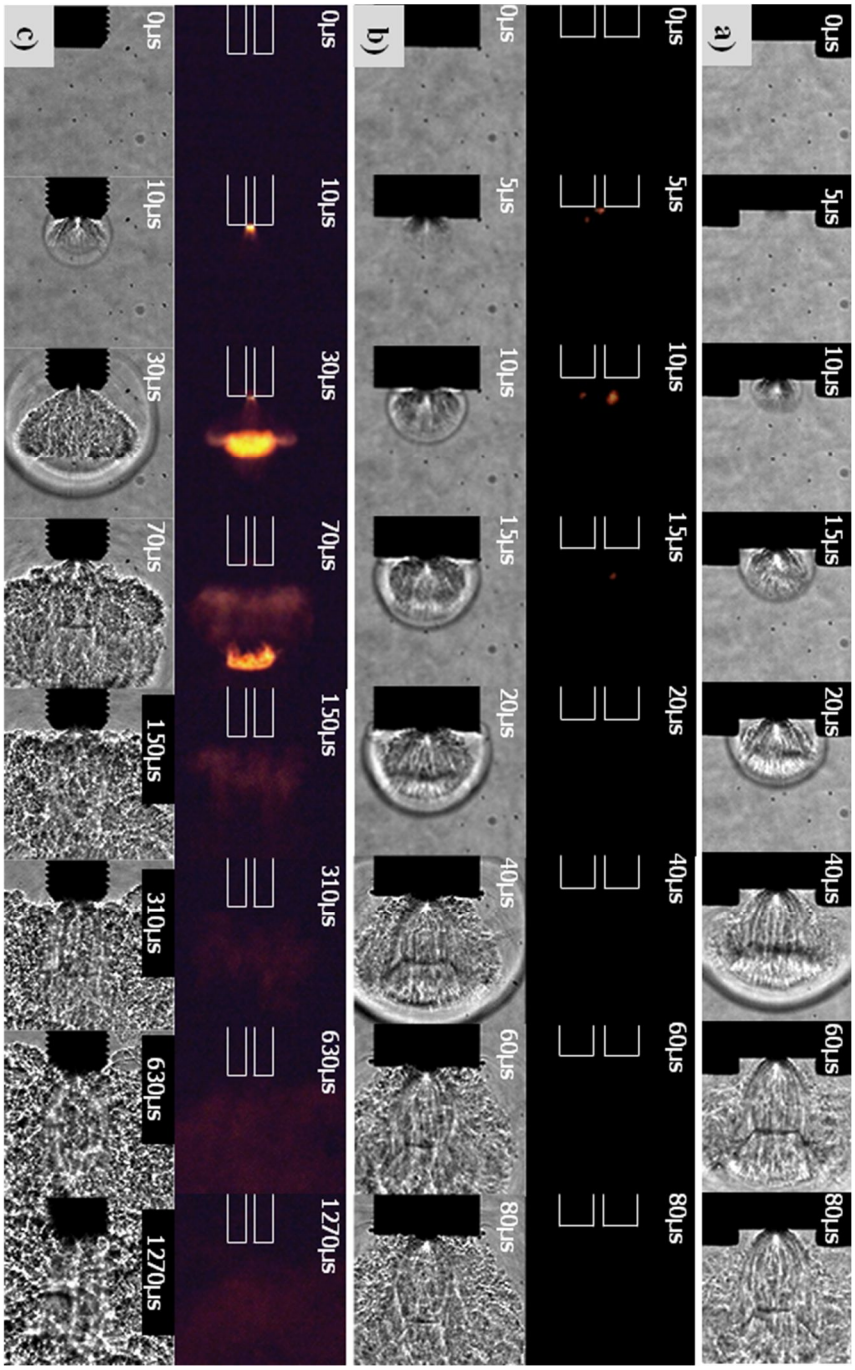

Figure 5-34 Three types of ignition pattern with different tube lengths at burst pressure of 14 MPa, (a) non-ignition (10 mm),
(b) failed-ignition (34 mm) (c) self-ignition (200 mm)

When the length was longer than 50 mm, a diffusion flame developed. In this case, a strong flame was observed at the tube exit before it was discharged. After the flame exited the tube, it slightly grew and separated into two flames. After the separation, surrounding air was entrained and the diffusion flame developed from the far side of the tube.

Experimental results with a wall at the same bursting conditions are shown in figure 5-35. When there was no flame inside the tube, the wall did not induce any reaction of this unburned mixture, as shown in figure 5-35(a). Figure 5-35(b) shows the result of a failed-ignition with a wall. The flame was extinguished after the same period as the no-wall condition. Although failed-ignition was expected to show a higher possibility of a reaction near the wall, direct imaging did not reveal any evidence of an additional reaction.

For the self-ignition case, the wall changed the direction of the flame. But phenomenon such as blow-off or secondary ignition was not observed, as shown in Figure 5-35(c). Figure 5-35(d) shows the recirculation region near the wall due to the impinging jet for a more detailed time interval than that of Figure 5-35(c). Figure 5-36 compares the Xu et al.'s numerical results [53] and present visualization images and shows a typical under-expanded flow structure around the impinging wall. The flow structure from the visualization image agrees well with that of the numerical results. It contains complex flow structures such as a leading shock, contact surface, shear layer, and plate shock near the wall. Even though the wall created stagnation points as shown in Figure 5-35(a), no changes in the ignition pattern were observed, meaning that for the non-ignition or the failed-ignition case, the temperature increase at a stagnation point was not enough to lead to a reaction or that the oxygen concentration in that region may have been too low to generate a flame.

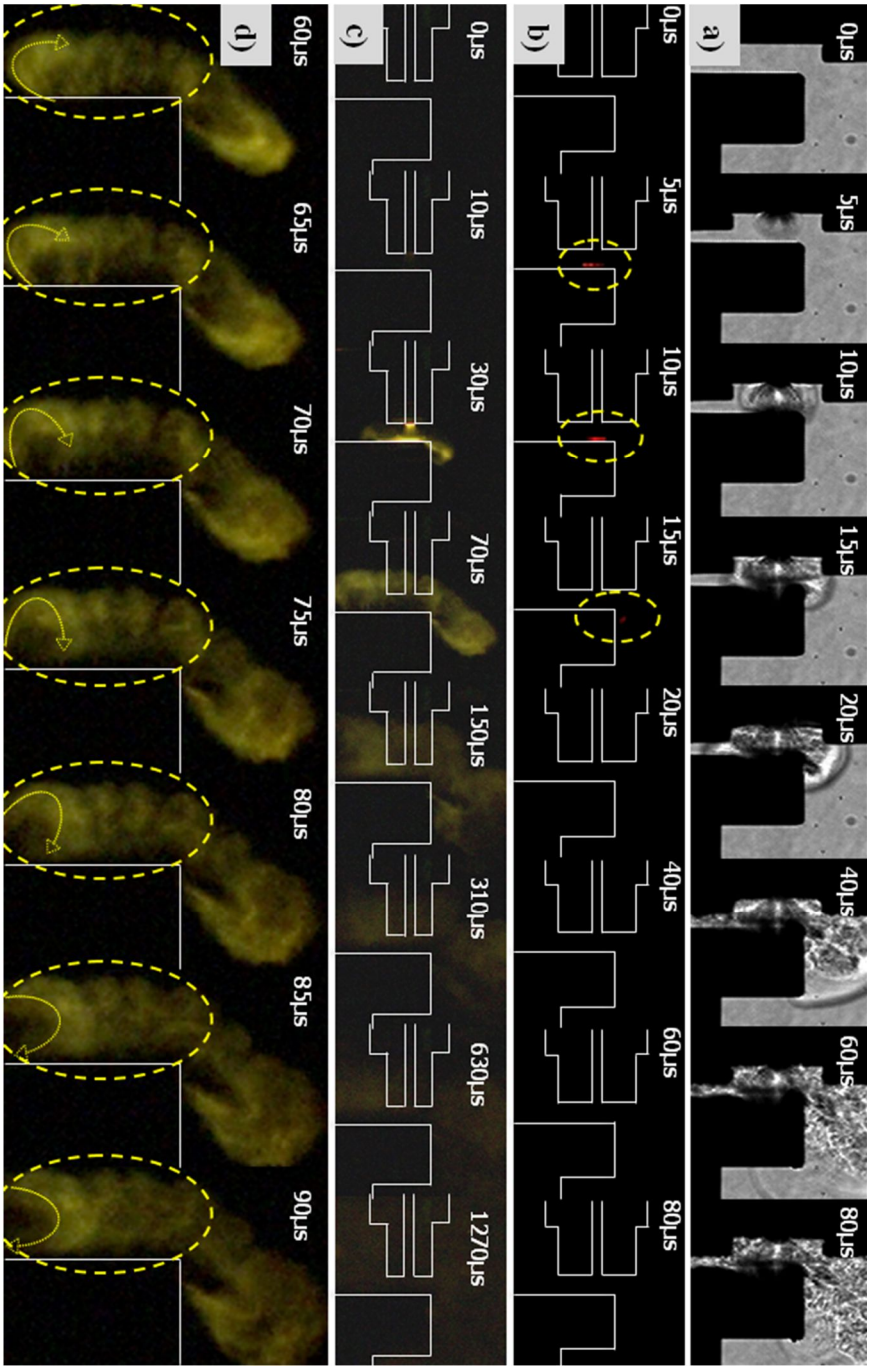

Figure 5-35 Effect of wall on three types of ignition pattern, wall height: 1D, distance: 2D, burst pressure: 14 Mpa, (a) nonignition (10 mm), (b) failed-ignition (34 mm), (c) self-ignition (200 mm) and (d) recirculation by the wall.

Moreover, as shown in Figure 5-36, mixing enhancements by the turbulence generated at the edge of the wall could not help to make this combustible mixture burn. This result agrees with the numerical studies of Xu et al. [53], in which a flame was not observed near the wall below 10 MPa.

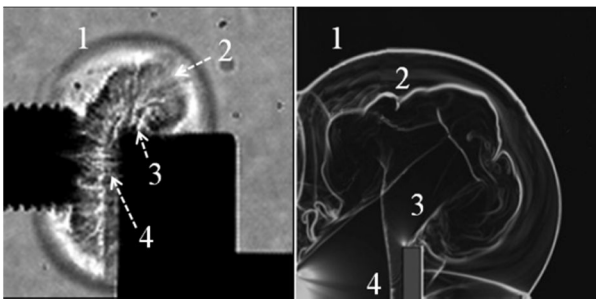

Figure 5-36 Flow structure around the impinging wall with under-expanded flow; experimental results (left) and numerical simulation (right), (1) leading shock, (2) contact surface, (3) shear layer and (4) plate shock

Xu et al.[53] simulated a case without a tube in order to eliminate shock interactions. However this experimental study used a short tube due to the thickness of the flange. According to previous results, a flame in a tube tends to be generated more easily when the tube is long because the mixing of air and hydrogen by multi-dimensional shock interactions can be enhanced in the tube. But a flame was not observed when the shortest tube was used, as shown in Figure 5-35(a). Even though the burst pressure was increased to a pressure higher than 30 MPa, a flame was not observed. Therefore, a wall may be capable of changing the direction or the intensity of a flame, but does not seem to fundamentally affect the ignition pattern. This result means that the generation of a strong flame inside the tube is the key feature that can explain hydrogen self-ignition when the burst pressure is less than 30 MPa.

Although the presence of the wall does not affect the ignition pattern, if an ignition takes place, the wall will aid in flame stabilization. As shown in figure 5-34(c) for a self-ignition case without an obstacle, the flame is separated into two parts, a leading flame that flows away from the exit and another flame that starts to develop. After that moment, the air is slowly entrained from the outer region and the flame stabilizes. It takes about 1,270 μsec for the flame to completely stabilize in the domain. But for the self-ignition case with a wall, the flame seems to stabilize without such flame separation and air entrainment. Comparing figure 5-34(c) and 5-35(c), the flame stabilizes in less than 630 μsec.

5.4.2 Effects of wall height on flame propagation

Generally, a gas handling system is exposed to diverse conditions. In this section, the effect of the surrounding geometry such as the height of the wall or the distance between the wall and the tube on the self-ignited flame is examined. To investigate the effect of the height of the wall on the self-ignited flame, the height was changed from 1*D* to 206*D*. Figure 5-37 shows the flame propagation for various heights at a fixed distance of 2*D*. The result without a wall is also inserted together for comparison. Figure 5-37(b) presents the direct images of the wall height of 10*D*. Compared to the wall height of 1*D* as shown in figure 5-35(c), this height is suitable for preventing direct flame propagation. As shown in figure 5-37(b), the initial flame was reflected at the facing wall. Around this reverse flow, the recirculation that is generated mixes and entrains the air around the flame, as indicated in figure 5-35(d). In this case, the flame split was not observed, but instead the collapse of the flame's boundary and the diffusion of the flame were observed. Figure 5-36(c) and 5-

37(d) show the flame development for wall heights of 100*D* and 206*D*.

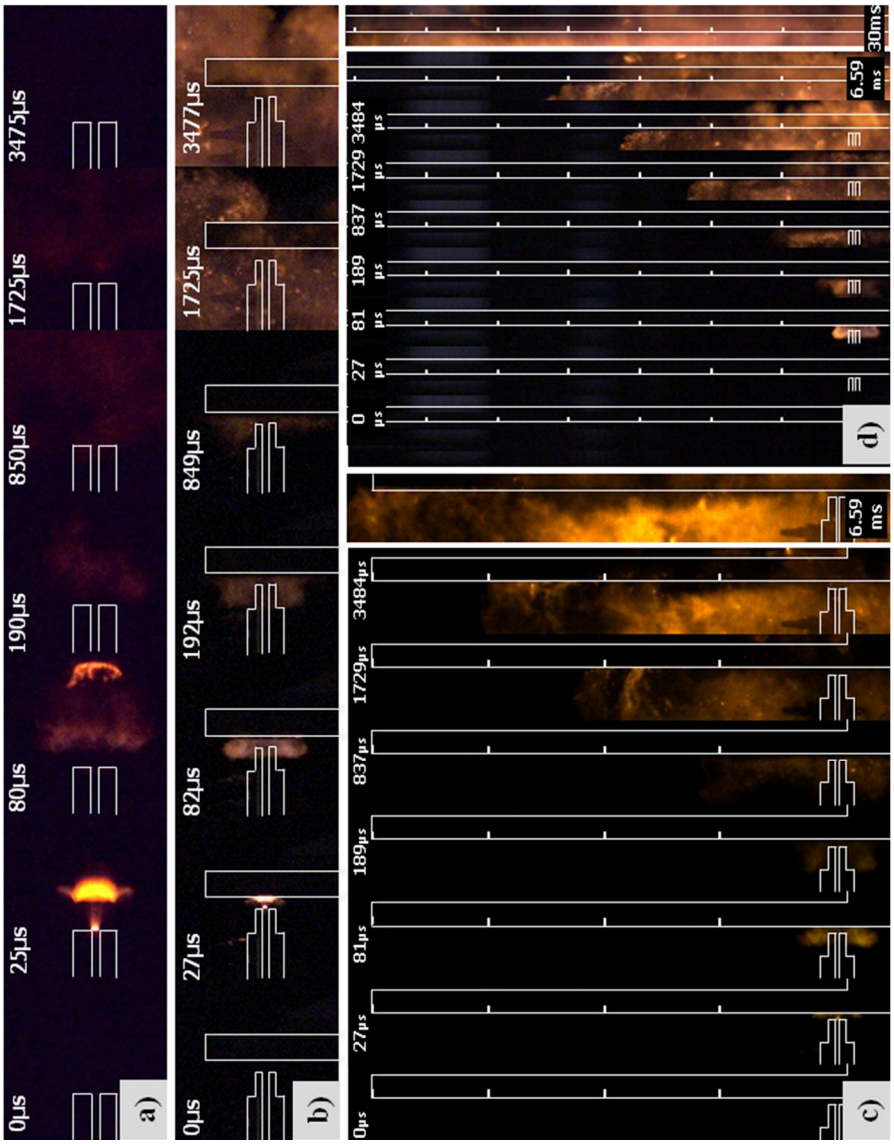

Figure 5-37 Height effect of wall for self-ignition, tube length: 200 mm, distance: 2D, burst pressure: 14 MPa,
(a) no-wall, (b) 10D, (c) 100D and (d) 200D

The tick marks are drawn at every *25D* from the center of the tube. In figure 6d, the height of the wall is 206*D* but only part of it, about 170*D*, is visualized because of the limitation of the view angle of the camera. Comparing the flame height of figure 5-37(c) with that of 5-37(d), the flame did propagate up to the same distance during the same period because there was no additional ignition, and the flame distribution was only governed by time and the hydrogen supply rate, which is driven by the burst pressure. Also, the flame propagated up to the end of the wall, regardless of the wall height, as shown in the last image of figure 5-37(c) and 5-37(d). This may have occurred because of the lighter molecular weight of hydrogen than that of air, as well as the momentum increase due to high pressure.

The results show that the flame propagation speed was not affected by the wall height when the burst pressure was the same and that the wall could not extinguish the flame by itself. But the wall height could affect the flame propagation and stabilization.

5.4.3 Effects of distance from the tube exit

In an actual situation, a pipe is not always installed near a wall or an obstacle. And hydrogen is a very diffusive gas, which means that the wall distance from the tube exit has a limited effect on self-ignition. This finding is shown in figure 5-38(b) and 5-38(c). Figure 5-38 presents the visualization images of flame propagation with respect to the wall distance from the tube exit. When the wall was set at 3*D* distance where the flame separation takes place, as shown in figure 5-34(a), the diffusion flame grew right after this impingement as shown in figure 5-38(a).

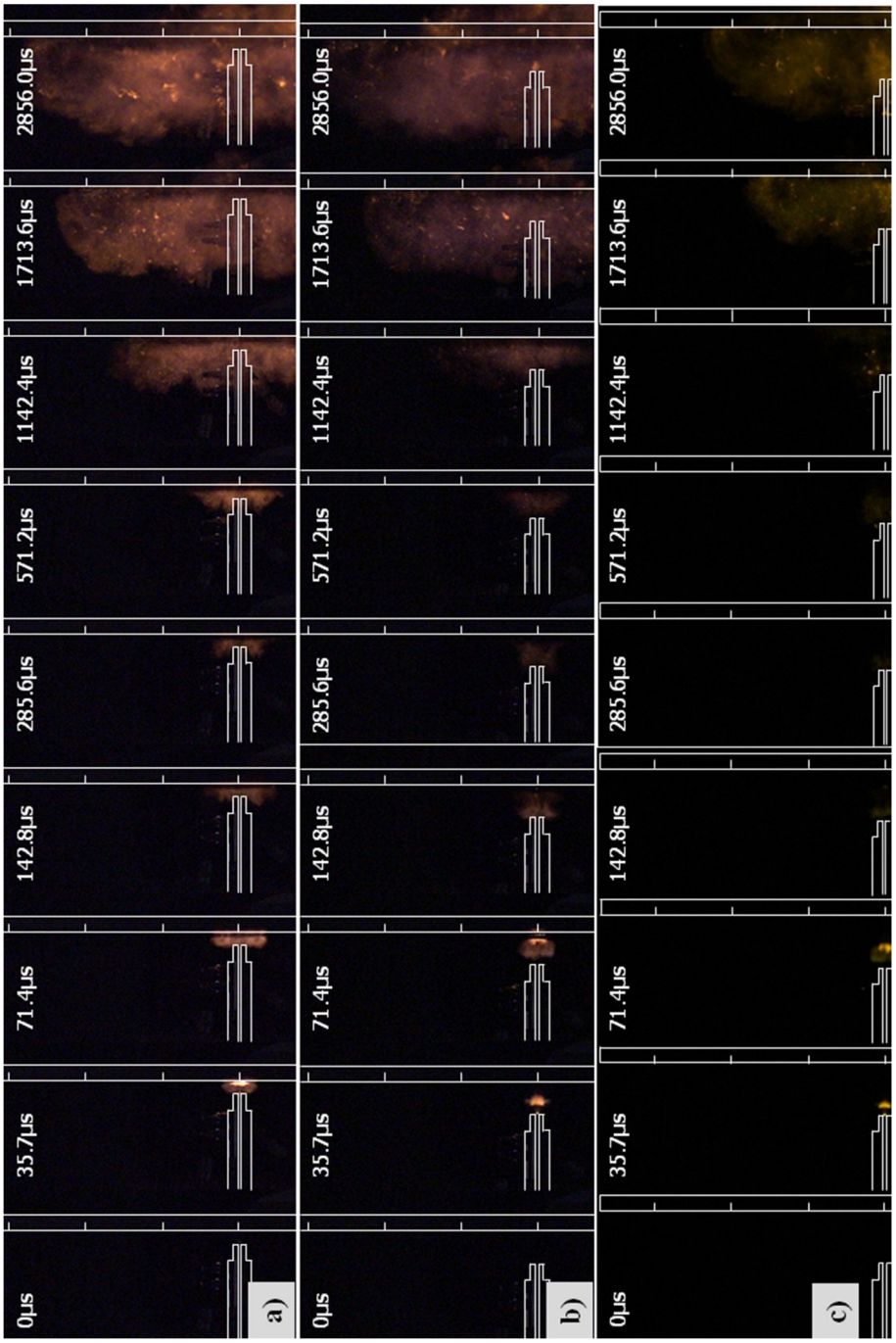

Figure 5-38 Effect of distance between wall and exit, tube length: 200 mm, burst pressure: 14 MPa, (a) 3D, (b) 10D and (c) 20D

Recirculation near the wall was found at that moment. But when the wall was detached from the tube at a distance greater than 10*D*, the blockage effect was not detected. Instead, flame separation and air entrainment were revisited, and the time at which the reinforced flame appeared near the tube was the same as that in the case without a wall. Nevertheless the flame propagated at different speeds for the 10*D* and 20*D* cases. This means that a wall located far away does not alter the flame development characteristics, but it holds the hydrogen in a certain region. Therefore an obstacle does not contribute to flame stabilization but rather accelerates the flame growth rate. Figure 8-5 also indicates that the rate of flame propagation is inversely proportional to the distance between the tube and the wall.

5.4.4 Effects of burst pressure on the self-ignition

Figure 5-39 shows the propagation of the flame at three different burst pressures. The results for burst pressures of 14, 10, and 8 MPa are presented because the possibility of self-ignition becomes too low below 8 MPa. A wall of 100*D* height was placed 2*D* away from the tube for these experiments. The exposure time was set to about 27 μsec so that the characteristics of flame propagation could be understood from a macroscopic view. At the initial stage of the self-ignited flame, the three figures show the same propagation phenomena: the flame boundary near the tube exit is the same up to until about 810 μsec. But after this time, the flame grows much faster at higher burst pressures. It seems higher burst pressures provide more momentum to the hydrogen jet to widen its spread.

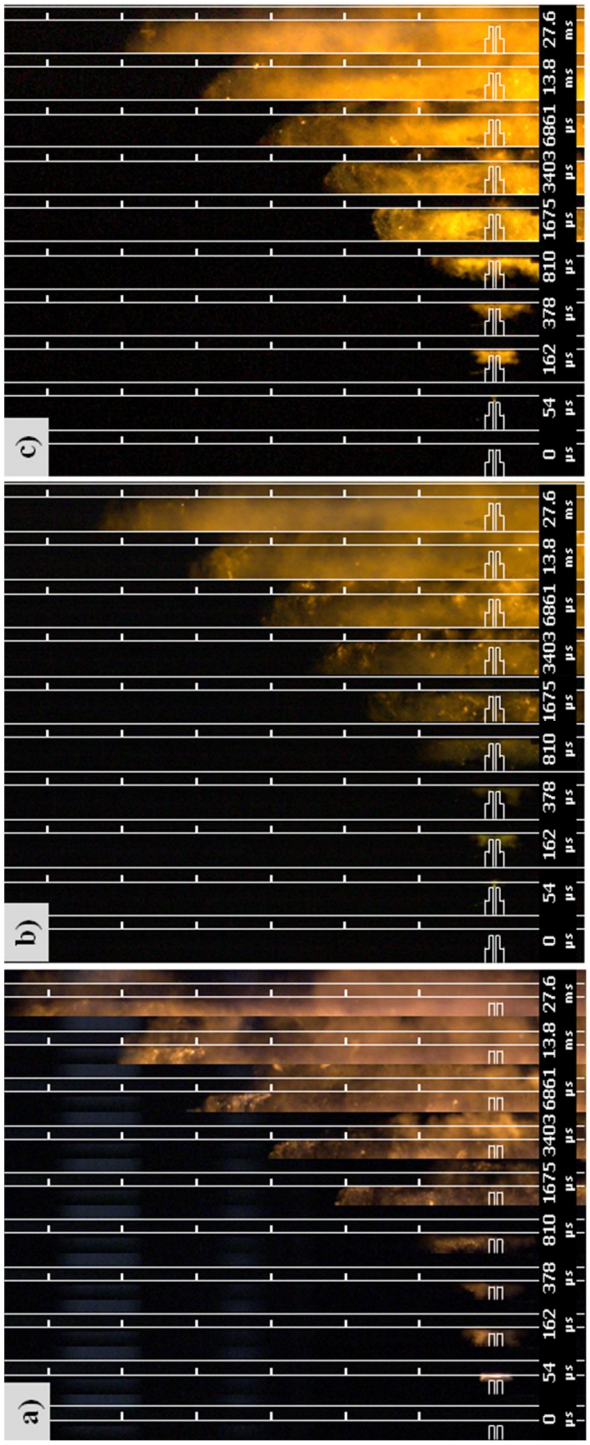

Figure 5-39 Burst pressure effect on flame propagation,
(a) 14 MPa, (b) 10 MPa and (c) 8 MPa

Chapter 6
Conclusion

In this thesis, the mechanism of spontaneous ignition of highly pressurized hydrogen and flame development/propagation are studied intensively. The results show that multi-dimensional shock wave from the diaphragm rupture and its interaction between shock and boundary layer has a significant effect on spontaneous ignition. Even though the detailed characteristics could be altered by the shape of the diaphragm geometry of the tube, the diffusion ignition of shock heated air and expanding hydrogen is identified as the most important mechanism. Study on the effect of exterior structure suggests that complete flame development before spouting from the tube is an essential prerequisite for self-ignition. Due to these reasons, research should be focused on the flow and flame characteristics inside the tube.

6.1 Summary

The main purpose of this research is to investigate self-ignition mechanism of the high pressurized hydrogen that is instantaneously released through an extension tube, and to study about safety issue at various leaking condition. To study the flow development and reaction, both experimental and numerical approach has been conducted.

In the experimental studies, commercial hydrogen is compressed up to

40 MPa using the boosting system. Then compressed hydrogen was fed into the secondary chamber in the test part. By integrating secondary chamber, stagnation condition could be obtained more easily and also measure accurate burst pressure through the feeding speed control.

The spontaneous ignition phenomena due to the high pressurized hydrogen released was investigated using high speed camera, pressure transducers, and photodiodes. Results from the experiment of relationship between tube length and burst pressure shows a general tendency that the propensity of spontaneous ignition is proportional to the burst pressure and extension tube length. Means that the shorter tube could be used to prevent the accident due to the failure of pressure vessel, valves or rupture disk. But if the burst pressure was increased to 23.5 MPa, the flame was observed at the exit even with 50 mm tube, which was not occurred when the burst pressure was 10.8 MPa. Furthermore, as the burst pressure was increased, the distance between a location of auto-ignition and a diaphragm was decreased. This tendency is resulted from the strong shock development and its forceful interaction with the boundary layer. In this study, although a flame development inside the tube was only observed using the photodiode due to the limit of structure, comparison between the signals and the direct images from the exit gives a consistent result. When the successful ignition was observed, the luminance was increased as the flame approached the exit of the tube. These results suggest that the complete flame was easy to be generated when the longer tube was installed, and this entire cross-section covered flame seems to have more energy to be sustained during the expansion. Whereas, when the length of tube was not enough to develop complete flame, only the flame near the boundary, which was extinguished due to the expansion, was

observed.

Other experiment was conducted to investigate an effect of obstacles near the pipe system that mimic real applications such as hydrogen car refueling station or safety wall surrounding high pressure tubes. In the study, distinctive ignition pattern following the tube length has been constructed. Then an obstacle having various height or distance from the exit was installed. The results have been analyzed using direct and shadowgraph images taken at the exit of tubes. The result suggests that the wall could alter the flow structure in front of the surface, has no effect on the ignition characteristics of hydrogen-air mixture. Although a stagnation point was generated near the wall, a flame was not induced for the non-ignition and failed-ignition conditions, because tubes were too short to a strong flame be developed inside the tube. The results remained intact even the burst pressure increased up to 30 MPa. On the other hand, the presence of a wall led to shorter stabilization times because it influenced the flame separation and air entrainment for the self-ignition condition. However, the effect disappeared when the wall distance was greater than 10D.

Investigation of the flow structure and flame development near the diaphragm where the direct visualization is difficult was conducted using a sophisticated numerical simulation code.

In the previous research, a remaining of a fraction of diaphragm was detected after the experiment. To study the effect of this remaining on the flow development and ignition characteristics, four different types of pressure boundary were designed and tested at large spectrum of burst pressure. When the partial spherical boundary condition has been applied, reflected shock was focused on the axis and the ignition occurred in two reaction region, core and

boundary. Then two reaction regions merged into a complete flame as travelling the downstream. However a shock focusing was not observed for the full spherical boundary condition. In this case, the flame only developed near the boundary layer. This result suggest that the possibility of the spontaneous ignition by only the flame developed at the boundary layer, which is similar to the result of previous experiment with rectangular cross-sectional extension tube. However the effect of pressure boundary shape is diminished as the burst pressure increases. When the burst pressure is high enough, the ignition characteristics and flow development has similar tendency with each other. In this case, the flame starts to grow from the reaction region near the boundary layer independently from the shape of pressure boundary.

Last part of this thesis deals with the flow inside the tube with different inner diameter. In previous experiments, there were two different ignition patterns at the same burst pressure. The only difference was the inner diameter of extension tubes. To investigate the mixing and the flame development inside the tube, tubes that has 3 mm and 10.9 mm inner diameter were modeled with the Cartesian grid of 10 micrometer size. In the 3 mm tube, the multi-dimensional shock waves and vortex generated by the rupture of diaphragm were weakened after a few μsec. Then the initiated flame stabilized before it left the tube. The stabilized flame grew from the boundary layer and a complete flame across the cross-section was formed. However when the tube diameter was increased, the effect of the rupture of pressure boundary was sustained for a long time. The vortex made the shock heated air and hydrogen mixed which eventually ignited near the mixing surface. But these smaller flames did not merged into a complete flame before approaching

the exit. It seems to the reason why the former case had sustainable flame after the spouting and the later showed the failed-ignition pattern. The result also confirmed that the flame near the boundary had ability to generate a complete flame which could be sustained after expansion.

6.2 Future work

In this study, the mechanisms of the spontaneous ignition phenomena considering the fundamental bursting condition are investigated using experimental and numerical approaches. However to use the hydrogen safely in an actual situation, detailed studies on the specific burst conditions and the interaction with surrounding structures should be considered. Also as the developed code is focused on the simulations of the reacting flow inside the tube, a flame spouting into the air could not be simulated in the study which is important in the realistic case. For aforementioned reasons, researchers who study high pressurized hydrogen are expected to consider followings.

Develop a program which has a capable of either three dimensional computations or rigorous turbulent modeling to calculate both inside and outside of the tube. Although most of studies assume that the diaphragm has been ruptured instantaneously, every time the rupture disk has been broken an opening speed or shape could be varied. As the variation affects downstream flow inside the tube, it is expected that the flame development process is also changed. Few research groups try to reveal the effect of rupture disk opening dynamics, nothing is proven yet. By considering this effect, more realistic values from the simulation, such as ignition delay, could be obtained. Finally,

the effect of an obstacle outside the tube is studied just for the flat plate. However to confirm the general tendency, it should be considered that the effect of a typical structure, such as cavity or bump.

Appendix

In the study, to handle the massive data efficiently from the numerical study, the newest techniques have been implemented into computational program. Here, two major efforts are introduced.

A. Binary I/O

The program imports external libraries from Tecplot 360 and VisIt visualization tool. Tecplot is very powerful data processing package and commonly used. The package provides a method to write a data into a binary form whose size is very small compared to ascii format data.[58] Another merit is the Tecplot quickly loads the data which is already converted as a binary format. Moreover with a little effort, older program, which write a data into a ascii format, could be modified. The cell-centered data averaging the finite volume and the locations of grid points forming the finite volume could be written either in a structured or in an unstructured data form. However, as the binary output file has own format, other data processing package could not be used.

Subroutine ; Writeflow

```
implicit none
real*8 ::r,u,v,p,t,c
real*8 ::y_h2,y_o2,y_oh,y_h2o
real*8 ::fo_stoic,fo_local,eqratio,eqsym,yleast
integer*4 tecini111,tecend111,tecdat111,teczne111
```

```
      character*1    nullchr
      integer*4 nnod,ncen,ndat
      integer*4 debug,visdouble,filetype
      integer*4 zonetype,strandid,parentzn,isblock
      integer*4    nfconns,fnmode,shrconn
      integer*4    valuelocation
      dimension valuelocation(14)
      pointer (nullptr,null)
      integer*4    null(*)

      nullchr = char(0)
      nullptr = 0
      debug          = 0          ! 0=no-debug, 1=debug
      filetype    = 0          ! 0=full, 1=grid, 2=solution
      visdouble = 1          ! 0=single precision, 1=double precision
      zonetype    = 0          ! 0=ordered
      strandid    = 0          ! 0=static zone
      parentzn    = 0          ! 0=not associated with a parent zone
      isblock     = 1          ! 0=point, 1=block
      nfconns     = 0
      fnmode       = 0
      shrconn     = 0

      data valuelocation /1,1,0,0,0,0,0,0,0,0,0,0,0,0/

! output
      iret = tecini111('Hydrogen'//nullchr, 'X Y RHO U V P T M YH2
      YO2 YOH YH2O YR EQS'//nullchr, fntec//nullchr, '.'//nullchr,
```

```
      filetype, debug, visdouble)

! write zone data for each block
      iret=teczne111(zntec//nullchr, zonetype, imax, jmax, 1, 0, 0, 0, time,
      strandid, parentzn, isblock, nfconns, fnmode, 0, 0, 0, null,
      valueLocation, null, shrconn)

! NODE data
      nnod = imax*jmax
      iret = tecdat111(nnod,x(1:imax,1:jmax),1)
      iret = tecdat111(nnod,y(1:imax,1:jmax),1)

! CENTER data
      ndat = 12
      ncen = imm1*jmm1*ndat
      allocate(var(imm1,jmm1,ndat))
      fo_stoic = 2.d0*amw(ih2)/amw(io2)

      do j=1,jmm1
      do i=1,imm1
         r = qij(mr,i,j)
         u = qij(mu,i,j)/r
         v = qij(mv,i,j)/r
         p = qij(mp,i,j)
         t = qij(mt,i,j)
         c = qij(mc,i,j)
         y_h2 = qij(ih2,i,j)/r
         y_o2 = qij(io2,i,j)/r
```

```
y_oh = qij(ioh,i,j)/r
y_h2o= qij(ih2o,i,j)/r
if(qij(ih2,i,j).lt.nearzero) then
   fo_local = 0.d0
else if(qij(io2,i,j).lt.nearzero) then
   fo_local = verybig
else
   fo_local = qij(ih2,i,j)/qij(io2,i,j)
endif
eqratio = fo_local/fo_stoic
eqsym = eqratio/(1.d0+eqratio)
if(eqratio.le.1.d0) then
   yleast = y_h2
else
   yleast = fo_stoic*(1.d0-y_h2)
endif
var(i,j, 1) = r
var(i,j, 2) = u
var(i,j, 3) = v
var(i,j, 4) = p
var(i,j, 5) = t
var(i,j, 6) = dsqrt(u**2+v**2)/c
var(i,j, 7) = y_h2
var(i,j, 8) = y_o2
var(i,j, 9) = y_oh
var(i,j,10) = y_h2o
var(i,j,11) = yleast
var(i,j,12) = eqsym
```

```
        enddo
        enddo
        iret = TecDat111(ncen,var,1)
        deallocate(var)
        iret = TecEnd111()

    ! restart
        open(4,file=fnflo,status='unknown',form='unformatted')
        write(4) icycle,iter,time
        do iv=1,nv
          write(4) ((qij(iv,i,j),i=1,imm1),j=1,jmm1)
        enddo
        close(4)

        end
```

B. In-Situ Data Visualization

As mentioned, the program also imports external libraries from VisIt visualization tool. Although massive data processing techniques try to enhance the efficiency by integrating parallel computation, graphic core processing, binary data writing, and etc., these methods require understanding of data I/O hierarchy with storage. However, supercomputers show a few times faster than the capacity of I/O bandwidth. For this reason, intermittent data has been left out or all data in a memory could not be stored. Even

though the information was not critical to analyze the physical phenomena, it could be a useful data for a certain procedure.

To solve this problem, VisIt provides a simulation library that is capable of providing simulation data to the user. Figure A-1 shows the VisIt architecture that explains how the library(LIBSIM) communicates with the simulation.

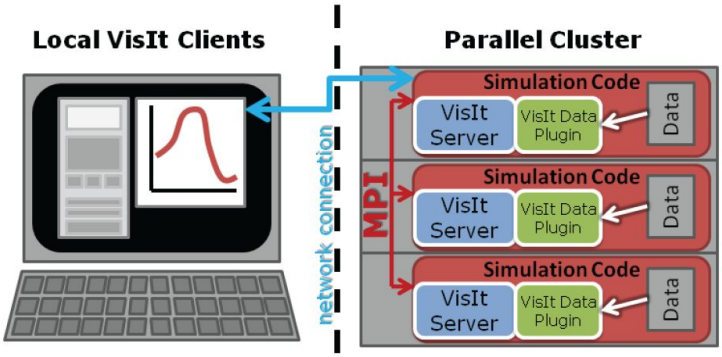

Figure A-1 VisIt architecture diagram

A computational code has to be modified to integrate the VisIt library interface. In order for VisIt to connect to the simulation, LIBSIM creates a listening socket that can be used to detect inbound VisIt connections. After the modification, new program follows the typical steps listed below,

1. The simulation code launches and starts execution.

2. The simulation regularly checks for connection attempts from VisIt clients.

3. When a VisIt client attempts to connect, the simulation loads the VisIt server library and allows it to complete the connection.

4. The VisIt server asks the simulation for a description of its meshes and data types.

5. Either running or paused, the simulation relies on the VisIt server to handle any VisIt-specific operations, handing it pointers to data when requested.

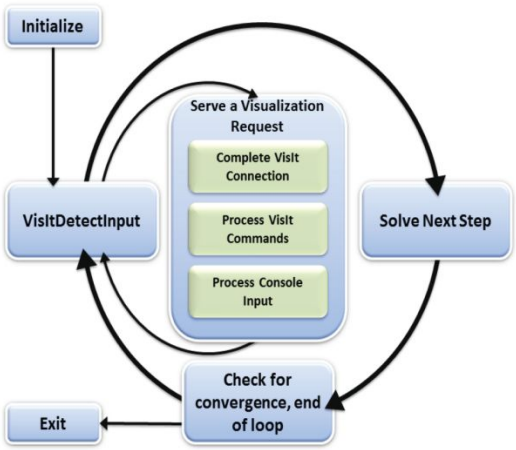

Figure A-2 Simulation control flow after introducing in situ processing

Subroutine ; Main_insitu

```
program
        use params
        use visit_variables
        implicit none
        include 'visitfortransimV2interface.inc'    ! VISIT in-suit
        include 'mpif.h'

!VISIT in-suit
        integer:: processvisitcommand
        integer:: visitstate, visitresult, visitblocking, visitierr
```

```
integer:: visitconnect
character (len=1024) :: visit_trace = 'visit_trace.out'
character (len=1024) :: visit_path    = ''
character (len=1024) :: visit_args    = '-debug 5 -pid'
character (len=1024) :: visit_simbase = 'visit_insuit'
character (len=1024) :: visit_simcomment = 'Hydrogen Release into the
                                            tube simulation'
character (len=1024) :: visit_simpath = VISIT_F77NULLSTRING
character (len=1024) :: visit_siminput = VISIT_F77NULLSTRING
character (len=1024) :: visit_simgui = VISIT_F77NULLSTRING

call MPI_INIT(ierr)
call MPI_COMM_SIZE(MPI_COMM_WORLD,nprocs,ierr)
call MPI_COMM_RANK(MPI_COMM_WORLD,myrank,ierr)

!VISIT in-suit
!Determin the rank and size of this MPI task so we can tell
!VisIt's libsim about it
visiterr = 0
if(nprocs.gt.1) then
   visiterr = visitsetparallel(1)
endif
visiterr = visitsetparallelrank(myrank)
visiterr=visitopentracefile(visit_trace,len_trim(visit_trace))

visiterr = visitsetupenv()
!Have the master process write the sim file
if(myrank.eq.0) then
```

```
          visiterr = visitinitializesim(visit_simbase,len_trim(visit_simbase),
         >                    visit_simcomment,len_trim(visit_simcomment),
         >                              visit_simpath,len_trim(visit_simpath),
         >                           visit_siminput,len_trim(visit_siminput),
         >                              visit_simgui,len_trim(visit_simgui),
         >    VISIT_F77NULLSTRING, VISIT_F77NULLSTRINGLEN)
        endif
    !VISIT in-suit, done Prepare

        call mpi_barrier(mpi_comm_world,ierr)
        call read_data_needed

        !VISIT in-suit
        allocate (visitx(imax,jmax))
        allocate (visity(imax,jmax))
        allocate (visit_var_2d_mem(nv,imax,jmax))

        do j=1,jmax
        do i=1,imax
           visitx(i,j) = x(i,j)
           visity(i,j) = y(i,j)
        enddo
        enddo
        !VISIT in-suit

        if(myrank.eq.0) then
          write(*,*) ' Ready to go! '
        end if
```

```
!VISIT in-suit
      visitrunflag    = 1
      visitsimcycle = 0
      visitsimtime    = 0

! Computation Start
      do while(under_cycle)

      !VISIT in-suit
         if (visitrunflag.eq.1) then
            visitblocking = 0
         else
            visitblocking = 1
         endif

         if(myrank.eq.0) then
            visitstate = visitdetectinputwithtimeout(visitblocking,0,-1)
            endif
         call MPI_BCAST
         if (visitstate.lt.0) then
            under_cycle = .false.
            icycle = icyclemax + 100
            write(*,*) 'Can not recover from error!'
            visitconnect = VisItDisconnect()
            if (visitconnect.ne.VISIT_OKAY) then
               write(*,*) 'VisIt: disconnect failed!'
            else
```

```
            write(*,*) 'VisIt: disconnected.'
        endif
    elseif (visitstate.eq.0) then              ! No VisIt connection detected
        call main_computation_loop
        visitsimcycle = visitsimcycle + 1
        visitsimtime = visitsimtime + dtmin
    elseif (visitstate.eq.1) then
        visitrunflag = 0
        do j = 1,jmm1
        do i = 1,imm1
            do iv=1,nv
                visit_var_2d_mem(iv,i,j) = qij(iv,i,j)
            enddo
        enddo
        enddo
        visit_var_2dp => visit_var_2d_mem
        call mpi_barrier(mpi_comm_world,ierr)
        visitresult = visitattemptconnection()
        if (visitresult.eq.1) then
            write(*,*) 'VisIt connected!',myrank+1,visitsimcycle
        else
            write(*,*) 'VisIt did not connect!',myrank+1,visitsimcycle
        endif
    elseif (visitstate.eq.2) then
        visitrunflag = 0
        if (processvisitcommand().eq.0) then
            visitresult = visitdisconnect()
            visitrunflag = 1
```

```
        else
           write(*,*) 'VisIt: disconnect failed!'
        endif
     endif
end do
deallocate(visitx)
deallocate(visity)
deallocate(visit_var_2d_mem)

call MPI_FINALIZE(ierr)
stop
end
```

BIBLIOGRAPHY

[1] M.G. Zabetakis, *Safety with Cryogenic Fluids*, Plenum Press New York, 1967

[2] H. Eichert, et al., *Potential risk for an increased use of hydrogen*, German Research Center for Aerospace, 1992.

[3] A. Gasse, "Experimental determination and simulation of explosion limits, studied in hydrogen containing fuel gas mixture" (Ph.D thesis, University of Paderborn, Aachen, Germany,1992)

[4] G.R. Astbury, "Review of unidentified ignition sources of unplanned flammable releases – Comparison of Offshore and Onshore data" (Report Number HSL/2006/09)

[5] http://www.hse.gov.uk/infoserv/mhidas.htm.

[6] G.R. Astbury and S.J. Hawksworth, "Spontaneous ignition of hydrogen leaks: A review of postulated mechanisms," International Journal of Hydrogen Energy, Vol. 32, pp.2178-2185, 2007

[7] Anon, "Spontaneous ignition of hydrogen," Engineering, Vol. 113, p.502, 1922

[8] R.W. Fenning, and F.T. Cotton, "Two Unexpected Hydrogen-Air Explosions," Engineering, Vol. 130, p.252, 1930

[9] J. Bond, *Sources of Ignition: Flammability Characteristics of Chemicals and Products*, Butterworth Heinemann, 1991

[10] R. Reider, H.J. Otway, and H.T. Knight, "An Unconfined Large Volume Hydrogen/Air Explosion," Pyrodynamics, Vol. 2, p.249, 1965

[11] "Safety standard for hydrogen and hydrogen systems," (National Aeronautics and Space Administration Report, Report NSS 1740.16, p.A-16, 1997)

[12] J.H. Perry, *Chemical engineers, handbook. 4th ed.*, New York, 1963

[13] A. Michels, W. de Graaff, and G.J. Wolkers, "Thermodynamic properties of hydrogen and deuterium between -175°C and 150°C and at pressures up to 2500 atmospheres," Applied Scientific Research, Section A, Vol. 12, No. 1, pp.9-32, 1964

[14] "Basic considerations for the safety of hydrogen systems" (International Standards Organization Technical Report ISO/TR 15916, 2000)

[15] N. Gibson and D.J. Harper "Parameters for assessing electrostatic risk from non-conductors – a discussion," Journal of Electrostatics, Vol. 21, No. 1, pp.27-36, 1988

[16] G.P. Ackroyd and S.G. Newton, "An investigation of the electrostatic ignition risks associated with a plastic coated metal," Journal of Electrostatics, Vol. 59, No. 2, pp.143-151, 2003

[17] V.J. Schaefer, *Properties of particles of snow and the electrical effects they produce in storms*, American Geophysical Union, 1947

[18] P.R. Camp, "Charge morphology and pH of natural snow," Journal of Geophysical Research, Vol. 81, No. 9, pp.1589-1592, 1976

[19] D.A. Burrows and P.V. Hobbs, "Electrical charges on snow particles," Journal of Geophysical Research, Vol. 75, No. 24, pp.4499-4505, 1970

[20] P. Wolanskei and S. Wojcicki, "Investigation into the mechanism of the diffusion ignition of a combustible gas flowing into an oxidizing atmosphere," Proceedings of the Combustion Institute Vol. 14 pp.1217-1223, 1972

[21] International Electrotechnical Commission, "Electrical apparatus for explosive gas atmospheres-part 20: data for flammable gases and vapors, relating to the use of electrical apparatus" (Standard IEC 60079-20, 2000)

[22] *Fire protection guide on hazardous materials, 325M, 9th ed.*, National Fire Protection Association, Massachusetts, 1986

[23] L. Pan, S.A. Fisher, S. Jayanti, and G.F. Hewitt, "Measurement and prediction of temperature rise following sudden compression in a high-pressure pipline," Process safety and environmental protection, Vol. 73, No. 1, pp.18-20, 1995

[24] T.M. Cain, "Autoignition of hydrogen at high pressure," Combustion and Flame Vol. 111, No. 1, pp.124-132, 1997

[25] M. E. Neer, "An investigation into spontaneous ignition in flowing hydrogen air mixture" (Ph.D. thesis, Ohio State University; 1972)

[26] E.M. Bulewicz et al. "The ignition of hydrogen-oxygen mixture from a hot surface," Archiwum Termodynamiki I palania, Vol. 8, No.1, pp.85-93, 1977

[27] G. Chaineaus, G. Mavrothalassitis, and J. Pineau, "Modelization and validation test of the discharge in air of a vessel pressurized by a flammable gas," Progress in Astronautics and Aeronautics, Vol. 134, pp.104-137, 1990

[28] F. L. Dryer, M. Chaos, Z. Zhao, J. N. Stein, J. Y. Alpert, and C. J. Homer, "Spontaneous Ignition of Pressurized Releases of Hydrogen and Natural Gas into Air," Combustion Science and Technology, Vol. 179, pp.663-694, 2007

[29] V.V. Golub, D.I. Baklanov, S.V. Golovastov, M.F. Ivanov, I.N. Laskin, A.S. Saveliev, N.V. Semin, and V.V. Volodin, "Mechanisms of high-pressure hydrogen gas self-ignition in tubes," Journal of Loss Prevention in the Process Industries, Vol. 21, pp.185-198, 2008

[30] T. Mogi, D. Kim, H. Shiina, and S. Horiguchi, "Self-ignition and explosion during discharge of high-pressure hydrogen," Journal of Loss Prevention in the Process Industries, Vol. 21, pp.199-204, 2008

[31] J.X. Wen, B.P. Xu, and V.H.Y. Tam, "Numerical study on spontaneous ignition of pressurized hydrogen release through a length of tube," Combustion and Flame, Vol. 156, pp.2173-2189, 2009

[32] B.J. Lee and I.-S. Jeung, "Numerical study of spontaneous ignition of pressurized hydrogen released by the failure of a rupture disk into a tube," International Journal of Hydrogen Energy, Vol. 34, pp.8763-8769, 2009

[33] P.H. White, "Effect of Transducer Size, Shape and Surface Sensitivity on the Measurement of Boundary Layer Pressure," The Journal of Acoustical Society of America, Vol. 41, No. 5, pp.1358-1363, 1967

[34] G. Schewe, "On the Structure and Resolution of Wall-Pressure

Fluctuations Associated with Turbulent Boundary-Layer Flow," Journal of Fluid Mechanics, Vol. 134, pp.311-328, 1983

[35] R.D. Hanly, "Effects of Transduce Flushness on Fluctuating Surface Pressure Measurements," AIAA Paper 75-534, 1975

[36] H. Herbrich, "Die Schlieren photographie – ein optisches Diagnoseverfahren," Sensor, Vol. 3, pp.5-9, 1990

[37] D.W. Holder and R.J. North, "Schlieren methods" (NPL notes on Applied Science No. 31. Her Majesty's Stationery Office, London, 1963)

[38] F.J. Weinberg, *Optics of flames: including methods for the study of refractive index fields in combustion and aerodynamics*, Butterworths, London, 1963

[39] G.S. Settle, *Schlieren and Shadowgraph Techniques*, Springer, 2001

[40] H. Schardin, "Das Toeplersche Schlierenverfahren: Grundlagen fur seine Anwendung und quantitative Auswertung," VDI-Forschungsheft No 367, Vol. 5, No. 4, pp.1-32, 1934

[41] L.A. Vasiliev, *Schlieren methods*, Israel Program for scientific translations, New York, 1971

[42] H. Wolter, "Schlieren, phase contrast, and light-section method," Fundamentals of Optics, Handbook of Physics, Vol. 24, pp. 555-645, 1956

[43] R.A. Burton, "The application of schlieren photography in fluid flow and heat transfer analysis" (M.S. Thesis, University of Texas, 1951)

[44] M.R. Davis, "Determination of turbulent flow properties by

penetrating beam dynamic shadowgraph method," Journal of Physics E, Vol. 20, No. 10, pp.1271-1277, 1987

[45] M.R. Davis, and H.L. Li, "Evaluation of fractal dimension for mixing and combustion by the schlieren method," Experiments in Fluids, Vol. 21, No. 4, pp. 248-258, 1996

[46] W.F. Hilton, *High-speed aerodynamics*, Longmans & Green, NY, 1951

[47] Y. Wada and M.-S. Liou, "An accurate and robust flux splitting scheme for shock and contact discontinuities," SIAM Journal on Scientific Computing, Vol. 18, No. 3, pp. 633-657, 1997

[48] E. Hairer and G. Wanner, *Solving Ordinary Differential Equations II, Stiff and Differential-Algebraic Problems, Second Edition*, Springer, 1996

[49] D. Goodwin, *Cantera: An object-oriented software toolkit for chemical kinetics, thermodynamics, and transport processes,* Caltech, Pasadena, 2009

[50] M. P. Burke, M. Chaos, Y. Ju, F. L. Dryer, and S. J. Klippenstein, "Comprehensive H2/O2 Kinetic Model for High-Pressure Combustion," International Journal of Chemical Kinetics, Vol. 44, No. 7, pp. 444-474, 2012

[51] E. Yamada, S. Watanabe, A. K. Hayashi, and N. Tsuboi, "Numerical analysis on auto-ignition of a high pressure hydrogen jet spouting from a tube," Proceedings of the combustion institute, Vol. 32, No. 2, pp. 2363-2369, 2009

[52] Y.R. Kim, H.J. Lee, S. Kim, and I.-S. Jeung, "A flow visualization study on self-ignition of high pressure hydrogen gas

released into a tube," Proceedings of the combustion institute, Vol. 34, No. 2, pp. 2057-2064, 2013

[53] B.P. Xu, J.X. Wen, and V.H.Y. Tam, "The effect of an obstacle plate on the spontaneous ignition in pressurized hydrogen release: A numerical study," International Journal of Hydrogen Energy, Vol. 36, pp.2637-2644, 2011

[54] H. Yamashita, M. Shimada, and T. Takeno, "A Numerical Study on Flame Stability at the Transition Point of Jet Diffusion Flames," Proceedings of the combustion institute, Vol. 26, No. 1, pp. 27-34, 1996

[55] Chung K. Law, *COMBUSTION PHYSICS*, Cambridge University Press, 2006

[56] S. Kim, H.J. Lee, J.H. Park, and I.-S. Jeung, "Effects of a wall on the self-ignition patterns and flame propagation of high-pressure hydrogen release through a tube," Proceedings of the combustion institute, Vol. 34, No. 2, pp. 2049-2056, 2013

[57] H.J. Lee, Y.R. Kim, S. Kim, and I.-S. Jeung, "Experimental investigation on the self-ignition of pressurized hydrogen released by the failure of a rupture disk through tubes," Proceedings of the combustion institute, Vol. 33, No. 2, pp. 2351-2358, 2011

[58] *Tecplot 360 Data Format Guide*, Tecplot, Inc., 2012

[59] B. Whitlock, J.M. Favre, and J.S. Meredith, "Parallel In Situ Coupling of Simulations with a Fully Featured Visualization System," Eurographics Symposium on Parallel Graphics and Visualization, 2011

초 록

수소는 차세대 무공해 에너지원으로 그 관심이 증대되고 있으나, 단위 부피당 에너지 효율은 매우 낮은 수준이므로 실생활에 활용하기 위해서 압축, 액화, 또는 촉매를 이용한 저장기법 등이 요구된다. 현재의 기술 수준을 고려하면 액화 저장 방식보다 가압 저장 방식을 사용하는 것이 유용할 것으로 평가되고 있다. 다만 수소의 높은 가연성으로 인하여 명확한 점화원이 존재하지 않는 경우에도 고압 수소 가스 누출에 따른 점화 및 폭발 사고 사례 등이 보고되고 있으므로 고압 수소를 시스템에 적용하기 위해서는 안전에 대한 고려가 선행되어야 한다.

본 논문에서는 실험적, 수치적 기법을 통하여 고압 수소가 안전 배출관을 통해 누출되는 다양한 조건에 대한 자발 점화 현상을 이해하기 위한 연구를 수행하고, 이를 바탕으로 고압 수소의 자발 점화 메커니즘을 제시하였다. 이를 위하여 저기조와 튜브 사이에 설치된 안전 격막을 고압 수소를 이용하여 파열시킴으로써 관 내 수소의 누출 현상을 실험적으로 모사할 수 있는 실험 장비를 설계, 구축하였으며, 고온 공기-수소의 화학 반응, 충격파 및 팽창파, 난류 등과 같은 복잡한 물리적 현상이 포함된 유동 현상을 해석하기 위해 개발된 수치 해석 코드를 적용하였다.

연구는 실험과 수치적 접근을 병행하여 아직까지 시도되지 않았던 40 MPa 초고압까지 수소의 누출 압력 범위를 확장하고 배출관의 길이와 안전 격막의 파열 압력을 변화시키는 시험을 통하여 관의 길이와 파열 압력의 증가가 자발 점화 가능성을 높이게 된다는 경향을 밝혀내었다. 이와 함께 수치 해석을 통하여 가시화가 불가능한 축대칭형 관 내부에서의 유동 및 화염의 형성과

전파 특성을 파악하고 실험 결과와 비교를 통해 서로 다른 직경을 갖는 안전 배출관 내 자발 화염 형성 과정과 출구의 화염 전파 특성을 제시하였다. 또한 다양한 압력 범위에서 격막의 파열 형상 변화에 따른 자발 점화 특성 변화와 아직 실험이 수행되지 않은 초고압 영역에서 수소의 누출에 따른 자발 화염의 형성 및 점화 특성 등을 살펴보았다. 연구 결과 격막이 저압에서 파열될 경우 그 형상이 충격파의 형태, 공기-수소의 혼합 및 화염의 발생 영역 등에 큰 영향을 미치나, 고압 파열의 경우 격막의 파열 형태가 자발 점화에 미치는 영향이 점차 감소하는 것으로 조사되었다. 또한 고압 파열의 경우 강한 충격파의 발생으로 튜브 내 고온 공기-수소의 혼합 특성이 변화하여 관 내 자발 화염은 경계층에서 발생한 반응 영역으로부터 성장한 화염에 의해 형성되었다. 이와 같이 고압 수소가 누출되는 관 내 현상에 대한 연구와 함께 고압 수소의 누출부 주위에 다양한 거리에 위치한 높이가 다른 평판형 구조물에 의한 2차 점화 발생 가능성을 살펴보았다. 이 구조물은 관내에서 생성된 자발 화염의 전파 특성을 변화시키고 외부의 화염 안정화 단계에는 영향을 미치는 것으로 조사되었으나 누출된 혼합기의 체류 시간 증대에 따른 추가적인 화학 반응 등의 효과는 관찰되지 않아, 관내에서의 화염 형성이 자발 점화 현상의 주요 기제임을 밝혀내었다.

주요어 : 고압 수소, 자발 점화, 파열 격막, 충돌 분사, 수소 안정성
학 번 : 2008-30832